Atmospheric Pressure Chemical Vapor Deposition of Methylammonium Bromide and Tin(II) Bromide

Citation
Gustafson, Robert. 2022. Atmospheric Pressure Chemical Vapor Deposition of Methylammonium Bromide and Tin(II) Bromide. Doctoral dissertation, Harvard University Graduate School of Arts and Sciences.

Permanent link
https://nrs.harvard.edu/URN-3:HUL.INSTREPOS:37372248

Terms of Use
This article was downloaded from Harvard University's DASH repository, and is made available under the terms and conditions applicable to Other Posted Material, as set forth at http://nrs.harvard.edu/urn-3:HUL.InstRepos:dash.current.terms-of-use#LAA

Share Your Story

The Harvard community has made this article openly available.
Please share how this access benefits you. Submit a story .

Accessibility

Gustafson, Robert DAC.d

HARVARD UNIVERSITY

Graduate School of Arts and Sciences

DISSERTATION ACCEPTANCE CERTIFICATE

The undersigned, appointed by the

Harvard John A. Paulson School of Engineering and Applied Sciences
have examined a dissertation entitled:

"Atmospheric Pressure Chemical Vapor Deposition of Methylammonium Bromide and Tin(II) Bromide"

presented by: Robert Irwin Gustafson

Signature ________________________

Typed name: Professor R. Gordon

Signature ________________________

Typed name: Professor X. Li

Signature ________________________

Typed name: Professor L. Davis

May 4, 2022 Page 1 / 1

Atmospheric Pressure Chemical Vapor Deposition of Methylammonium Bromide and Tin(II) Bromide

A dissertation presented

by

Robert Irwin Gustafson

to

The John A. Paulson School of Engineering and Applied Sciences

in partial fulfillment of the requirements

for the degree of

Doctor of Philosophy

in the subject of

Applied Physics

Harvard University

Cambridge, Massachusetts

May 2022

© 2022 Robert Irwin Gustafson
All rights reserved

Dissertation Advisor: Roy Gordon Robert Irwin Gustafson

Atmospheric Pressure Chemical Vapor Deposition of Methylammonium Bromide and Tin(II) Bromide

Abstract

With the need to rapidly decarbonize society to slow the effects of and halt climate change, new forms of renewable energy need to replace current fossil fuel consumption. Of the alternatives, solar energy is both free and universally accepted. However, today's solar panels made of silicon are still too inefficient, too expensive, and in too short of supply to deploy as quickly as the world needs in all markets. Perovskite absorbers offer the opportunity to dramatically increase efficiency as tandem solar panels and decrease costs. This dissertation explored the use of atmospheric pressure chemical vapor deposition (APCVD) in depositing perovskite relevant films methylammonium bromide and tin(II) bromide.

Precursors for making these films were selected based on metrics such as volatility, thermal stability, and ease of handling. A tin compound was used that conveyed suitable volatility and thermal stability by Thermogravimetric Analysis. The bromide source was provided by hydrogen bromide, and a process for providing hydrogen iodide was explored. Methylamine was used in its neat form as a gas.

The reactor geometry used to control the gas flow was designed using computational fluid dynamics software. Two designs are discussed that aimed to minimize inlet contamination and premature deposition – two sources of film inhomogeneity. The resultant films were characterized

by a suite of techniques to identify their composition and quality. For $SnBr_2$ films, additional impurity analysis was performed to identify potential sources of the impurities.

Finally, Energy Dispersive X-ray Spectroscopy was used to measure the spatial dependence of the deposition rate. These data were then used to qualitatively assess the mechanistic origins of the deposition through modeling. Results suggested an absence of gas phase reactions and substantial surface reactions of at least two kinds. These results and procedures may be used to fully develop APCVD models for the deposition of perovskite absorbers and accelerate the world towards a solar energy future.

Table of Contents

Title page i

Copyright ii

Abstract iii

Table of Contents v

Acknowledgements viii

1 Introduction 1
- 1.1 Motivation 1
- 1.2 Solar Cell Physics 4
- 1.3 Current solar cell technologies 12
- 1.4 Perovskite solar cells 13
- 1.5 Towards efficient, stable, lead-free PSCs 15
- 1.6 Conclusions 19
- 1.7 References 20

2 Atmospheric Pressure Chemical Vapor Deposition 23
- 2.1 Motivation 23
- 2.2 APCVD Principles 24
- 2.3 Precursor Selection 30
  - 2.3.1 Tin precursor selection 31
  - 2.3.2 Hydrogen halide selection 40
  - 2.3.3 Methylamine Selection 49
- 2.4 Conclusion 50
- 2.5 References 51

3 APCVD Reactor Development 53
- 3.1 Motivation 53
- 3.2 CFD Simulations 55
  - 3.2.1 Gas Transport Models 57

3.2.2 Software Packages 61
3.3 Reactor Design 63
3.4 Simulation Results 65
3.4.1 Gen 1 Reactor 65
3.4.2 Gen 2 Reactor 71
3.5 Reactor Fabrication 78
3.5.1 Gen 1 Reactor Fabrication 78
3.5.2 Gen 2 Reactor Fabrication 81
3.6 Conclusion 82
3.7 References 82
4 Characterization of MABr and $SnBr_2$ films 85
4.1 Motivation 85
4.2 Compound Identification 85
4.2.1 X-Ray Diffraction Spectroscopy 85
4.2.2 X-Ray Photoelectron Spectroscopy 90
4.3 Morphology Characterization 94
4.3.1 Scanning Electron Microscopy 95
4.3.2 Profilometry 99
4.3.3 Energy Dispersive X-Ray Spectroscopy 109
4.4 Impurity Analysis 116
4.4.1 $SnBr_2$ EDS Impurity Analysis 117
4.4.2 $SnBr_2$ ATR-FTIR Analysis 119
4.4.3 $SnBr_2$ Raman Analysis 121
4.5 Conclusion 123
4.6 References 123
5 Modeling of MABr Depositions 125
5.1 Motivation 125
5.2 CVD Modeling Framework 126
5.2.1 Classical Kinetic Theory 126
5.2.2 *Ab-initio* Estimates of Activation Energy Barriers 130
5.2.3 Initial Model Estimates 135
5.3 EDS Training Sets 136

5.4 CFD/CVD Simulation Results 137
5.4.1 Absence of Gas Phase Reactivity 137
5.4.2 Evidence for Surface Chemistry 144
5.4.3 Evidence for a Rideal-Eley Reaction 148
5.4.4 Evidence for a L-H Reaction 151
5.5 Conclusion 153
5.6 Appendix 154
6 Conclusion 156

Acknowledgements

In many ways, it is harder to leave Harvard than to finish a PhD. This place I have called home for so long now has been truly wonderful. I have been so fortunate to come here and meet likeminded, curious people at every turn and befriend so many from so many different backgrounds. I can't thank you all – my friends – enough for providing this rich, intellectual playground to develop and grow as a student and person. In addition to my friends and peers, I wish to thank the staff at CNS – Greg Lin, Arthur McClelland, Tim Cavanaugh – for sharing so much insight and time in helping guide my research. To Jim MacArthur and Stan Cotreau, I also cannot thank you enough for teaching me the ropes in do-it-yourself electronics and machining. To Prof. Xin Li, I wish to thank you for reviewing my work and kindly participating on my defense committee.

The Gordon Group, above all, helped create such a positive work environment during my time at Harvard. Everyone was truly selfless in their time to help when I needed them, especially as buddies in the machine shop. You all made it a friendly (and fun!) place that cannot be overappreciated. In particular, I wish to thank Prof. Luke Davis who graciously shared his time and interest in my work through numerous discussions and points of advice. I also wish to thank my advisor, Roy Gordon. I cannot think of another person who would be so welcoming to me as I joined and so patient of me over the years as I learned the subtle art of scientific research. His curiosity, passion for sustainability, and insistence on treating everyone with respect is something I hope to carry with me. From a young know-nothing to a trained scientist confident in speaking on matters of the field to his peers, I owe a debt of gratitude to you, Roy.

Of course, I would be remiss to omit my thanks to my loving and supportive parents (who, I'm sure, will form a sizable fraction of this work's readership). From my days as a twelve-year-old, sputtering through old physics books from the library, you have been there to foster and encourage my interests in science and engineering. For this, the many years of care, patience, and love, I can never thank you enough. I love you.

And, to my dear Lisa. Thank you for being my friend this many years. I am glad we met at that volleyball court – who plays volleyball in a dress, anyway? You have been there to listen when I needed someone to explain something so I could understand it better myself and to listen when… I just needed to vent. You bring so much color into my life by sharing your enthusiasm for events, friends, and the outdoors and help blunt some of my worst tendencies (is "stubborn" even a tendency?). Thank you for being with me on this journey. I love you.

1 Introduction

"Human influence on the climate system is clear, and recent anthropogenic emissions of green - house gases are the highest in history. Recent climate changes have had widespread impacts on human and natural systems." – IPCC Climate Change 2014 Synthesis Report[1]

1.1 Motivation

Anthropogenic emissions are altering the natural and built environment at an alarming scale and a relentless pace. Scholars have known of the greenhouse effect since the 19th century, yet appreciating the impact of exponentially increasing rates of emissions would take many more generations. Already, the concentration of CO_2 in the atmosphere has increased from below 300 ppm at the turn of the 20th century to above 400 ppm today[2]. The previous 3 decades have been deemed *likely* the warmest 30-year period in the last 1400 years[1]. Carbon dioxide (CO_2) emitted today will likely remain in the Earth's carbon budget for at least the next several thousand years with a significant fraction remaining in the atmosphere for much longer[3]. Given CO_2's relative inertness and vast dispersal throughout the atmosphere and oceans, it seems implausible that some yet unimagined machine, beyond large-scale natural intervention, will be able to rapidly scrub CO_2 from the atmosphere in a *technically* and *economically* feasible way.

Therefore, the challenge now is to mitigate further emissions. By far the largest source is the energy sector, accounting for near 68% of greenhouse gas (GHG) emissions in 2014[4]. This includes the combustion of coal, oil, and gas, which accounted for 81% of total primary energy supplies and 99% of CO2 emissions in this sector.

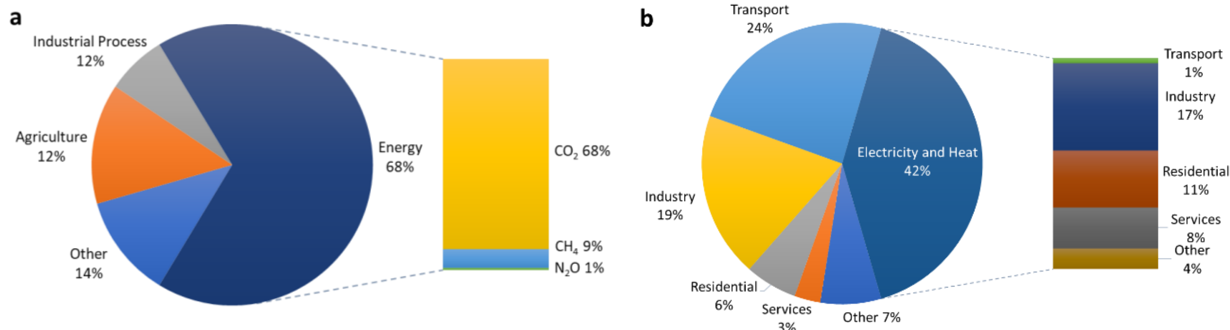

Figure 1-1: (a) Estimated shares of global anthropogenic GHG, 2014.[4] (b) World CO_2 emissions from fuel combustion by sector, 2015[4]

By partitioning the combustion of these fuels into the various sectors they serve, one sees, as in Figure 1-1b, that the greatest preponderance of emissions come from electricity and heat generation. Thus, the greatest reduction in emissions could be had by addressing the CO_2 footprint in this sector. Furthermore, there are already many renewable energy technologies competitive with fossil fuel-based ones. However, these competitive advantages may be partially due to governmental subsidy or favorable geological conditions (e.g. hydroelectric power). Nuclear power, though technically feasible, is now crippled by cost overruns and political and social barriers[5]. Wind power worldwide generates 22x the global annual commercial energy consumption of 2009, but this power is not evenly distributed[6]. Furthermore, energy from the wind originates from approximately 1% of the absorbed solar irradiance. This leads one to consider solar energy, which is much more evenly distributed across the world and radiates enough energy in one hour to provide for the world's yearly energy needs[7]. The two leading technologies to generate electricity from sunlight are solar thermal systems and photovoltaics (PVs). Solar thermal systems rely on an array of mirrors to focus sunlight onto a containment of molten salt to use in a Sterling or other power cycle for utility scale generation. Solar thermal systems may also be used for local hot water or space heating. PVs leverage the development of semiconductor physics over the past

60 years to directly convert sunlight to electricity without an intermediate power cycle or heat generation. A solar thermal system may be advantageous in particular instances, but PV technology offers more ubiquitous use cases. Additionally, solar PV generation has rapidly grown in recent years (see Figure 1-2).

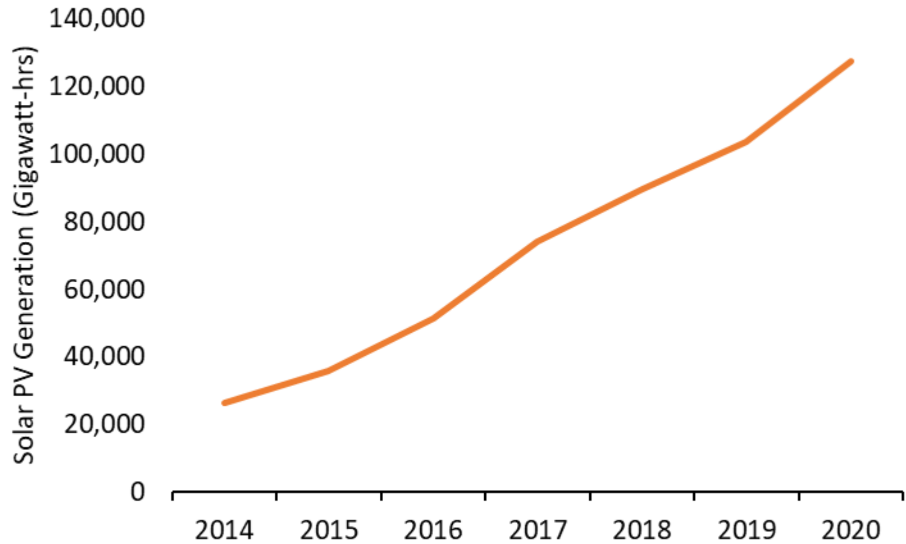

Figure 1-2: Electricity generation from PVs in the U.S[8].

However, when compared to the rest of the generation in the U.S., the percent of electricity generated by solar is near 3%.

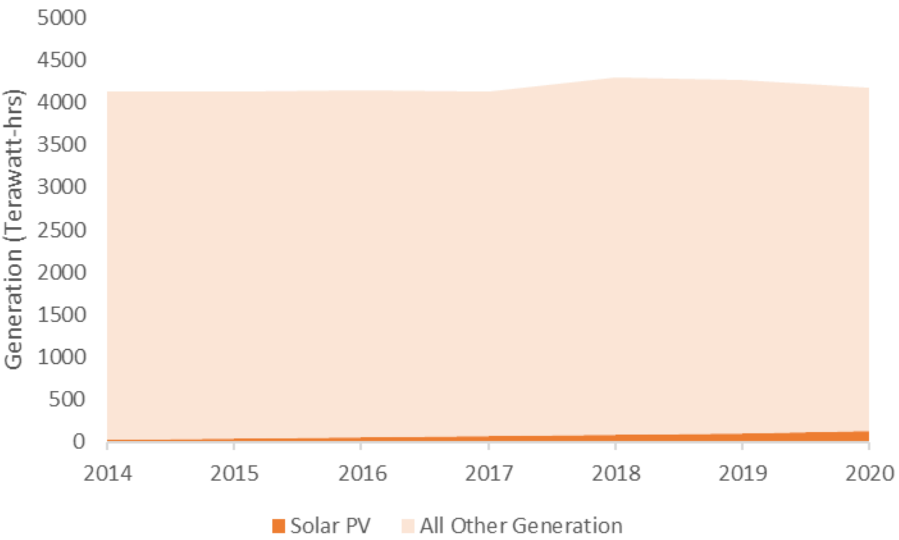

Figure 1-3: Net generation of electricity in the U.S. across all sources[8]

The potential for growth is enormous. However, despite drastic reductions in module and inverter costs in recent years and average levelized cost of electricity (LCOE) for utility-scale solar energy below $0.04/kWh,[9] the cost of solar will need to continue to decrease to both increase the rate of adoption and pressure the early retirement of fossil fuel generation sources. One way to decrease the cost of solar on a $/W basis is to increase the efficiency. Average Tier 1 solar panels of ~ 19—20% efficiency[10] are still far below the limit of 34% for a single junction solar panel and much below that for a tandem device[10].[11] If this efficiency could be increased and if the cost of manufacturing solar panels decreased, then it is believable that solar energy could further accelerate the global decarbonization effort.

1.2 Solar Cell Physics

Solar energy from a utility is the aggregate energy from a collection of solar panels, each typically on the order of 1-2 m^2. Si-based solar panels are made by connecting individual solar

cells, which themselves encompass roughly 200 cm^2. Thin-film solar panels, however, are made by scribing a monolithic solar cell into individual sub-cells that are connected back in series to amplify the voltage (at the expense of current). Shown below is a typical cross-section of a thin-film heterojunction solar cell.

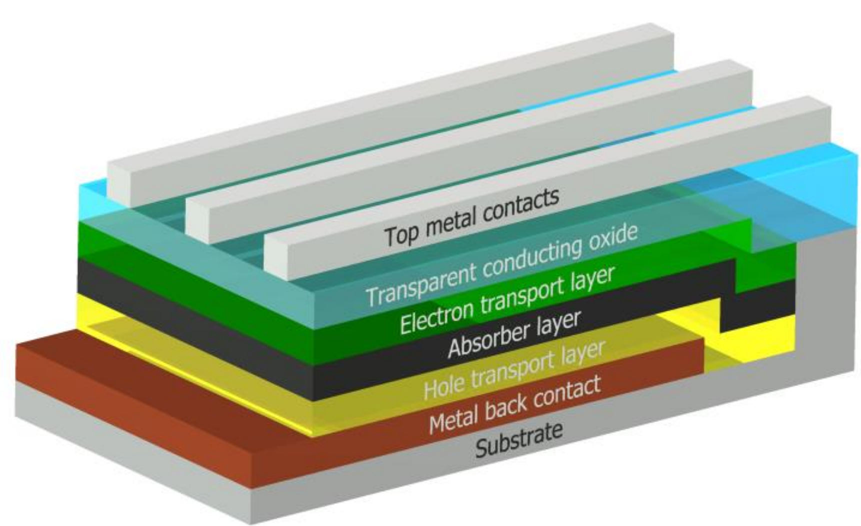

Figure 1-4. Solar cell schematic

Briefly, the top metal contacts collect electrons from the transparent conducting oxide (TCO) and conduct them to the next cell in series or a load; the TCO layer permits the passage of photons while transporting electrons from the electron transport layer (ETL) to the metal contacts; the ETL (much thinner in comparison to the absorber or TCO layers – shown in Figure 1-4 with an exaggerated relative thickness) passivates surface defects that would otherwise be present at the TCO / absorber interface and blocks the flow of holes to the TCO; the absorber layer converts photons to excitons and facilitates exciton separation into electrons and holes; the hole transport layer (HTL), analogous to the electron transport layer, passivates otherwise present trap states at the surface of the absorber layer, blocks the flow of electrons into the back contact layer, and

facilitates the flow of holes to the back metal contact; the back metal contact collects the holes to deliver to the load or sequential cell in the panel; the substrate provides a rigid or flexible support to the stack. Not all layers in Figure 1-4 are present in all solar cell architectures, but the aims of each layer must be accomplished in any efficient solar cell.

The absorber layer, to which all other layers are supporting actors, absorbs photons according to its bandgap, E_g, absorptivity, $a(h\omega)$, the solar spectrum, $\frac{dj_\gamma}{d\hbar\omega}$, and thickness, L_D, as shown in[12]

$$j_{sc} = -e \int_{E_g}^{\infty} a(\hbar\omega, L_D) \left(\frac{dj_\gamma}{d\hbar\omega} \right) d\hbar\omega \tag{1-1}$$

$a(h\omega)$ contains information regarding the density of states (DOS) in the conduction band (CB) and the valence band (VB), the probability of occupation as given by the Fermi-Dirac distribution, and the absorption coefficient. More generally, the absorptivity describes how many states there are in the conduction and valence bands, and for each of those states, what the likelihood per unit energy is that an electron in the valence band transitions into the conduction band with a probability proportional to the absorption coefficient. When the applied voltage across a solar cell is zero, the integral in Eq. 1-1 equals the short-circuit current density, j_{sc}, the maximum possible current for that specific testing condition. Obtaining this current from a real solar cell device would require an external quantum efficiency (EQE) of 100% for all photon energies above the bandgap. More fundamentally, this would require an internal quantum efficiency (IQE) of 100%, which requires only radiative recombination of electrons and holes with no parasitic absorption, surface recombination velocities of 0, and only reemission of light through the narrow solid angle pointing

back towards the sun. For a real solar cell, achieving all of these would require a material of the highest optoelectronic quality comparable to GaAs (IQE of 99.7%[13]), a perfectly reflecting back contact (a metal) and a completely transparent front contact, and a lens to focus any outcoupled light back towards the sun. Assuming these conditions are met, the next step is to convert the chemical potential energy of the electrons and holes into electrical energy by selectively collecting them at their respective transport layers.

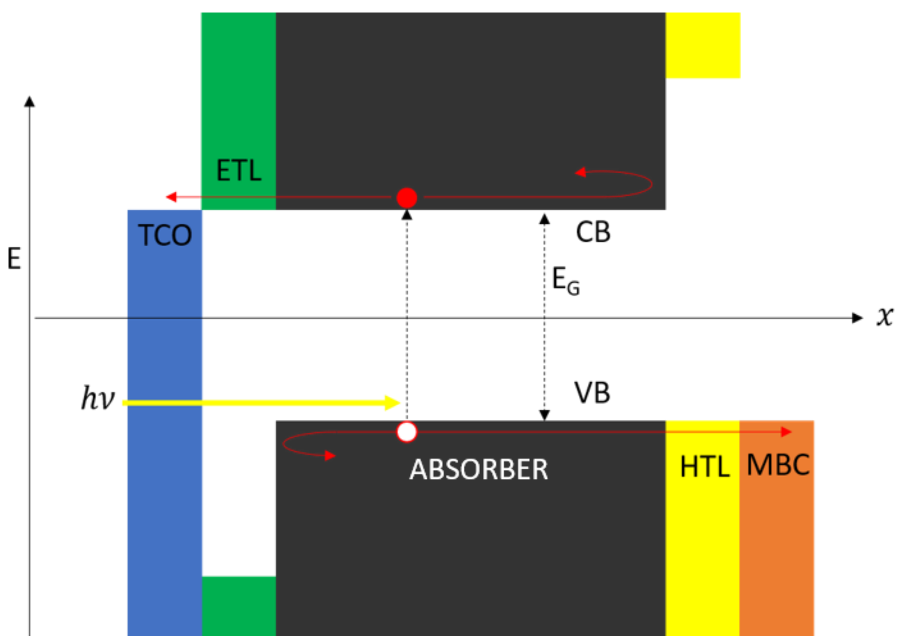

Figure 1-5: Band diagram

Figure 1-5 depicts the events of absorption and charge collection within a band diagram model. The key takeaway is that the VB of the HTL should align with the VB of the absorber ($0 \leq E_{VB_{absorber}} - E_{VB_{HTL}} \leq \sim 0.3$ eV) and likewise for the CB of the absorber and ETL ($0 \leq E_{CB_{ETL}} - E_{CB_{absorber}} \leq \sim 0.3$ eV) once contact of the layers is made (0.3 eV is a rule-of-thumb maximum energy barrier that still permits thermionic emission without limiting current at normal operating temperatures). If the ETL CB is much lower than the CB of the absorber and/or the VB of the HTL

is much higher than the VB of the absorber (a higher VB of the HTL corresponds to a lower energy level for holes), then a sharp drop in the chemical potential of the charges can be expected with the result of lowering the sensible voltage at the contacts. If the ETL CB (HTL VB) is much higher (lower) than the CB (VB) of the absorber, then charge transport out of the absorber is limited and the short-circuit current suffers. If the transport layers are too resistive or non-selective enough, then a larger built-in field would be required to separate the charges to their respective electrodes. This field would cause the band diagram to tilt, once again lowering the expected voltage at the contacts. Therefore, the ideal electron (hole) transport layer would have an aligned CB (VB) with the absorber CB (VB) and high electron (hole) mobility. The transport layers, contrary to the schematics in Figure 1-4 and Figure 1-5, would be thick enough only to form a continuous layer, desirably on the order of tens of nm. Additionally, the foregoing discussion neglected the deleterious action of surface traps at the absorber / transport layer interface. To suppress the action of these non-radiative recombination pathways, one aims for a spike in the energy band of $0 - 0.3$ eV. This helps suppress the back recombination of majority carriers from the transport layer with carriers in the absorber layer.

Mathematically, the governing equations relating the chemical potential of the charge carriers to their current out of the solar cell, hence the possible deliverable power, have been derived from first principles. For either the electron or hole density in the absorber layer, the rate of change of the charge density ($\frac{dn_Q}{dt}$) must be equal to the rate of charge generation (G_Q) minus the rate of recombination (R_Q) and the change of charge current (∇j_Q) leaving the absorber. Under steady state,

$$\frac{dn_Q}{dt} = 0 \,. \tag{1-2}$$

Therefore,

$$\nabla j_Q = G_Q - R_Q \,. \tag{1-3}$$

In the one-dimensional model, this affords

$$j_Q = \int_{absorber} (G_Q - R_Q) dx \,. \tag{1-4}$$

Noting that R_Q is proportional to the product of electron and hole densities, $n_e n_h$, it can be rewritten using a form of the law of mass action that has at its roots the results of the Sakur-Tetrode equation.

$$R_Q = R_Q^0 \left(\frac{n_e n_h}{n_i^2} \right) = R_Q^0 \exp\left(\frac{\eta_e + \eta_h}{kT} \right) \tag{1-5}$$

Here, n_i is the intrinsic charge density of the film, kT is the product of the Boltzmann factor and the temperature, and $\eta_e + \eta_h$ is the sum of the electrochemical potential energies of the electrons and holes. That the electrons and holes have separate electrochemical potentials is a result of the Fermi level splitting under illumination and the bandgap retarding the thermalization of the electrons (holes) in the CB (VB) to the VB (CB). R_Q^0 is the recombination rate under no illumination and must be equal to the generation rate, G_Q^0, in the dark for ∇j_Q must equal 0. This is a consequence of the second law of thermodynamics. By removing the hot reservoir (the sun) from the system, the device is only in contact with its cold reservoir (the surroundings), and so no

temperature or chemical gradient exists in which to carry out any incoming or generated entropy which precludes the establishment of a steady-state operation. Therefore,

$$G_Q^0 = R_Q^0 \tag{1-6}$$

$$G_Q = G_Q^0 + G_Q^i \tag{1-7}$$

where G_Q^i is the rate of charge generation via illumination. Rewriting Equation (1-4) yields

$$j_Q = -q \int_{absorber} \left(G_Q^0 \left[1 - \exp\left(\frac{\eta_e + \eta_h}{kT} \right) \right] + G_Q^i \right) dx \tag{1-8}$$

where q is the fundamental unit of charge. One observes that the integral of G_Q^i is none other than the total generation of charge carriers from illumination, j_{sc}, from Equation (1-1) and that the integral of the first part of Equation (1-8) is nothing but a constant times the operand (assuming the electrochemical potential doesn't change significantly in the absorber layer, which it shouldn't in an ideal solar cell). Setting the sum of the electrochemical potentials as eV, the voltage at the metal contacts, one arrives at the ideal diode equation

$$j_Q = j_s \left[\exp\left(\frac{eV}{nkT} \right) - 1 \right] + j_{sc} \, . \tag{1-9}$$

j_s is the reverse saturation current. Because non-radiative recombination is responsible for this current, it is beneficial that it be as low as possible. In a practical solar cell, the electrochemical

potential is not perfectly flat across the absorber layer, so an additional factor, the ideality factor n, is added to the denominator of the exponential to express the deviation of a real diode from the ideal. The ideal diode equation ($n = 1$) can be plotted to give a graphical description of the current-voltage relationship.

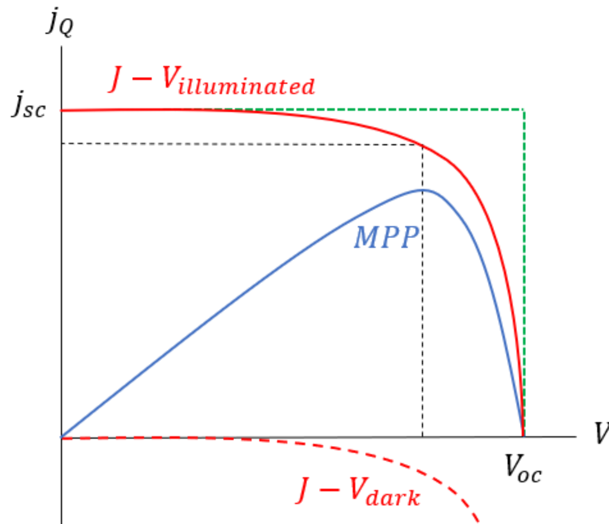

Figure 1-6: Ideal diode J-V curve

In Figure 1-6 the solid red curve denotes the current-voltage relationship under illumination; the dashed red curve denotes the current-voltage relationship with no illumination; the blue curve depicts the output power, or the product of the current and voltage, with the dashed black lines marking the current and voltage at the maximum power point (MPP). The ratio of the areas under the dashed black lines and the dashed green lines is called the fill factor, FF. This entity relates the product $V_{oc}j_{sc}$ to the output power at the MPP. Normalizing $V_{MPP}j_{MPP}$ by the total power in, P_{in}, one arrives at the overall solar cell efficiency,

$$\eta = \frac{V_{MPP}j_{MPP}}{P_{in}} = \frac{V_{oc}j_{sc}FF}{P_{in}} \quad (1\text{-}10)$$

Solar cell efficiencies are measured in practice using the Air Mass 1.5 (AM1.5) spectrum with an incident power density of 100 mW/cm^2 and a solar cell temperature of 25 ^{o}C. Thus, for solar energy to penetrate the energy market, solar cell technology must be developed with higher efficiencies, lower costs, and with earth-abundant, safe materials.

1.3 Current solar cell technologies

In recent decades, several new solar cell materials have come out of research labs and into the PV market to challenge crystalline silicon (c-Si) solar cells. However, not all these technologies are well suited to the current demands from the solar market. According to Ref. 10, the percentage of the module cost to the overall cost in $/Watt DC is approximately 43%. Therefore, 24% reduction in module manufacturing costs would only achieve a 10% reduction in total costs of solar PV installation. The trend in research and the market is thus moving away from cheap, but low-efficiency technologies to potentially more expensive and high-efficiency technologies. It is expected that c-Si solar cells will achieve market penetration with up to 25% efficiency[14] sometime by the next decade. Therefore, in comparing the viability of various solar cell technologies' ability to compete with c-Si, discussion is limited to those technologies that can offer solar cells with efficiencies greater than 20%.

The list of possible candidates is reduced under this necessary requirement. Poly-crystalline silicon (poly-Si), micro-crystalline silicon (μ-Si), and amorphous silicon (a-Si:H) solar cells achieve efficiencies below 20%[14]. They may be inserted as a p- or n-type (hole-doped or electron-doped) layer in a c-Si solar cell but are likely to continue losing market share to mono-crystalline

Si (mono-Si). Similarly, organic solar cells do not yet achieve at least 20% efficiency. While III-V semiconductor solar cells (e.g. GaAs) do achieve more than 20% efficiency, their manufacturing costs are significantly greater than c-Si and will not be discussed. This leaves the thin-film ($<10\ \mu m$) chalcogenide solar cells based on CdTe and $Cu(In,Ga)(Se,S)_2$ absorbers as possible contenders.

CdTe solar cells are made from a high-temperature ($\sim 500\ ^{o}C$) continuous manufacturing process that results in commercial-grade solar cells with efficiencies near 18% and lab-grade efficiencies near 21%.[15] With a tunable direct bandgap, strong absorption, and 98% less absorber material usage than c-Si, CdTe have achieved near $0.70/Watt DC.

Cu(In, Ga)(Se,S) (CIGS) solar cells have bandgaps between 1.1-1.2 eV and are direct gap semiconductors.[15] They are processable from either solution or vapor-based methods and can be deposited at temperatures low enough to support polyimide substrates. 22% efficient lab-based solar cells and 15.7% commercial modules have been so far achieved. These materials suffer from variations in film stoichiometry and defects, which lead to a lower V_{oc}. Like Te, the scarcity of elemental indium causes one to question CIGS long-term viability as a possible contender to c-Si. However, this shouldn't limit these technologies' immediate use as appropriate.

1.4 Perovskite solar cells

Still an emerging technology, perovskite solar cells (PSCs) have the potential to compete with c-Si. Since their introduction by Miyasaka in 2009, PSCs have increased in efficiency from 3.8% to an NREL certified 25.7%.[16,17] The cause for this meteoric rise in efficiency may be attributed to the furious pace and level of research in this field since 2009, versatility of fabrication

methods, high absorption coefficient, high IQE, and defect tolerance. The general perovskite crystal structure can be seen in Figure 1-7.

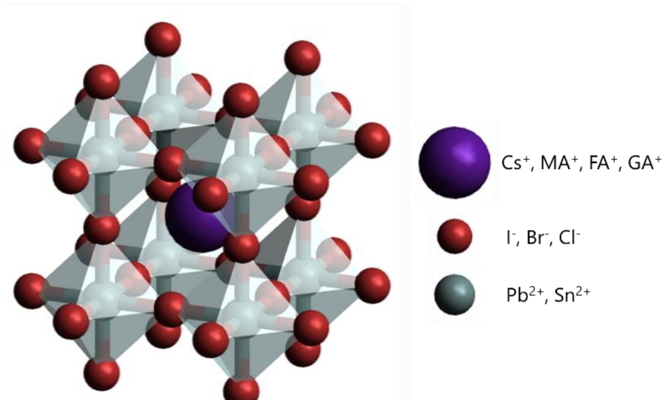

Figure 1-7: General perovskite crystal structure.

An example fabrication process proceeds as follows. First, fluorine-doped tin oxide (FTO) is deposited on a glass substrate followed by a layer of either planar or meso-porous TiO_2 which serves as the ETL. Record efficiencies have utilized the meso-porous structure, but this step requires sintering around 500 °C, which makes manufacturing costlier. The perovskite absorber layer is then deposited under a wide variety of methods including spin-coating, chemical bath, dip-coating, doctor blading, slot-casting, spray-coating, screen printing, inkjet printing, low pressure chemical vapor deposition (LPCVD), and evaporation among others. Next, the HTL, typically a lithium-doped organic material known as Spiro-MeOTAD, is deposited onto the perovskite layer. Lastly, gold metal contacts are sputtered or evaporated onto the HTL to complete the device fabrication.

The name "perovskite" refers to the crystal structure of composition ABX_3, of which calcium titanate, $CaTiO_3$, is the original crystal of this type. For solar cells, the most common

composition studied has been methylammonium lead iodide, $MAPbI_3$, but many compositions have been made with better and worse efficiencies.

One of the current, most efficient solar cells is a single cation lead perovskite with the composition $FAPbI_3$.[18] This composition yielded a stabilized efficiency of 25.2% and a V_{oc} of 1.174 V, and a FF of 81.8%. As mentioned already, a high V_{oc} is indicative of low levels of non-radiative recombination and a high IQE. Current research efforts into lead-based PSCs are now focused on further improving the V_{oc} by minimizing parasitic absorption and reducing surface recombination velocities by better matching transport layer charge carrier injection rates, reducing transport layer series resistances, and improving surface coverage and passivation to the perovskite layer.[19] Beyond efficiency improvements, the field is assiduously working at scaling up manufacturing methods to move beyond spin-coating and to improve device stability.

1.5 Towards efficient, stable, lead-free PSCs

Despite the achievements of lead-based PSCs, the issue of the toxicity of lead still remains. According to the World Health Organization (WHO), there is no known safe level of lead exposure.[20] Because of this fact, expanding water-soluble, lead-based PSCs and the use of toxic anti-solvents in the manufacturing process could lead to environmental and health disasters.[21,22] Replacing lead with a safe, abundant element is not straightforward. Many elements with a suitable oxidation state lead to a perovskite with too high a bandgap (Be, Ca, Sr, Ba), are toxic still (Cd, Hg), or do not have desirable electrical properties.[23] The most promising elemental substitution is Sn^{2+}. It has a similar ionic radius as Pb^{2+} (110 pm vs 119 pm), more favorable perovskite bandgap (1.3 eV for $MASnI_3$), and a strong absorption coefficient.[23] However, to date, only efficiencies

less than 15%[23] have been achieved with pure Sn-based PSCs, far below those of lead-based PSCs.[23—25] It is understood in the literature that better preparation methods are needed to suppress unintended hole-doping, which greatly reduces the V_{oc}.[26]

Theoretical studies of the three major tin iodide perovskites, cesium (Cs^+) – methylammonium (MA^+) – formamidinium (FA^+) tin trisiodide, have shown tin-vacancies to be the primary cause of the high hole concentration, which limits the V_{oc} for an intrinsic solar cell according to

$$V_{oc} \propto \ln\left(\frac{(N_A + \Delta n)\Delta n}{n_i^2}\right) \quad (1\text{-}11)$$

where N_A is the doping concentration (or defect concentration assuming the transition state between a neutral or charged defect site is higher in energy) and Δn is the steady state excess charge generated from light exposure (assuming $\Delta n \gg n_{min}$ where n_{min} is the minority charge carrier concentration).

From Ref. 27 and 28, the enthalpy of formation of the tin-vacancy defect, V_{Sn}, is the lowest in most cases. For $MASnI_3$, the defect has a negative enthalpy of formation except for the Sn-rich growth condition and only within 0.15 eV of the VBM. This suggests that the $MASnI_3$ are inherently, highly p-doped. Due to the slightly longer $Sn - I$ bond length in $FASnI_3$ compared to the $Sn - I$ bond length in $MASnI_3$ (3.31 Å to 3.23 Å), the $Sn\ 5s - I\ 5p$ antibonding coupling is weaker in $FASnI_3$, which leads to a higher enthalpy of formation of tin-vacancies in the FA^+ tin perovskites compared to the MA^+ tin perovskites. In the case of $FASnI_3$, it is possible to achieve intrinsic carrier concentrations under Sn-rich growth, which Ref. 28 suggests is not true with MA^+ tin perovskites. Like the FA^+ perovskites, the Cs^+ tin perovskites can have intrinsic-like carrier

concentrations in samples grown in tin-rich environments. However, one must be careful to not introduce too much tin as tin-rich conditions can generate tin-iodide antisites, $\mathrm{Sn_I}$, which act as efficient recombination centers deep in the band gap with moderate enthalpies of formation $\Delta\mathrm{H}_{\mathrm{Sn_I}} \approx 0.5 - 0.7$ eV in this growth condition.[27] Despite the fact that Cs^+- and FA^+- perovskites have the potential for intrinsic doping levels, very few devices have been made with low open-circuit voltage deficiencies[29], suggesting there still exist high levels of doping as compared to their lead analogues.

To understand the origins of the hole-doping, one may use the Kröger–Vink notation to delineate the possible chemical reactions to generate excess holes. Explanations of the Kröger–Vink notation system may be found in the literature[30]. Assuming the presence of only the neat tin perovskite and adventitious oxygen, the following reactions may lead to p-type doping[30]:

$$\mathrm{V_{Sn}^{X}} \rightarrow \mathrm{V_{sn}''} + 2\mathrm{h}^{+} \tag{1-12}$$

$$\mathrm{Sn_{Sn}^{X}} + \frac{1}{2}\mathrm{O_2} \rightarrow \mathrm{Sn_{Sn}^{\cdot\cdot}} + \mathrm{O}^{-2} \tag{1-13}$$

$$\mathrm{Sn_{Sn}^{\cdot\cdot}} \rightarrow \mathrm{Sn_{Sn}^{X}} + 2\mathrm{h}^{+} \tag{1-14}$$

Reaction (1-12) generates two holes and a doubly, negatively charged tin-vacancy from a neutral tin-vacancy. Assuming appropriate growth conditions (tin-rich) are used in the fabrication process of either the Cs^+- or FA^+- perovskite (or some mixture of the two), the number of tin-vacancies can be sufficiently suppressed. That leaves reaction (1-13) and (1-14) responsible for the preponderance of holes. In reaction (1-13), adventitious oxygen may enter the film either during

or post deposition and oxidize a neutral tin(II) to tin(IV). The tin(IV) ion subsequently may accept two electrons from the lattice to become a neutral tin atom with respect to the lattice, and release two holes as in reaction $(1-14)$.[30,31] It has been suggested in the literature that reaction (1-13) proceeds via formation of SnI_4 and SnO_2 during the oxidation process involving two tin atoms according to reaction (1-15).

$$2SnI_2 + O_2 \rightarrow SnO_2 + SnI_4 \qquad (1\text{-}15)$$

The SnI_4 impurity itself does not lead to an increase in the hole concentration as the oxidation of the neutral tin from Sn^{2+} to Sn^{4+} is locally compensated by the four iodide ions. The total increase in hole doping is from the oxidation first by O_2 as shown in reaction (1-13). This suggests that to reduce p-type doping in tin-based perovskites, Sn^{4+} compounds should be eliminated from the starting precursors, and oxygen should be eliminated from the deposition environment. Atmospheric pressure chemical vapor deposition (APCVD) is a process that can achieve both of those criteria. By using a volatile Sn^{2+} precursor, one may avoid using impure tin precursors as the Sn^{4+} congener may be insufficiently volatile. The oxygen levels inside an APCVD reactor may also be reduced to the parts per trillion (ppt) level using gas purifiers. APCVD eliminates the use of solvents altogether and affords the processing of PSCs in a mass-producible technique. By operating at deposition temperatures of 120–180 ^{o}C, APCVD affords the opportunity to form large grains for improved device performance without the need to worry about the tradeoffs between nucleation and growth kinetics.[32] If future solar panel factories are to produce at the multi-GW/yr scale, only truly mass-production techniques will be realized.

1.6 Conclusions

The world needs to transition to carbon dioxide-free energy sources as soon as possible. The economic reality of ramping up and maintaining silicon-based solar panel production and installation suggests that this will not occur at the scale and within the timeline necessary to limit global warming to 1.5 °C. Alternative forms of solar panel technology should be pursued in addition to silicon to aid this effort. One such technology, perovskite solar cells, has shown considerable promise, although lab-based production methods are far inadequate to commercialize at necessary production levels. However, atmospheric pressure chemical vapor deposition (APCVD) is a process that can meet future solar panel production demands at low cost.

Therefore, the aim of this thesis was to develop an APCVD process to deposit tin-based perovskites. The results of this endeavor are a reactor design and process model for depositing the precursors methylammonium bromide (MABr) and tin dibromide ($SnBr_2$), which may be applied towards designing a high-throughput reactor for depositing the ternary perovskite, $MASnBr_3$. Although the MA^+- perovskites are known to have inherently high doping under all growth conditions[28], the same or similar conditions and equipment presented in this thesis may be used to deposit $FASn(I,Br)_3$ from formamidine gas[33]. Beyond perovskites, the APCVD hardware and models developed in this thesis may be applied more generally to lab-scale and industrial-scale R&D of thin-film materials.

1.7 References

1. IPCC, *Climate Change 2014: Synthesis Report. Contribution of Working Groups I, II and III to the Fifth Assessment Report of the Intergovernmental Panel on Climate Change,* (eds. R.K. Pachauri and L.A. Meyer) (Geneva, Switzerland, 2014).

2. IPCC, *Long-term Climate Change: Projections, Commitments and Irreversibility. In: Climate Change 2013: The Physical Science Basis. Contribution of Working Group I to the Fifth Assessment Report of the Intergovernmental Panel on Climate Change,* Cambridge University Press, Cambridge, United Kingdom and New York, NY, USA (2013).

3. Archer, D., et al. Atmospheric lifetime of fossil fuel carbon dioxide. *Annu. Rev. Earth Planet. Sci.*, **37**, 117–34 (2009).

4. IEA, *CO_2 emissions from fuel combustion highlights 2017,* OECD/IEA, Paris. https://doi.org/10.1787/co2_fuel-2017-en (2017).

5. Chang, M., White, D., Hausman, E., Hughes, N., Biewald, B., "Big Risks, Better Alternatives," Synapse Energy Economics, Inc. Cambridge, MA. (2011).

6. Lu, X., McElroy, M., Kiviluoma, J., Global potential for wind-generated electricity, *PNAS*, **106**, 10933-10938 (2009).

7. Lewis, N., Toward cost-effective solar energy use. *Science*. **315**. 798-801 (2007).

8. EIA. *Electric Power Annual 2021*. (2022).

9. EIA. *Levelized Costs of New Generation Resources in the Annual Energy Outlook 2022*. (2022).

10. Feldman, David, Ramasamy, Vignesh, Fu, Ran, Ramdas, Ashwin, Desai, Jal, & Margolis, Robert. *U.S. Solar Photovoltaic System and Energy Storage Cost Benchmark: Q1 2020*. National Renewable Energy Laboratory (2021).

11. Shockley, W. & Queisser, H., Detailed balance limit of efficiency of p-n junction solar cells, *Journal of Applied Physics*, **32**, 510 (1961).

12. Wurfel, P. *Physics of Solar Cells: From Basic Principles to Advanced Concepts*. (John Wiley & Sons, 2005).

13. Schnitzer, I., Yablonovitch, E., Caneau, C. & Gmitter, T. J. Ultra-high spontaneous emission quantum efficiency, 99.7% internally and 72% externally, from AlGaAs/GaAs/AlGaAs double heterostructures. *Appl. Phys. Lett.*, **62**, 131–133 (1993).

14. Reinders, A., Verlinden, P., van Stark, W., Freundlich, A. *Photovoltaic Solar Energy – From Fundamentals to Applications*, (John Wiley & Sons, 2017).

15. Noufi, R. High Efficiency CdTe and CIGS Thin Film Solar Cells: Highlights of the Technologies Challenges, *2006 IEEE 4th World Conference on Photovoltaic Energy Conversion* (WCPEC-4) Waikoloa, Hawaii. (2006).

16. NREL. *Best Research-Cell Efficiency Chart*, https://www.nrel.gov/pv/cell-efficiency.html (2022)

17. Kojima, A., Teshima, K., Shirai, Y., Miyasaka, T. Organometal Halide Perovskites as Visible-Light Sensitizers for Photovoltaic Cells, *J. AM. CHEM. SOC.*, **131**, 6050-6051 (2009).

18. Jeong, J. et al. Pseudo-halide anion engineering for α-FAPbI3 perovskite solar cells. *Nature* **592**, 381–385 (2021).

19. Correa-Baena, J., et al. The rapid evolution of highly efficient perovskite solar cells, *Energy Environ. Sci.* **10**, 710-727 (2017).

20. WHO. *Lead poisoning and health*. http://www.who.int/news-room/fact-sheets/detail/lead-poisoning-and-health (2017).

21. Hoefler, S., Trimmel, G., Rath, T. Progress on lead-free metal halide perovskites for photovoltaic applications: a review, *Monatsh Chem* **148**, 795–826 (2017).

22. Serrano-Lujan, L. *et al.* Tin- and Lead-Based Perovskite Solar Cells under Scrutiny: An Environmental Perspective. *Adv. Energy Mater.* **5**, 1501119 (2015).

23. Saliba, M., Correa-Baena, J., Grätzel, M., Hagfeldt, A., Abate, A., Perovskite Solar Cells: From the Atomic Level to Film Quality and Device Performance, *Angew. Chem. Int. Ed.* **57**, 2554-2569 (2018).

24. Jiang, X. *et al.* One-Step Synthesis of $SnI_2 \cdot (DMSO)_x$ Adducts for High-Performance Tin Perovskite Solar Cells. *J. Am. Chem. Soc.* **143**, 10970–10976 (2021).

25. Ball, J. M. *et al.* Optical properties and limiting photocurrent of thin-film perovskite solar cells. *Energy Environ. Sci.* **8**, 602–609 (2015).

26. Luo, P. *et al.* Uniform, Stable, and Efficient Planar-Heterojunction Perovskite Solar Cells by Facile Low-Pressure Chemical Vapor Deposition under Fully Open-Air Conditions. *ACS Appl. Mater. Interfaces* **7**, 2708–2714 (2015).

27. Yang, S., Fu, W., Zhang, Z., Chen, H. & Li, C.-Z. Recent advances in perovskite solar cells: efficiency, stability and lead-free perovskite. *J. Mater. Chem. A* **5**, 11462–11482 (2017).

28. Zhang, C., Gao, L., Hayase, S. & Ma, T. Current Advancements in Material Research and Techniques Focusing on Lead-free Perovskite Solar Cells. *Chem. Lett.* **46**, 1276–1284 (2017).

29. Xu, P., Chen, S., Xiang, H.-J., Gong, X.-G. & Wei, S.-H. Influence of Defects and Synthesis Conditions on the Photovoltaic Performance of Perovskite Semiconductor $CsSnI_3$. *Chem. Mater.* **26**, 6068–6072 (2014).

30. Shi, T. *et al.* Effects of organic cations on the defect physics of tin halide perovskites. *J. Mater. Chem. A* **5**, 15124–15129 (2017).

31. Konstantakou, M. & Stergiopoulos, T. A critical review on tin halide perovskite solar cells. *J. Mater. Chem. A* **5**, 11518–11549 (2017).

32. Gupta, S., Cahen, D. & Hodes, G. How SnF_2 Impacts the Material Properties of Lead-Free Tin Perovskites. *J. Phys. Chem. C* **122**, 13926–13936 (2018).

33. Leijtens, T., Prasanna, R., Gold-Parker, A., Toney, M. F. & McGehee, M. D. Mechanism of Tin Oxidation and Stabilization by Lead Substitution in Tin Halide Perovskites. *ACS Energy Lett.* **2**, 2159–2165 (2017).

34. Diau, E. W.-G., Jokar, E. & Rameez, M. Strategies To Improve Performance and Stability for Tin-Based Perovskite Solar Cells. *ACS Energy Lett.* **4**, 1930–1937 (2019).

35. Zhou, Y., Yang, M., Pang, S., Zhu, K. & Padture, N. P. Exceptional Morphology-Preserving Evolution of Formamidinium Lead Triiodide Perovskite Thin Films via Organic-Cation Displacement. *J. Am. Chem. Soc.* **138**, 5535–5538 (2016).

2 Atmospheric Pressure Chemical Vapor Deposition

2.1 Motivation

The choice to study APCVD as a deposition technique was motivated by a desire to achieve scalability for tin-based perovskite solar cells. The desired perovskite film should be deposited uniformly, cheaply, and at the square-meter per minute scale. Given these conditions, one may consider potential deposition methods, some of which were identified in Chapter 1, and group them by their baseline operating pressure. This distinction is crucial for any mass production technique but especially so for solar panels. Solar panels, unlike televisions, laptop screens, or computer chips, must be produced with an annual quota on the magnitude of square miles to achieve commercial competitiveness. Given that fossil fuels accounted for roughly 16 TW-yrs of energy produced globally in 2017[1] and a 20% efficient solar panel with a capacity factor of 20% generates 40 W-yr/m^2, a solar panel factory making 10 square miles of solar panels per year produces 1.04 GW-yr or 0.0065% of the fossil fuel energy used each year. If humans built 33 such factories *every year*, we would be able to replace all fossil fuels used in 2020 (neglecting the fact that not all forms of energy are directly replaceable and that solar panels will need to be replaced every few decades) by 2050. Assuming 33 new factories per year is an overly optimistic figure (there were less than 600 automobile plants worldwide in 2012[2]), the manufacturing of solar panels must be cheap and fast.

This suggests avoiding the use of vacuum processing in solar panel manufacturing. Vacuum processing necessitates the implementation of batches, which is not agreeable with higher throughput, in-line manufacturing. The pumps, vacuum oil, and maintenance all contribute to a

cost that is absent under atmospheric pressure processing[3]. Additionally, the total processing time is directly coupled with the processing area – a larger batch size increases the pumping time to achieve a desired vacuum level. This hinders the unit economic gains of manufacturing at scale.

Ruling out any vacuum processing technique on the grounds of speed and cost issues, that leaves such atmospheric processes as solution and chemical vapor deposition. As mentioned in chapter 1, current state of the art PSCs are made via a solution deposition technique. The most efficient PSCs are made by spin-coating, but recent advances in solvent chemistries have enabled doctor blading techniques to deposit efficient PSCs on much larger areas than those permissible with spin-coating.[4] However, these techniques are still unproven on the meter scale, the scale pertinent to commercial production. Provided the growth rates are sufficient, APCVD is capable of depositing uniformly at the meter length scale.[3]

2.2 APCVD Principles

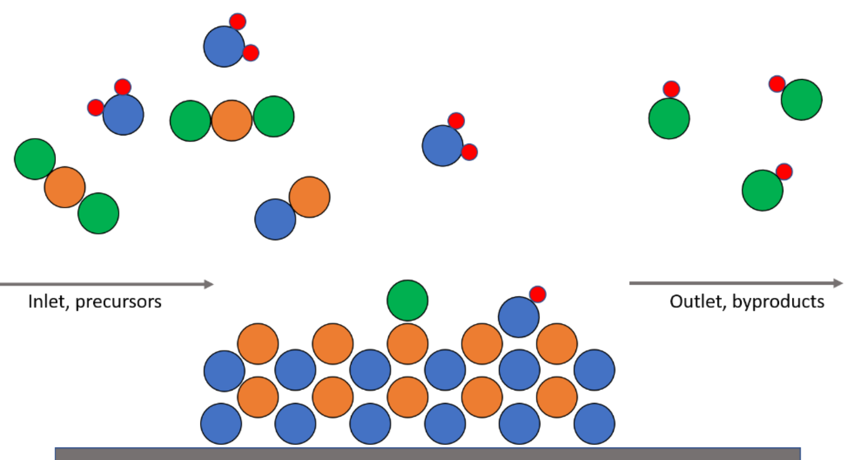

Figure 2-1: APCVD example diagram

APCVD, a subclassification of chemical vapor deposition (CVD), uses gaseous precursors at atmospheric pressure to produce thin films on a substrate by chemical reaction, as seen in Figure 2-1. Unlike physical vapor deposition (PVD) techniques, which use line-of-sight to control the deposition, CVD may be used to produce conformal films through diffusion of precursors near the surface. In an example CVD process, precursors may undergo ligand exchange with a partially reacted precursor on the surface (see the green "ligand" in Figure 2-1: APCVD example diagram) and chemisorb to the surface with the byproducts expelled from the reactor. Precursors may also adsorb to the surface. Both chemisorption and adsorption are controlled by surface temperature, stereodynamic effects of the precursor, and the availability of energetically favorable surface sites. A general model for the rate, r, of a CVD reaction (Equation $r=k\prod C_i^{n_i}$ #(2-1)) may depend on the concentration of precursors, C_i, just above the surface, the order of each precursor concentration in the chemical reaction, n_i, and the reaction rate constant, k (Equation (2-2)), which contains the temperature dependence via the activation energy, E_a, and any steric factor via the frequency factor, f.

$$r = k\prod C_i^{n_i} \tag{2-1}$$

$$k = f\exp\left(-\frac{E_a}{k_B T}\right) \tag{2-2}$$

Operating at atmospheric pressure affords high throughput of precursors to achieve high growth rates compared. However, high rates of gas-phase reactions may generate particles which deposit on the surface, reduce film adhesion, and generate pin-holes – tiny gaps in the film which

allow physical contact of two adjacent layers. This can be mitigated by reducing the temperature, reducing the precursor concentration, and heating the substrate hotter than the surroundings to enhance thermophoresis, a phenomenon by which a temperature gradient acts to buoy particles. Because of APCVD's susceptibility to uncontrolled gas-phase reactions, precursor residence times should be short, which implies using high flow rates and small chamber volumes. Under these conditions, the chemistry and fluid dynamics near the boundary layer, as shown in Figure 2-2, attain greater importance to the overall deposition process.

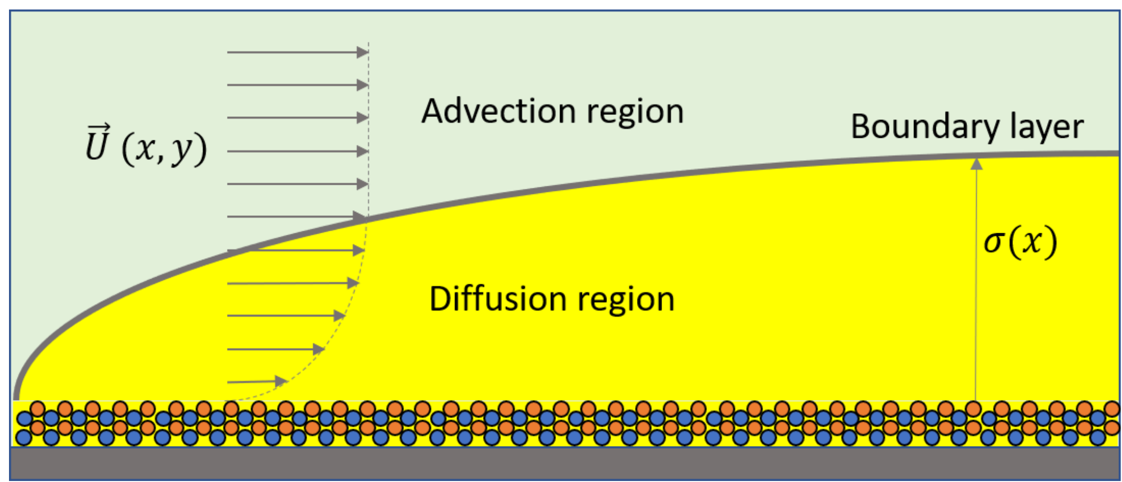

Figure 2-2: Boundary layer

This boundary layer separates the regions of the chamber into the advection and diffusion regions. In the former, the transportation of precursors to the substrate is controlled by advection, the bulk movement of gas, whereas in the latter, transport is limited by diffusion through the more stagnant gas close to the surface. The functional form of the boundary layer is often $\sigma(x) \propto \sqrt{x}$, where x is the distance along the substrate. The existence of the boundary layer originates in the velocity gradient between the free stream velocity far away from the surface and the zero velocity

at the surface where gas particles in thermodynamic equilibrium with the chamber surface momentarily come to rest.

A consequence of the precursor transport limitation in APCVD is the potential limitation of film growth, which similarly can be divided into two regions – transport limited and surface kinetics limited growth.

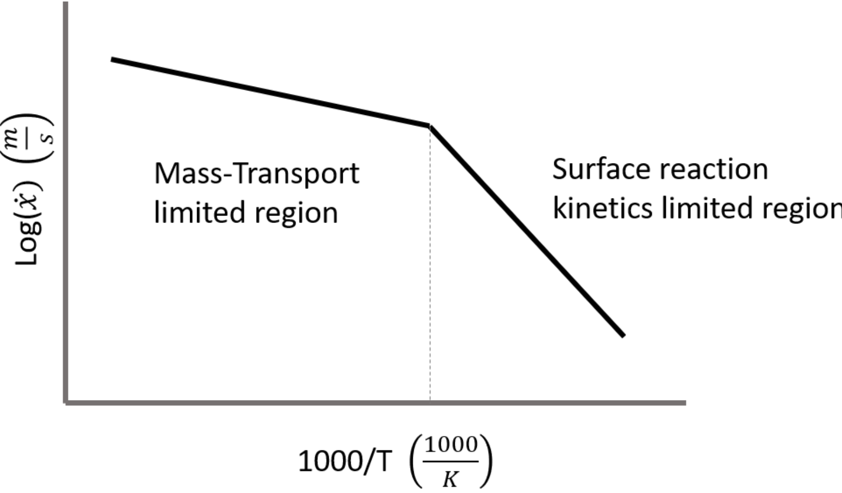

Figure 2-3: Film growth rate limited regions

From Figure 2-3, one may see that at cooler temperatures, the film growth rate is limited by the reaction rate. As the temperature increases, a cross-over point is reached where the film growth rate is limited by the diffusion of precursors to the surface. A further increase in temperature may lead to rapid gas-phase reactions, which dramatically increases the deposition rate and non-uniformity. The choice of region to operate in is not at all clear. If operating in the mass-transport limited region, one may achieve high growth rates, but the resultant film may be less uniform. The converse is true for operating in the surface reaction kinetics limited region. The choice depends on the application.

For making PSCs, many of the advantages of APCVD can be realized while several of the disadvantages can be minimized. Many commercial CVD processes operate furnaces in the several hundreds of degrees Celsius range, which bears a heavy energy and equipment cost. PSCs, however, need relatively low temperatures, in the range of room temperature (RT) to 200 °C, to achieve desirable film quality. This alleviates the need to have special, high-temperature equipment, prolongs the lifetime of the reactor, and reduces operating expenses. Furthermore, many commercial precursors are insufficiently volatile unless they are heated to high temperatures (> 200 ^{o}C). This again requires special equipment and increases the rate of precursor degradation. Fortunately, for the perovskite active layer, volatile precursors have been identified that permit their manipulation in the gas phase at temperatures below the reactor temperature. Consequently, the precursor vapors in the reactor are unlikely to reach saturation and precipitate or condense onto the substrate.

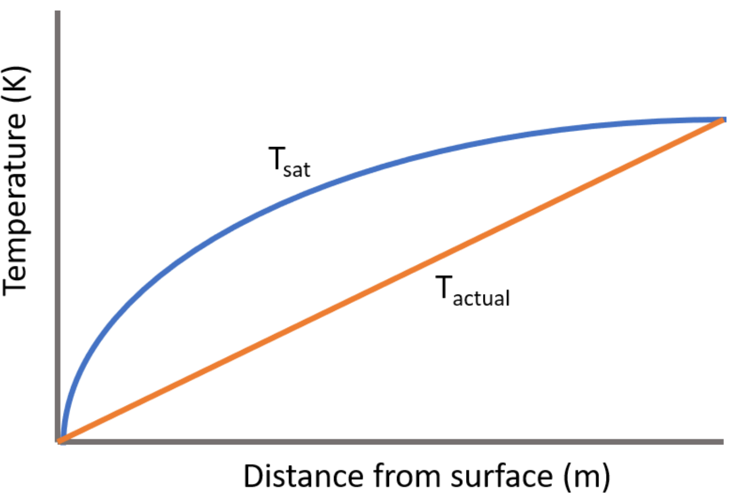

Figure 2-4: Example vapor saturation temperature vs actual temperature across the boundary layer

In an APCVD process where the substrate temperature is close to or less than the precursor source bubbler temperature, the actual temperature above the substrate may be below the vapor saturation temperature as seen in Figure 2-4.[3] This is a result of an increase in the concentration of precursor as the diffusion limited region is encountered. If the rate of precursor delivery into the reactor is greater than the rate of diffusion through the boundary, then the remaining precursor will exit through the outlet. However, this imbalance in advection and diffusion currents will increase the concentration of the precursor at the boundary layer above its free stream concentration, which effectively increases the saturation temperature necessary to maintain the excess precursor in the gas phase. If this saturation temperature increases above the actual temperature, the vapor will become supersaturated, and thermodynamics will drive the precipitation and dust formation of the excess precursor. Luckily, for PSCs, the vapor pressures of the chosen precursors are either gases at RT or are sufficiently volatile such that the substrate may be operated at temperatures well above the saturation temperature.

APCVD as a mass-manufacturing technique is not without its drawbacks. It does consume copious amounts of nitrogen and the mass-transport of the precursors has an added complexity over low-pressure techniques (low-pressure avoids turbulence all-together). Another often cited disadvantage of APCVD is oxygen contamination from the environment due to the high carrier gas density[3]. This enables even trace percentages of oxygen in the carrier gas to enter the reactor and corrupt the film stoichiometry. However, by using gas purification equipment and by raising the pressure of the reactor head space just above atmospheric pressure, the prevalence of oxygen in the carrier gas and diffusion of ambient oxygen through leaks in the reactor can be greatly minimized[3]. In sum, APCVD seems well-suited to addressing the concern of how to inexpensively mass-manufacture PSCs.

2.3 Precursor Selection

As mentioned in the previous section, precursors for APCVD should undergo a ligand exchange process that cleanly generates the desired product and volatile, inert byproducts that are easily removed from the reactor. Several desirable characteristics of APCVD precursors are listed in Table 2-1. Chief among these are volatility, thermal stability, and reactivity. Volatility of the precursor is important to ensure a wide operating temperature for the reaction – too low of volatility requires higher source temperatures which raises the minimum reactor temperature to avoid precursor condensation. Thermal stability is also important to avoid premature or unintended decomposition of the precursor, which may contribute to film contamination. Precursors with low thermal stability require lower source and reactor temperatures, thereby reducing the reactor maximum operating temperature. Lastly, reactivity is important, because a film will not be deposited if the precursors are insufficiently reactive in the operating temperature range.

Table 2-1: Desirable Precursor Characteristics

High volatility
High thermal stability
High/tunable reactivity
Non-toxic
Liquid
Inert byproducts
Inexpensive

The desired compounds to deposit for this thesis were methylammonium halides (MAX) and tin dihalides (SnX_2). For MAX, the methylammonium cation and halide anion could be obtained by the addition reaction of methylamine and an equivalent of hydrogen halide. For SnX_2, it was hypothesized that reacting a tin(II) compound with 2 equivalents of hydrogen halide would

successfully deposit SnX_2 (completed in two half reactions). Other routes may exist for either of these compounds, but exploration of possible alternatives in this thesis delivered little results.

2.3.1 Tin precursor selection

The choice of the tin(II) precursor to supply the desired Sn^{2+} ions to the SnX_2 lattice was determined using the guidelines of Table 2-1. The first consideration was whether the tin precursor would be sufficiently volatile. A chemical may be sufficiently volatile for a deposition under vacuum where the growth rate may be tolerably slow (< 10 nm/min) but not sufficiently volatile for a fast deposition process ($\sim$1,000 nm/min) under atmospheric pressure. In the case of APCVD for depositing solar cells, the later requirement must be met. A general rule for volatility sufficiency is whether the chemical has a vapor pressure of at least 0.1 Torr at or below the deposition temperature.[6] As described in Figure 2-4, delivering a precursor at a temperature *above* the deposition temperature may lead to inhomogeneous precipitation or condensation on the substrate. Therefore, the upper limit to the source temperature of the precursor should be the deposition temperature. For Sn^{2+} precursors, there are several available that meet this requirement.

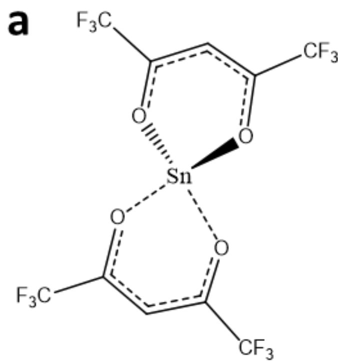

Bis(hexafluoroacetylacetonate)tin(II)
$C_{10}H_2O_4F_{12}Sn$
CAS #: 51319-99-4
Molecular Weight: 532.81 g
Appearance: white solid

b

Bis(acetylacetonate)tin(II)
$C_{10}H_{14}O_4Sn$
CAS #: 16009-86-2
Molecular Weight: 316.93 g
Appearance: orange/red liquid

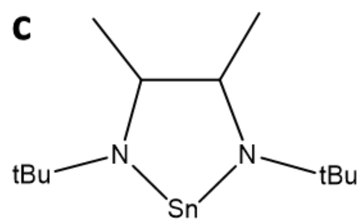

rac-1,3-di-tert-butyl-4,5-dimethyl-1,3-diaza-2-stannacyclopentane-2-ylidene
CAS #: 1268357-44-3
$C_{12}H_{26}N_2Sn$
Molecular Weight: 317.06 g
Appearance: orange solid

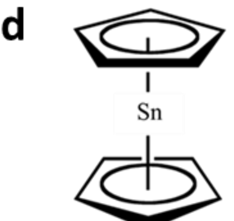

d

Stannocene
$C_{10}H_{10}Sn$
CAS #: 1294-75-3
Molecular Weight: 248.896 g
Appearance: White solid

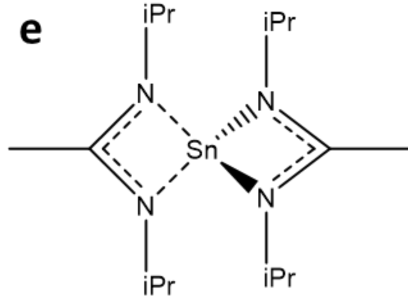

Bis(N,N'-di-i-propylacetamidinato)tin(II)
CAS #: 1421599-46-3
$C_{16}H_{34}N_4Sn$
Molecular weight: 401.18 g
Appearance: orange solid

Figure 2-5: List of select Sn^{2+} precursors that have sufficient volatility for use in APCVD.

Initial experiments used *rac*-1,3-di-tert-butyl-4,5-dimethyl-1,3-diaza-2-stannacyclopentane-2-ylidene, chemical c) in Figure 2-5, for its high volatility.[7] However, both c) and e) of Figure 2-5 have the potential for undesirable side reactions. In both precursors, the nitrogen on the ligands has sufficient basicity that after ligand exchange with a hydrogen halide, the free ligand is available to react with a second hydrogen halide to generate a non-volatile, ammonium salt byproduct, as shown below in reactions (2-3) and (2-4).[6]

tBu, NH, NH, tBu + HX → tBu, NH, $\overset{+}{N}H_2$, tBu X^- (2 − 3)

i-Pr, NH, H_3C, N, i-Pr + HX → i-Pr, NH_2^+ X^-, H_3C, N, i-Pr (2 − 4)

As these byproducts are unavoidable in a high-throughput process, the use of these two compounds was not considered further. Of the remaining three compounds, volatility increased in the order stannocene ($SnCp_2$) ≈ bis(acetylacetonate)tin(II) ($Sn(acac)_2$) < bis(hexafluoroacetylacetonate)tin(II) ($Sn(hfac)_2$), as seen in Figure 2-6 and Figure 2-7.

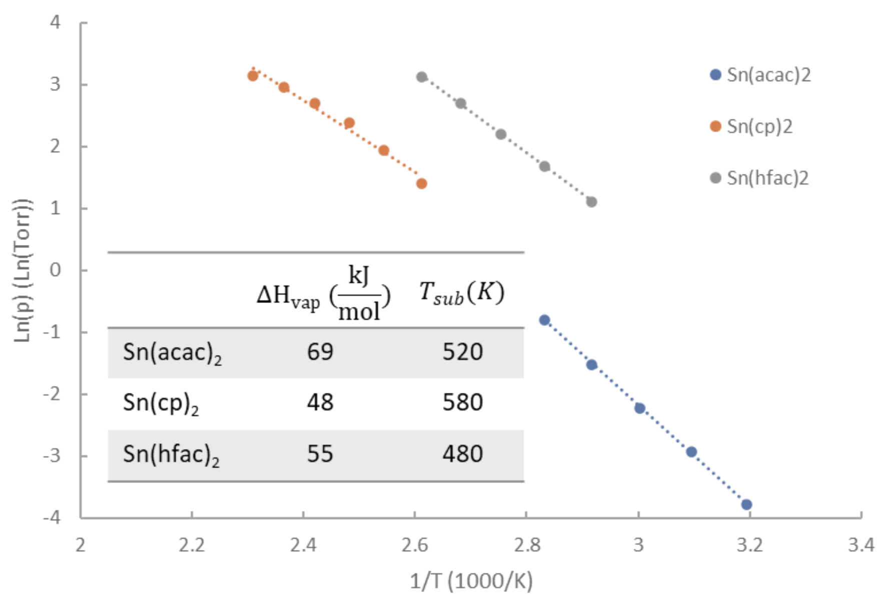

	ΔH_{vap} $(\frac{kJ}{mol})$	$T_{sub}(K)$
$Sn(acac)_2$	69	520
$Sn(cp)_2$	48	580
$Sn(hfac)_2$	55	480

Figure 2-6: Ln(p) vs 1/T for select Sn^{2+} precursors. The pressure values were calculated from TGA data assuming a Langmuir evaporation model[9-11] using benzyl alcohol as a calibration standard.

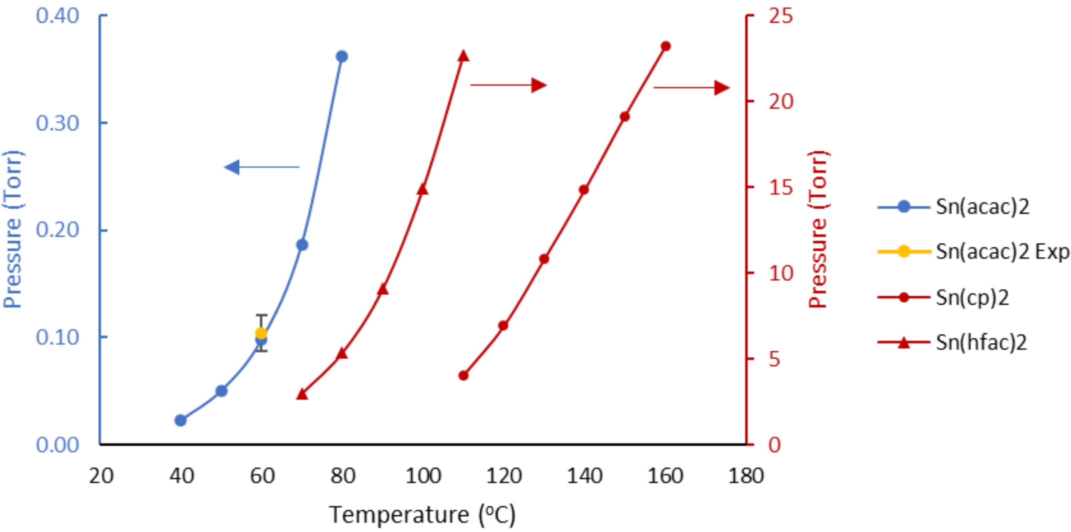

Figure 2-7: Vapor pressure estimates of $Sn(acac)_2$, $Sn(hfac)_2$, and $Sn(cp)_2$ from TGA measurements. The TGA vapor pressure estimates were derived assuming a Langmuir evaporation model using benzyl alcohol reference TGA data together with their respective vapor pressures.[9-12] The experimental value for the vapor pressure of $Sn(acac)_2$ at 60 °C was estimated from bubbling 250 sccm of N_2 through a $Sn(acac)_2$ bubbler at 60 °C for 120 min and collecting the vapor in a liquid nitrogen cold trap. The $Sn(acac)_2$ was transferred and weighed inside a glovebox. The error estimates include ±10 mg.

The Clausius-Clapeyron plot of Figure 2-6 and the vapor pressure curves of Figure 2-7 were derived assuming a Langmuir evaporation model using stepwise isothermal TGA data of the compounds.[9-11] Langmuir's evaporation model (Equation (2-5)) relates the difference between the partial pressure of the compound in the gas phase above the liquid surface (p_v) and an idealized partial pressure of the compound vapor dissolved in the liquid (p_l) to the rate of mass loss (dm/dt) per unit area across the liquid-vapor boundary line (Figure 2-8), where M is the molar mass, R is the ideal gas constant, and T is the temperature.

$$\frac{dm}{dt} = (p_v - p_l)\sqrt{\frac{M}{2\pi RT}} \tag{2-3}$$

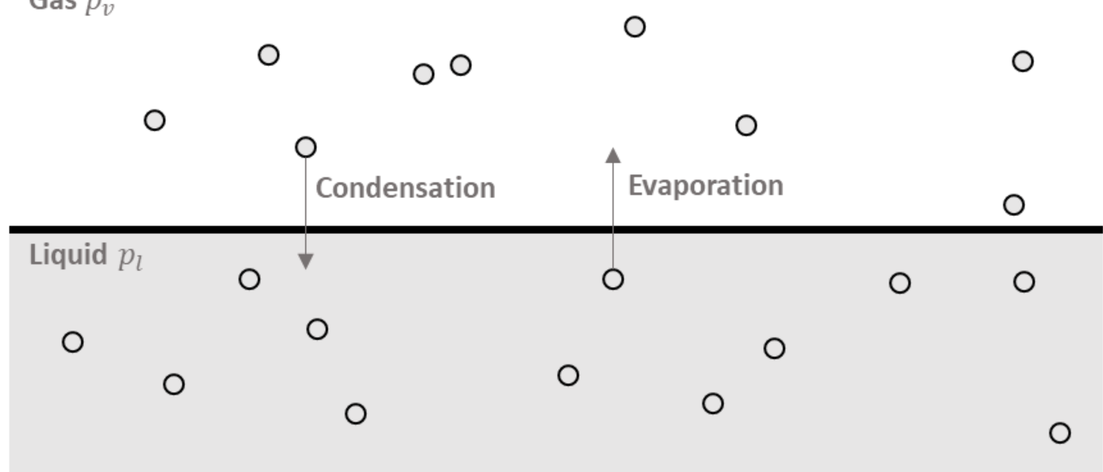

Figure 2-8: Langmuir's evaporation model. The model idealizes evaporation as vapor dissolved in the liquid phase escaping the liquid-gas boundary. Condensation is the reverse process.

Using mass loss data from stepwise isothermal TGA experiments, assuming the compound partial pressure in the gas phase is ~ 0 due to the sweeping action of the purging, and assuming negligible effect of the boundary layer,[11] inert gas (N_2) under normal TGA operating conditions, Equation (2-5) can be re-written as

$$p_l = -\frac{dm}{dt}\sqrt{\frac{2\pi RT}{M}} \tag{2-4}$$

Taking logarithms of both sides and expanding the right-hand side, Equation (2-6) can be re-written as

$$\mathrm{Log}_{10}(p_l) = a \times \mathrm{Log}_{10}\left(-\frac{dm}{dt}\sqrt{\frac{T}{M}}\right) + b \tag{2-5}$$

where a and b are constants of the TGA instrument and need to be calibrated using a reference compound. Ideally, a and b would equal 1 and $\sqrt{2\pi R}$, respectively, but p_v is not exactly 0 in a real TGA experiment and the Langmuir model describes an equilibrium whereas isothermal TGA data describes a steady-state process. a and b are fitting parameters to account for these deviations from the model. With the TGA instrument properly calibrated, the pressure was estimated from the mass loss rate under stepwise isothermal conditions.

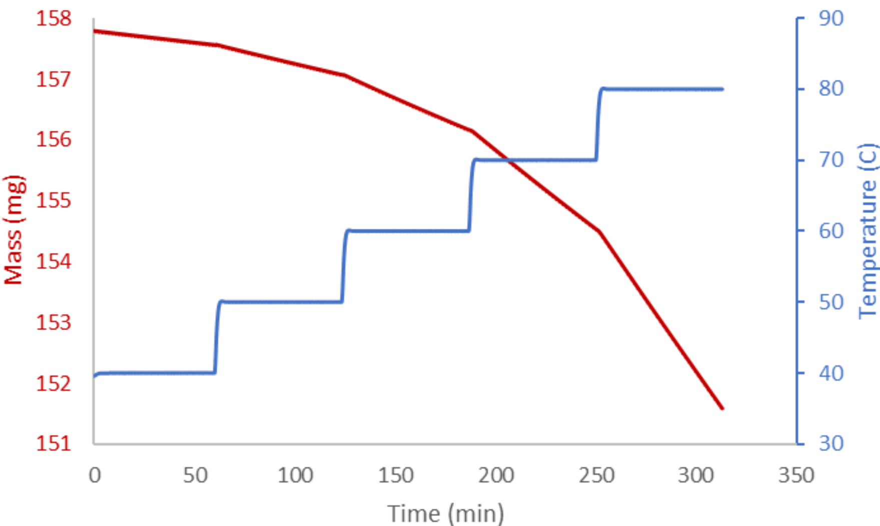

Figure 2-9: Example stepwise isothermal TGA plot of $Sn(acac)_2$

The vapor pressure of $Sn(acac)_2$ at 60 °C was also estimated by bubbling N_2 through $Sn(acac)_2$ and collecting the vapors in a cold trap at -196 °C according to Figure 2-10.

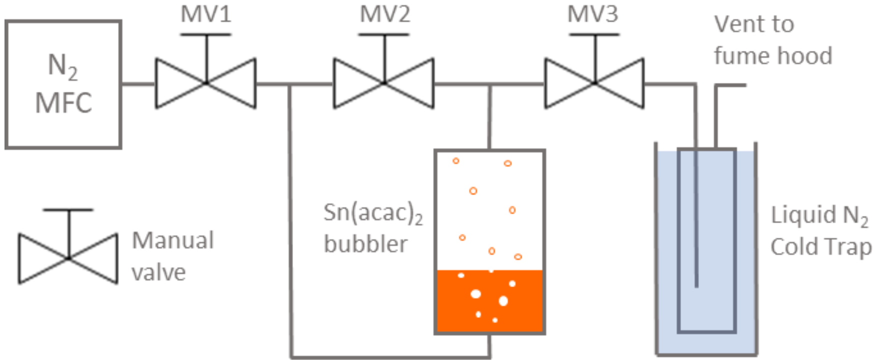

Figure 2-10: Experimental setup to estimate the vapor pressure of $Sn(acac)_2$

In this experiment, the $Sn(acac)_2$ bubbler was wrapped in heating tape and set to 60 °C. The tubing connecting the tin bubbler to the cold trap was heated in the range 70-80 °C to avoid condensation. The MFC delivered 250 sccm of N_2 (> 99.999%) through a porous metal sparger submerged in the liquid tin precursor. The N_2 carrier gas then delivered the entrained precursor to

the cold trap. The series of manual valves helped redirect the flow and prevent unintended exposure of the tin bubbler to air. After flowing N_2 for 120 min, the cold trap was detached and allowed to warm. A slight vacuum was applied after detachment to avoid over pressurizing the internal volume prior to transfer to a glovebox. Inside the glovebox, the trapped $Sn(acac)_2$ was collected and weighed. Assuming the bubbler was 100% efficient in saturating the N_2 with $Sn(acac)_2$, the partial pressure of $Sn(acac)_2$ at 60 °C could be estimated by comparing the total moles of $Sn(acac)_2$ delivered to the cold trap to the total moles of N_2 delivered. The results of the calculations are tabulated in Table 2-2.

Table 2-2: $Sn(acac)_2$ Vapor Pressure Experiment

Time (min)	**Flow Rate (sccm)**	**Mass $Sn(acac)_2$ (mg)**	**$Sn(acac)_2$ (moles$\times 10^{-4}$)**	**N_2 (moles)**	**Partial Pressure (torr)**
120	250	63 ± 10	2.0 ± 0.3	1.5	0.10 ± 0.017

Given that $Sn(acac)_2$ has a sufficient vapor pressure in the temperature range of interest, is commercially available, and is a liquid, this compound was selected for further study. The synthesis protocol for $Sn(acac)_2$ is straightforward. This is important as even though the starting chemicals may be inexpensive, a complicated, multi-step process will greatly increase overall cost. $Sn(acac)_2$ may be synthesized from $SnCl_2$ and sodium acetylacetonate (Na(acac)) in tetrahydrofuran (THF) with precipitation of sodium chloride (NaCl) according to reaction (2-8). The product may be purified by distillation or sublimation.

$$\mathrm{SnCl_2 + 2Na(C_5H_7O_2) \rightarrow 2NaCl + Sn(C_5H_7O_2)_2} \tag{2-6}$$

One noteworthy difference between $Sn(acac)_2$ and $Sn(hfac)_2$ is the much-reduced acidity of the acac ligand compared to the hfac ligand ($pK_a \approx 9$ vs $pK_a = 4.35$).[14] This difference is due to the stronger inductive effect of the CF_3 groups compared to the CH_3 groups. While the acac and hfac ligands form two tautomers – keto and enolic forms – the configuration of lowest energy is the enolic form in the gas phase.

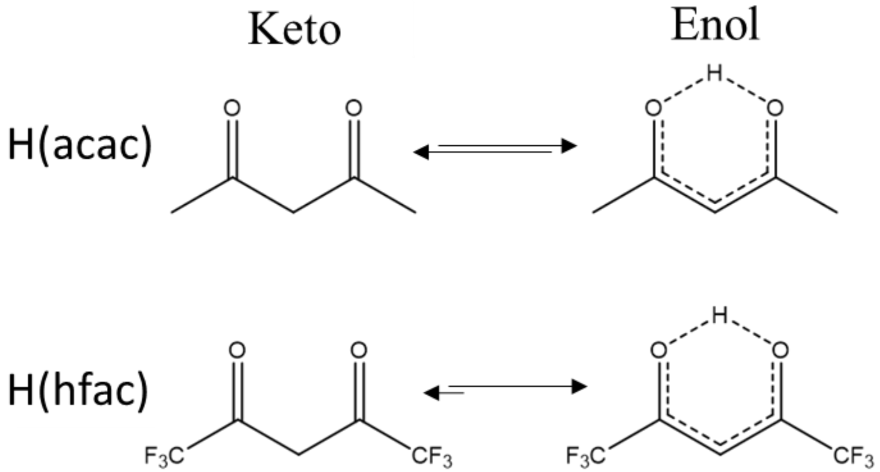

Figure 2-11: Tautomers of acetylacetone and hexafluoroacetylacetone

Sn(acac)$_2$ was also found to be stable within the desired reactor operating temperature range, ≤ 200 °C, on the timescale of minutes. The TGA ramp data shown in Figure 2-12 suggests $Sn(acac)_2$ could be used as a CVD precursor below 200 °C. Approximately 20% residual mass is evident when the temperature increases beyond 200 °C. The degree of decomposition in the reactor depends strongly on temperature, residence time, and the chemical environment. Finally, given $Sn(acac)_2$'s accessibility of the metal center, it was expected that the compound would show high reactivity to hydrogen halides. DFT calculations were performed to estimate the activation energy of this reaction and are reported in a later chapter.

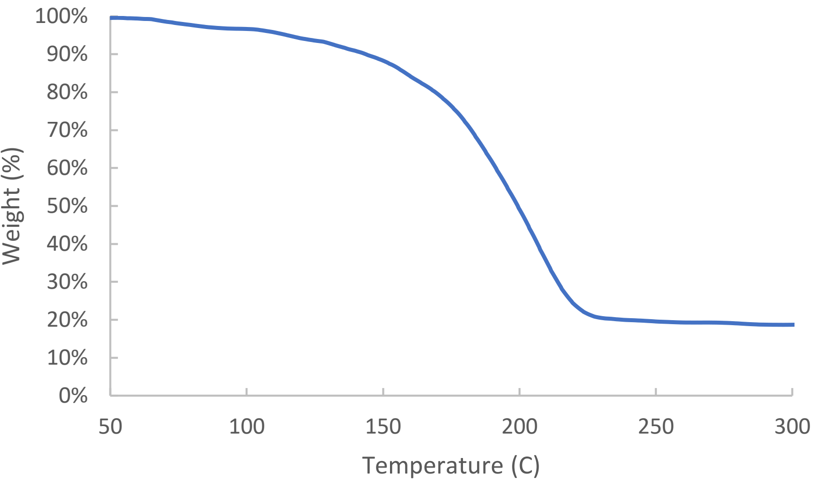

Figure 2-12: TGA ramp data for $Sn(acac)_2$ at a ramp rate of 10 °C/min. The initial weight was 30 mg. The small ripples in the plot are due to instrument errors.

2.3.2 Hydrogen halide selection

To form the MAX, SnX_2, and perovskite compound, a halide anion source is required. The fluoride (F^-) anion is too small to stabilize the perovskite crystal structure using either Sn^{2+} or Pb^{2+} as the metal center and was not considered. Chloride (Cl^-) and bromide (Br^-) could be delivered using hydrogen chloride (HCl) and hydrogen bromide (HBr), both inexpensive and commercially available gases compatible with MFCs. Both are thermally stable and very reactive and would form volatile byproducts with $Sn(acac)_2$, namely acetylacetone – H(acac).

Hydrogen iodide (HI) however, was not commercially available. Substituting hydrogen for a methyl group to use iodomethane – the simplest iodoalkane – poses serious reactivity challenges at the temperatures of interest (≤ 200 °C). The methyl group is much less likely to react with the acetylacetonate ligand ($acac^-$) than hydrogen. Instead, hydrogen iodide was made in *in situ* by reacting iodine (I_2) with a silane[15]. Under conditions of excess iodine, this process can generate a high yield of HI as shown in reaction (2-9).[16]

$$\mathrm{Et_3SiH} + \mathrm{I{-}I} \longrightarrow \mathrm{Et_3SiI} + \mathrm{H{-}I} \qquad (2\text{-}7)$$

In the first experiment, N_2 (> 99.999%) passed through a bubbler containing iodine (I_2) crystals after drops of triethylsilane (Et_3SiH) in tetradecane were added. The outlet of the bubbler was placed beneath the water line of a double-necked flask with the pH of the water continuously recorded with a digital pH meter (Oakton).

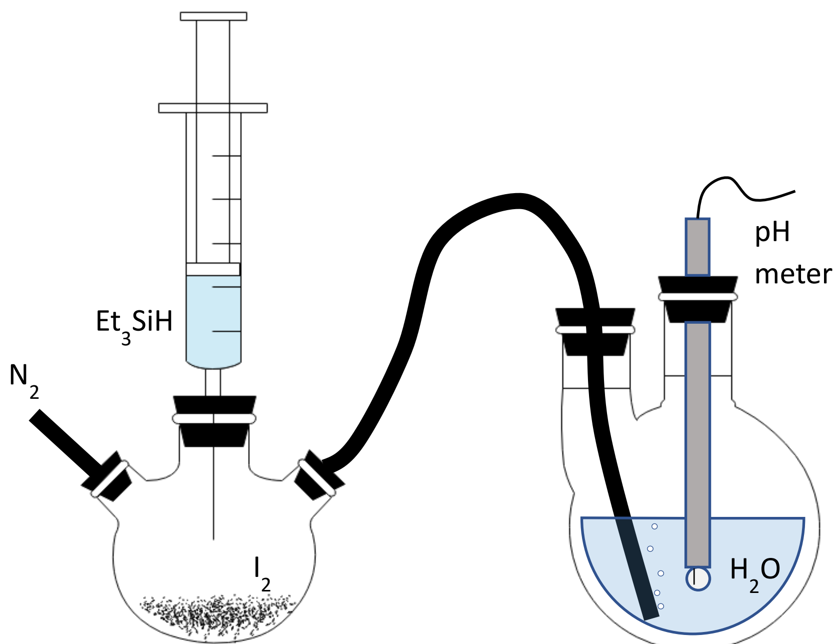

Figure 2-13: Test apparatus for measuring HI production from Et_3SiH injection into excess I_2. In this test, nitrogen was introduced into the triple-necked flask containing I_2 as drops of Et_3SiH were added. The contents of the flask were continuously flushed into the second flask containing 1000 mL of water.

The reaction setup depicted in Figure 2-13 generated HI as measured by a change in pH (5.38 pH → 4.02 pH after 1 drop of triethylsilane-tetradecane solution). However, achieving a constant flux of HI was challenging in this setup. Additionally, the syringe needle used to deliver the Et_3SiH often became clogged with iodine crystals if sufficient time was allowed to pass between experiments. To increase the control of HI delivery, the process depicted in Figure 2-14 was developed whereby a rotameter delivered N_2 carrier gas through MV_1 into a bubbler containing Et_3SiH. The Et_3SiH entrained in the N_2 carrier gas was then delivered into an iodine bubbler where the I_2 vapor and solid would react with the Et_3SiH to form HI. The outlet of the iodine bubbler connected to a cold trap to remove the iodine from the vapor stream. The outlet of the cold trap connected to the reactor.

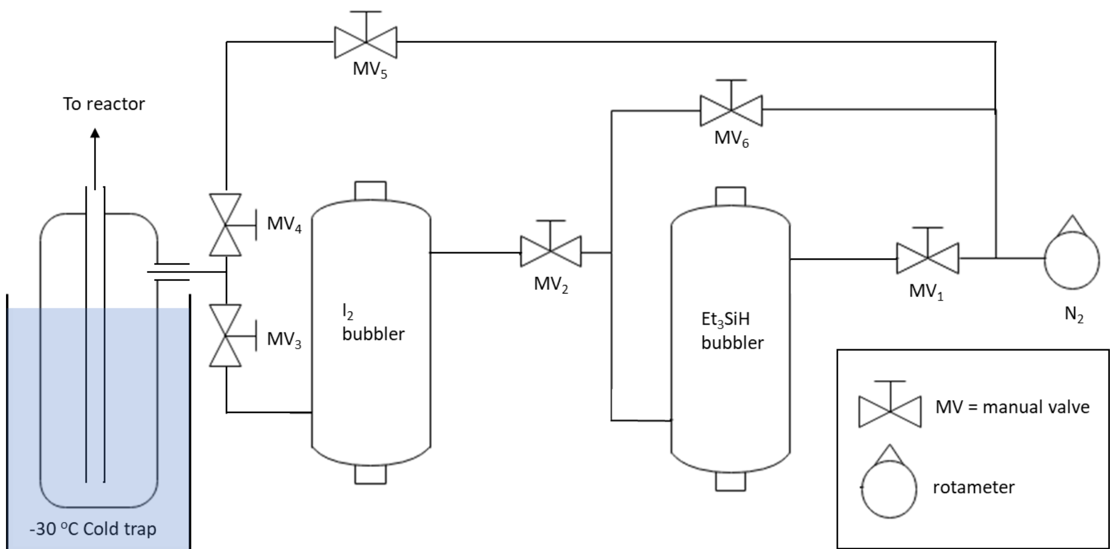

Figure 2-14: *In situ* HI generation schematic

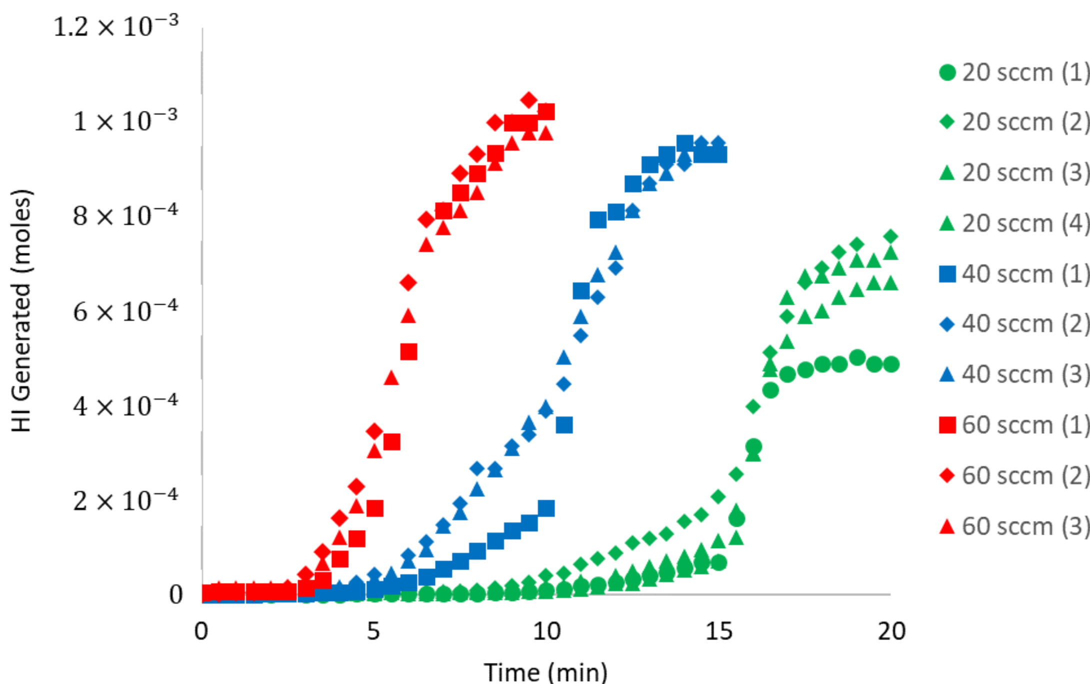

Figure 2-15: Data on hydrogen iodide generation from the process scheme depicted in Figure 2-14. The HI generated was bubbled into a reservoir of water using N_2 carrier gas at different flow rates of 20, 40, and 60 sccm and repeated at each N_2 flow rate to observe the consistency of generation. The effect of the experiment was to demonstrate that HI could be generated *in situ* in this manner.

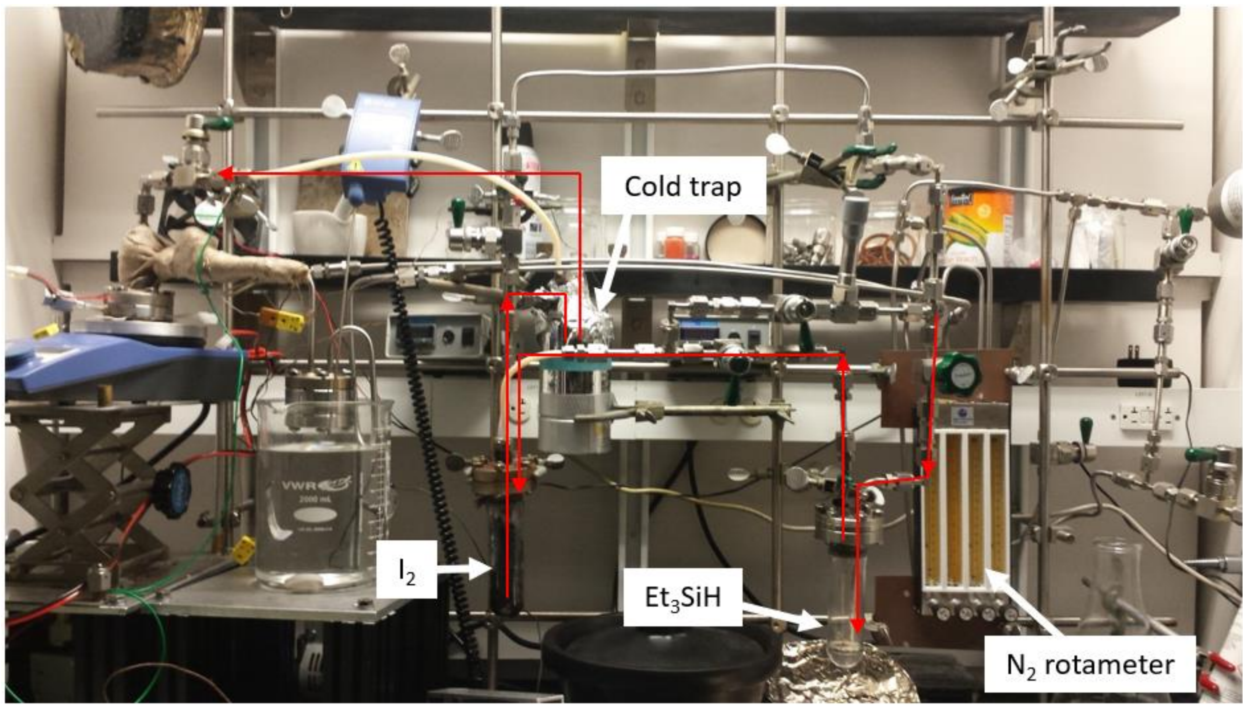

Figure 2-16: Reactor with the HI generation precursors and equipment installed for the scheme in Figure 2-14. The red line delineates the path from the starting N_2 source to delivering HI to the reactor.

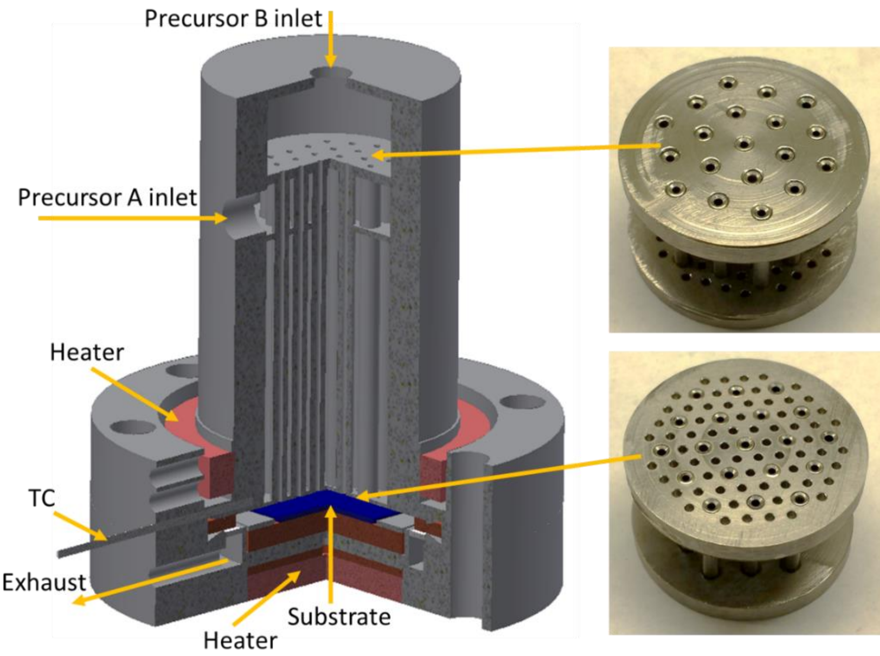

Figure 2-17: Showerhead reactor diagram for deposition tests using $Sn(acac)_2$ and methylamine (MA) (Precursor A inlet) and HI (Precursor B inlet). The substrate holder was magnetically coupled to a stir-plate (not shown) to enable substrate rotation.

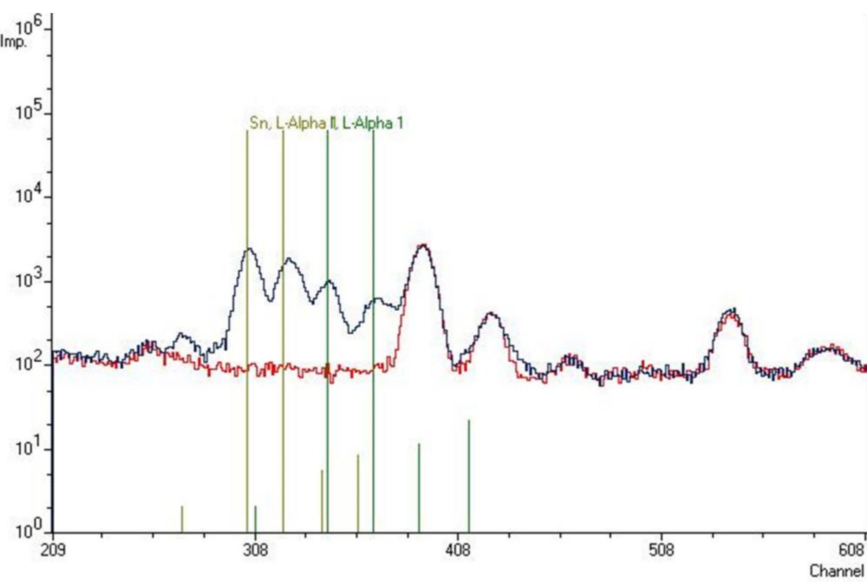

Figure 2-18: X-Ray Fluorescence (XRF) spectroscopy result from the reaction of $Sn(acac)_2$ and HI using the reactor in Figure 2-17. Evidence of Sn and I in the film confirms the delivery of both precursors to the substrate.

This *in-situ* HI generation scheme was successful in delivering HI to the reactor as determined by x-ray fluorescence spectroscopy (XRF) characterization of the resulting films from the reaction of $Sn(acac)_2$ and HI (Figure 2-18). The reaction was conducted in the reactor depicted in Figure 2-17. In this reactor, the generated HI entered from the top (Precursor B inlet) and either methylamine (MA) or $Sn(acac)_2$ entered from the side (Precursor A inlet). The HI flowed through the 1/8" OD tubing to the headspace above the substrate where it was allowed to react with MA or $Sn(acac)_2$ entering through the smaller inlet holes. The reactor was equipped with heaters on top and on bottom to set a uniform temperature measured with a thermocouple (TC). The substrate was magnetically coupled with samarium cobalt magnets to a hotplate to enable rotation. The aim of the rotation was to assist deposition uniformity.

Despite the success in generating and delivering HI to the reactor, consistent and timely *in-situ* generation remained challenging. To circumvent these difficulties, a new reactor design with

HI generation *ex situ* was used. This allowed easier generation, purification, and more accurate delivery by using a mass flow controller (MFC).

Table 2-3: HI Generation Protocol

Description	Manipulation
Cool *the 1st cold trap to* $\sim 0\,°C$ *and the 2nd cold trap to -196 °C*	Place the 1st cold trap under ice water; place the 2nd cold trap in a liquid nitrogen dewar
Reduce *the pressure in the cold traps and heating lines to* $\sim 50\ torr$	Open MV3, MV4, MV6, MV8 and pull vacuum
Close *the valve after the 2nd cold trap to collect the hydrogen iodide*	Close MV4
Expose *the heated gas lines to* I_2 *and* Et_3SiH	Open MV1 and MV2
Wait *to allow the* I_2 *and* Et_3SiH *to diffuse and react*	Wait the *X* minutes to generate the desired amount of hydrogen iodide. Monitor the pressure at PG1 to avoid overpressure
Stop *the reaction and wait until all the products and byproducts are collected*	Close MV1 and MV2 and wait ca. 5 more minutes
Shut *off the 1st cold trap from the 2nd cold trap*	Close MV3
Pump *and purge out the storage cylinder to remove adventitious oxygen*	Open MV6, MV7, and MV8 to alternating vacuum and N_2 3x to pump/purge the storage cylinder. Open MV5 at the final pump down to a pressure of <1 torr
Shut *off the storage cylinder from vacuum and expose the storage cylinder to the 2nd cold trap*	Close MV8 and open MV4
Remove *the liquid nitrogen dewar from the 2nd cold trap to allow it to gently warm paying careful attention to the pressure measured at PG2*	Remove the liquid nitrogen dewar from the 2nd cold trap
When *the desired hydrogen iodide pressure is achieved, close off the gas cylinder from the 2nd cold trap and allow the remaining hydrogen iodide to vent*	Close MV7 and open MV8 to vacuum with acid scrubbing
Disconnect *the pressure gauge and 2nd cold trap from the storage cylinder*	Close MV5 and MV4.
Connect *MV6 to the reactor*	Disconnect MV6 from the generator and connect it to the reactor
Pump/purge *the trap volume between MV6, MV7, and MV8 as well as the line downstream to the hydrogen iodide MFC*	Open MV8 and pump/purge with N_2 and vacuum 3x
Backfill *the storage cylinder to dilution pressure in* N_2	Fill the storage cylinder with N_2 to the desired dilution pressure and close MV7
Pump *out the backfilled* N_2 *in the trap volume between MV8, the storage cylinder, and the MFC*	Switch to vacuum with MV8 open
Shut *off the system from vacuum and open the storage cylinder to use the diluted hydrogen iodide*	Close MV8 and open MV7

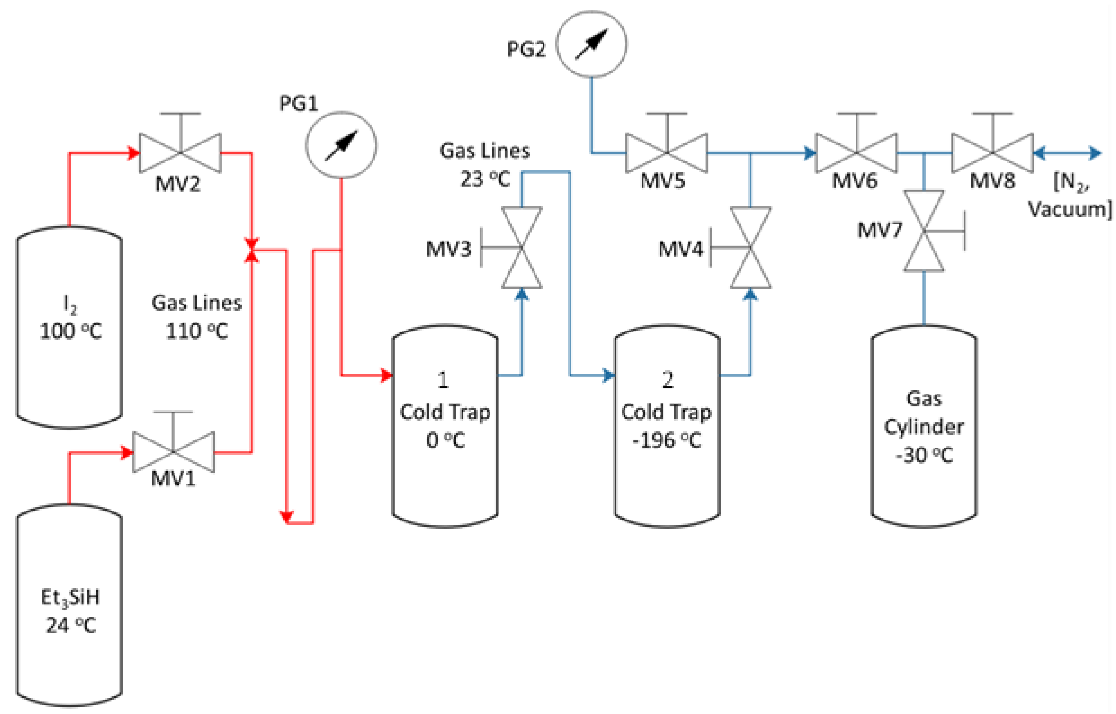

Figure 2-19: HI generation schematic for *ex situ* generation and storage

The protocol for generating hydrogen iodide is described in detail in Table 2-3 with the reference diagram shown in Figure 2-19. The storage cylinder (Figure 2-20) was equipped with a N_2 cooling coil and vacuum insulated jacket to allow cold storage when not in use to slow the rate of decomposition into H_2 and I_2.[17] The temperature was sensed using a resistance temperature detector (RTD) attached to the bottom of the storage cylinder. The RTD was used with a proportional-integral (PI) feedback loop and valve (not shown) connected between the gas cylinder and vacuum pump to set the temperature of the gas cylinder by opening and closing the valve. When the valve was open, the vacuum at one end of the cooling coil pulled liquid nitrogen into the gas phase and through the transfer line surrounding the gas cylinder, thus cooling the cylinder. When the valve closed, the transfer ceased, and the cylinder slowly warmed.

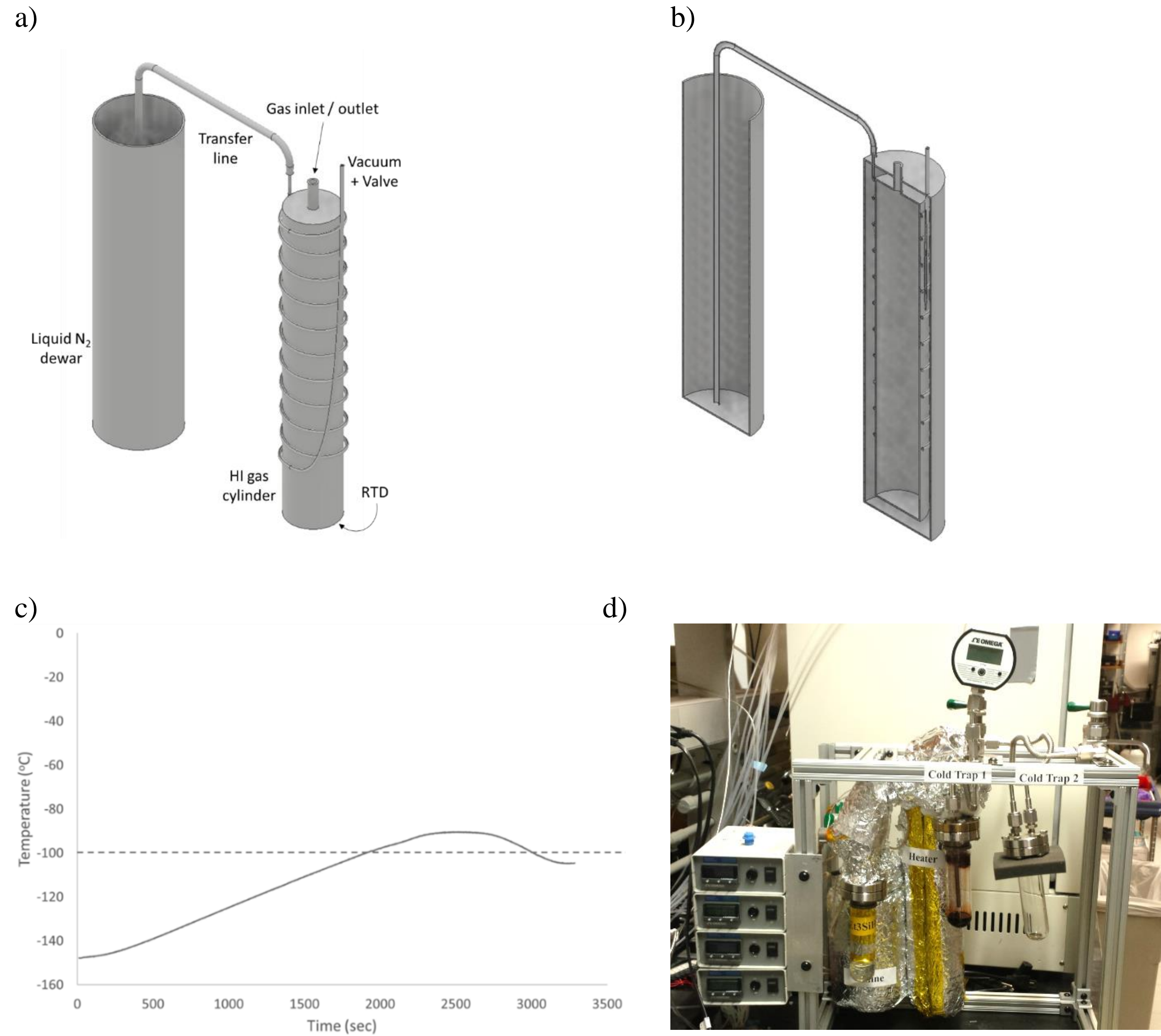

Figure 2-20: a) Computer aided drafting (CAD) model of the HI storage cylinder system. b) Section-view of a) showing how liquid nitrogen would be pulled from the bottom of the Dewar through the transfer line wrapped around the gas cylinder, which is insulated with a vacuum jacket. c) Plot of the temperature of the HI gas cylinder after the temperature setpoint was changed from the lowest achievable value (-150 ^{o}C) to -100 ^{o}C. The temperature eventually settled down to 100 $\pm$ 5 ^{o}C. The temperature was recorded with a resistance temperature detector (RTD) located at the bottom of the gas cylinder. d) Image of HI generator.

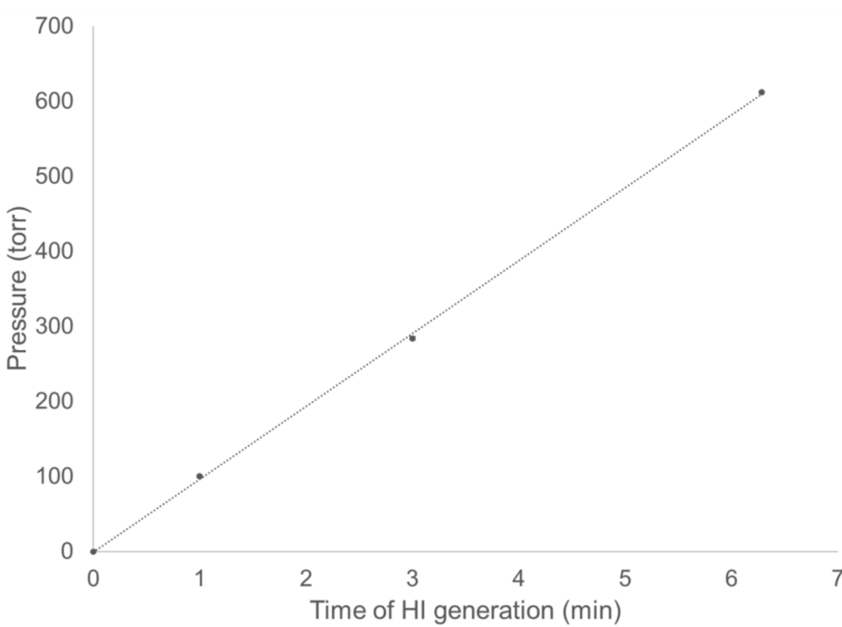

Figure 2-21: Calibration of the HI generator. The time of HI generation is the number of minutes the Et_3SiH and I_2 bubbler valves were open concurrently. The ordinate is the final HI pressure in the storage cylinder after allowing the 2nd cold trap of Figure 2-19 to warm and before dilution with N_2. The rate of HI generation is very nearly 100 torr / min of Et_3SiH and I_2 exposure.

Figure 2-21 demonstrates the consistency of HI generation. With cold storage and the use of an MFC, this latest design represented a significant advantage over the initial *in-situ* generation scheme. This work demonstrates a useful and repeatable process for generating HI to use in an APCVD reactor. However, for the purpose of applying the technique of APCVD to the fabrication of perovskite-related films, HI was not used further in this thesis. Instead, HBr was used to develop the APCVD process for making perovskite-related films MABr and $SnBr_2$ as HBr is commercially available with 99.999% purity (Matheson Gas).

2.3.3 Methylamine Selection

As mentioned in Chapter 1, a stable perovskite unit cell has the formula ABX_3 where A is a monovalent cation. The best performing perovskite absorbers have used cesium (Cs^+),

methylammonium (MA^+), formamidinium (FA^+), and guanidinium (GA^+), as shown in Table 2-4. Because methylamine (MA) can be readily protonated by HX, is commercially available, and is easily manipulated in the gas phase, it was selected for further study in developing the APCVD process and reactor to make MABr. The other A-site candidates listed in Table 2-4 are not commercially available in their neutral forms with sufficient volatility.

Table 2-4: A-site cation ionic radii[18,19]

Cesium (Cs^+)	1.8
Methylammonium (MA^+)	2.17
Formamidinium (FA^+)	2.53
Guanidinium (GA^+)	2.78

2.4 Conclusion

The chapter discussed the principles of APCVD, MABr and $SnBr_2$ precursor selections, and possible synthetic strategies to make such precursors for future work. $Sn(acac)_2$ was investigated and selected as suitable tin(II) compound because of its relatively high volatility, thermal stability up to 200 °C, accessibility of the tin center, and inexpensive synthesis. While a novel platform was developed for synthesizing and storing HI on demand, HBr was used for the remainder of this thesis as it is commercially available as a highly purified gas. Finally, MA was chosen for similar reasons – it is commercially available and easily manipulated with MFCs.

2.5 References

1. EIA. *International Energy Outlook 2021*, website: https://www.eia.gov/outlooks/ieo/index.php (2021).

2. Statista. Number of automobile manufacturing plants of the global automotive industry from 2000 to 2012. website: https://www.statista.com/statistics/266855/automobile-plants-of-the-global-automotive-industry/ (2018).

3. Woods, L. & Meyers, P., *Atmospheric Pressure Chemical Vapor Deposition and Jet Vapor Deposition of CdTe for High Efficiency Thin Film PV Devices: Final Technical Report*. National Renewable Energy Laboratory (2002).

4. Deng, Y. *et al.* Surfactant-controlled ink drying enables high-speed deposition of perovskite films for efficient photovoltaic modules. *Nat Energy* **3**, 560–566 (2018).

5. Proscia, J. & Gordon, R. G. Properties of fluorine-doped tin oxide films produced by atmospheric pressure chemical vapor deposition from tetramethyltin, bromotrifluoromethane and oxygen. *Thin Solid Films* **214**, 175–187 (1992).

6. Hampden-Smith, M. J. and Kodas, T. T. Chemical Vapor Deposition of Assorted Metals. in *The Chemistry of Metal CVD* (eds. Hampden-Smith, M. J. and Kodas, T. T.) 357–427 (Wiley-VCH Verlag GmbH, Germany, 1994).

7. Kim, S. B., Sinsermsuksakul, P., Hock, A. S., Pike, R. D. & Gordon, R. G. Synthesis of N-Heterocyclic Stannylene (Sn(II)) and Germylene (Ge(II)) and a Sn(II) Amidinate and Their Application as Precursors for Atomic Layer Deposition. *Chem. Mater.* **26**, 3065–3073 (2014).

8. Heasley, R., Chang, C. M., Davis, L. M., Liu, K. & Gordon, R. G. Vapor deposition of copper(I) bromide films via a two-step conversion process. *Journal of Vacuum Science & Technology A: Vacuum, Surfaces, and Films* **35**, 01B109 (2017).

9. Cuddy, M. F., Poda, A. R. & Chappell, M. A. Estimations of Vapor Pressures by Thermogravimetric Analysis of the Insensitive Munitions IMX-101, IMX-104, and Individual Components. *Propellants, Explosives, Pyrotechnics* **39**, 236–242 (2014).

10. Giani, S., Riesen, R. & Schawe, J. E. K. An Indirect Method for Vapor Pressure and Phase Change Enthalpy Determination by Thermogravimetry. *Int J Thermophys* **39**, 84 (2018).

11. METTLER TOLEDO. Determination of vapor pressure and the enthalpy of vaporization by TGA. *Thermal Analysis UserCom 38* (2014).

12. Dreisbach, R. R. & Shrader, S. A. Vapor Pressure–Temperature Data on Some Organic Compounds. *Ind. Eng. Chem.* **41**, 2879–2880 (1949).

13. Lewczyk, D. C. *et al.* Kinetic Treatment of Evaporation via Thermogravimetric Analysis: The Case of D -Limonene. *Ind. Eng. Chem. Res.* **59**, 15069–15074 (2020).

14. Stary, J. and Liljenzin, J. O. Critical Evaluation of Equilibrium Constants Involving Acetylacetone and Its Metal Chelates. *Pure & Appl. Chem*. **54**. 2557—2592 (1982)

15. Deans, D. R., Eaborn, C. Organosilicon Compounds. Part I X . The Reaction between Iodine and trisubstituted silanes. *J. Chem. Soc.* **0.** 3169-3173 (1954)

16. Voronkov, M. G., and Yu. I. Khudobin. Reaction of Trialkylsilanes with Iodine and Hydrogen Iodide. *Bulletin of the Academy of Sciences of the USSR Division of Chemical Science* **5**, 823–28 (1956).

17. Taylor, H. A. The Decomposition of Hydrogen Iodide. *J. Phys. Chem.* **28**, 984–991 (1923).

18. Cohen, B. N., Labarca, C., Davidson, N., Lester, H. A. Mutations in M2 alter the selectivity of the mouse nicotinic acetylcholine receptor for organic and alkali metal cations. *Journal of General Physiology* **100**, 373–400 (1992)

19. Kieslich, G., Sun, S. & Cheetham, A. K. An extended Tolerance Factor approach for organic–inorganic perovskites. *Chem. Sci.* **6**, 3430–3433 (2015).

3 APCVD Reactor Development

3.1 Motivation

As discussed in Chapter 2, an ideal deposition method for producing solar panels at scale is APCVD. APCVD is a proven technique for depositing a wide variety of thin films at the industrial level.[1-5] What the ideal APCVD reactor design should be requires knowledge of both cost drivers for the solar panels and techno-economic manufacturing limitations. As silicon cell prices have dropped over the past decade due to reductions in polysilicon prices and scale-up of panel production, the cost drivers for solar panels have shifted from the cell manufacturing to the balance of module, which includes the glass and framing. The long-term potential for silicon-based solar panels predicts that the balance of module (BOM) costs will be roughly 40% of the total panel cost.[6] This trend of increasing BOM costs relative to the active material costs is expected for perovskite-based solar panels as well. Therefore, to address the future cost drivers of perovskite-based solar panels, the manufacturing process for the solar panels should aim to reduce the cost of the glass and framing as much as possible. One potential method is to use a frameless panel design[7], which would eliminate the cost of the aluminum frame in exchange for corner braces**.** This could also make the panel lighter**.** The glass, however, cannot be eliminated. Instead, the cost of the glass can be reduced by co-locating the glass and solar panel production. Technical grade glass produced used for solar panels is produced at temperatures between 640-750 ^{o}C and then cooled over hundreds of meters to room temperature in a lehr.[8] This manufacturing process can produce glass with widths up to 4 m and at rates of 6,000 km/yr (15-25 m/min). One potential cost reduction pathway for perovskite-based solar panels would be a deposition method that can be

attached to a glass manufacturing line and produce uniform films up to 4 m in width at a rate of up to 25 m/min. APCVD of fluorine-doped SnO_2 ($F:SnO_2$) [7] for low-E glass already achieves these metrics. This chapter reports on a process and reactor design adaptation of SnO_2 APCVD for making perovskite relevant films MABr and $SnBr_2$.

One such method of APCVD of SnO_2 reported in the literature involved the reaction of tin(IV) tetrachloride ($SnCl_4$) and water in which the precursor channels were separated by a nitrogen gas curtain.[8] In this design, $SnCl_4$ entered the reactor and was flanked by two N_2 gas curtains that suppressed any reaction at the inlet. H_2O entered from outside slits and the reaction proceeded close to the substrate as the two gases mix.

Similar to the APCVD of SnO_2, rapid reactions may also occur when making MABr and $SnBr_2$ thin films. This was evident after attempting to deposit methylammonium iodide (MAI) using the reactor of Figure 2-17. In this deposition, MA was transported to the HI inlets and reacted to deposit MAI powder, quickly clogging the HI inlet as seen in Figure 3-1. This demonstrated the need to redesign the reactor and add a nitrogen gas curtain to separate the precursors until the reaction was desired. Accurately controlling the spatial profile of the deposition process required developing a computational fluid dynamics (CFD) and CVD model.

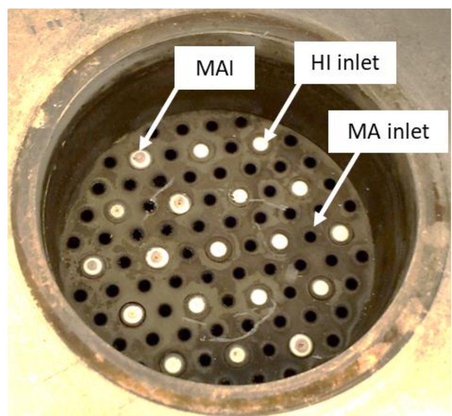

Figure 3-1: Reaction of methylamine (MA) and HI to make MAI that clogged the HI inlets. This demonstrated a need to use a nitrogen gas curtain to initially separate the precursors.

3.2 CFD Simulations

Briefly, CFD simulations involve discretizing a known geometry and simultaneously solving the conservation of energy, momentum, and mass equations at each discretized volume or element by transforming a set of partial differential equations (PDEs) into a set of algebraic equations.[9-10] There are numerous methods to perform the discretization including finite difference, finite volume, and finite element. Finite element is routinely chosen for its wide applicability to various geometries, but for simple systems, finite volume and finite difference may also be used. CFD simulations solve for 5 unknowns (velocity in 3-dimensions, pressure, temperature) using 5 equations, shown below.

Continuity Equation:

$$\frac{\partial \rho}{\partial t} + \frac{\partial \rho u}{\partial x} + \frac{\partial \rho v}{\partial y} + \frac{\partial \rho w}{\partial z} = 0 \tag{3-1}$$

X-Momentum Equation:

$$\rho\left(\frac{\partial u}{\partial t}\right)+\rho u\left(\frac{\partial u}{\partial x}\right)+\rho v\left(\frac{\partial v}{\partial y}\right)+\rho w\left(\frac{\partial w}{\partial z}\right)=\rho g_x-\frac{\partial p}{\partial x}+\frac{\partial}{\partial x}\left[2\mu\frac{\partial u}{\partial x}\right]+\frac{\partial}{\partial y}\left[\mu\left(\frac{\partial u}{\partial y}+\frac{\partial v}{\partial x}\right)\right]+\frac{\partial}{\partial z}\left[\mu\left(\frac{\partial u}{\partial y}+\frac{\partial v}{\partial x}\right)\right] \quad (3\text{-}2)$$

Y-Momentum Equation:

$$\rho\left(\frac{\partial v}{\partial t}\right)+\rho u\left(\frac{\partial v}{\partial x}\right)+\rho v\left(\frac{\partial v}{\partial y}\right)+\rho w\left(\frac{\partial v}{\partial z}\right)=\rho g_y-\frac{\partial p}{\partial y}+\frac{\partial}{\partial x}\left[\mu\left(\frac{\partial u}{\partial y}+\frac{\partial v}{\partial x}\right)\right]+\frac{\partial}{\partial y}\left[2\mu\frac{\partial v}{\partial y}\right]+\frac{\partial}{\partial z}\left[\mu\left(\frac{\partial v}{\partial z}+\frac{\partial w}{\partial y}\right)\right] \quad (3\text{-}3)$$

Z-Momentum Equation:

$$\rho\left(\frac{\partial w}{\partial t}\right)+\rho u\left(\frac{\partial w}{\partial x}\right)+\rho v\left(\frac{\partial w}{\partial y}\right)+\rho w\left(\frac{\partial w}{\partial z}\right)=\rho g_z-\frac{\partial p}{\partial z}+\frac{\partial}{\partial x}\left[\mu\left(\frac{\partial u}{\partial z}+\frac{\partial w}{\partial x}\right)\right]+\frac{\partial}{\partial y}\left[\mu\left(\frac{\partial v}{\partial z}+\frac{\partial w}{\partial y}\right)\right]+\frac{\partial}{\partial z}\left[2\mu\frac{\partial w}{\partial z}\right] \quad (3\text{-}4)$$

Energy Equation:

$$\rho C_p\frac{\partial T}{\partial t}+\rho C_p u\frac{\partial T}{\partial x}+\rho C_p v\frac{\partial T}{\partial y}+\rho C_p w\frac{\partial T}{\partial z}=\frac{\partial}{\partial x}\left[k\frac{\partial T}{\partial x}\right]+\frac{\partial}{\partial y}\left[k\frac{\partial T}{\partial y}\right]+\frac{\partial}{\partial z}\left[k\frac{\partial T}{\partial z}\right]+q_V \quad (3\text{-}5)$$

Table 3-1:

Symbol	Description
C_p	Constant pressure specific heat
g_x, g_y, g_z	Gravitational acceleration in the x, y, and z direction
k	Thermal conductivity
p	Pressure
q_V	Volumetric heat source
T	Temperature
t	Time
u	x-direction velocity
v	y-direction velocity
w	z-direction velocity
μ	dynamic viscosity
ρ	density

The momentum equations relate the momentum derivative to the expected forces in the environment – gravitational, pressure, and viscous forces. These equations are non-linear and

interdependent, which makes analytical solutions impossible except for the simplest of cases. Of special importance is the non-linear nature of these equations. Imprecision in the iterated calculations can result in error propagation, as can error diffusion through an improperly drawn mesh. Rectilinear meshes following the expected flow field help limit such error diffusion. When drawing rectilinear meshes is not possible, such as in cases around a sharp point or a curved surface, triangular or prismatic mesh geometries may be used but with smaller characteristic lengths. In general, optimization of the mesh comes from experience. Smaller mesh sizes generally produce more accurate results but may result in significantly greater computational requirements. Calculating the pressure presents another issue. If the velocities are calculated using the momentum equation, and the temperature is calculated using the energy equation, then the pressure must be calculated using the continuity equation. However, the pressure term does not explicitly appear in Equation (3-1). To address this, several techniques have been developed to modify the continuity equation whereby the pressure term appears through an explicit pressure-velocity relationship.

3.2.1 Gas Transport Models

The transport of precursors to the substrate relies on three transport phenomena typical in APCVD reactors – advection, convection, and diffusion. Advection, the dominant transport mechanism for APCVD reactors, consists of the transport of a precursor due to bulk flow of a carrier gas (such as N_2). By assuming complete saturation of the carrier gas with precursor according to its partial pressure, the flow rate of precursor may be estimated by[13]

$$\dot{V}_a = \frac{p_a}{1 - p_a}\dot{V} \tag{3-6}$$

where $\dot{V}_a$ is the flow rate of precursor a, p_a is the partial pressure of precursor a, and $\dot{V}$ is the flow rate of the carrier gas. The assumption of complete saturation is not always accurate and depends on the interface geometry of the precursor reservoir and carrier gas. As the ratio of the interfacial area to carrier gas velocity increases, the assumption of complete saturation becomes more appropriate. In the case of the traditional precursor bubbler design, the applicability of the assumption depends on bubble size and time the bubble is under the precursor liquid level. Nebulizers, machines that generate fine mists, are more likely to cause complete saturation of the carrier gas with the precursor by greatly increasing the interfacial contact area between the precursor and carrier gas.

Convection relies on a density gradient caused by either a temperature, pressure, or species gradient to drive fluid flow. Under isothermal conditions and when the partial pressure of the precursor is low, forced convection (e.g. from a pressure difference) will dominate. In this case, the density gradient inside the reactor will be negligible. A key difference between convection and advection is the former describes the motion of the fluid, whereas the latter describes the transport of a material or property in the moving fluid.

Diffusion is the spontaneous transport of a molecular species in a binary or multi-component mixture from regions of high to low concentration with zero net flux of particles. Diffusion is modeled assuming the linear relationship between the concentration gradient of a species and its rate of flux given by Fick’s First Law, reproduced below for a binary model

$$J_A^B = n\frac{\partial x_A}{\partial z} = D_{AB}\frac{\partial C_A}{\partial z} \quad (3\text{-}7)$$

$$J_B^A = n\frac{\partial x_B}{\partial z} = D_{BA}\frac{\partial C_B}{\partial z} \quad (3\text{-}8)$$

where J_A^B (J_B^A) is the rate of flux of species A in B (B in A), n is the total molar concentration, x_A (x_B) is the mole fraction of species A (B), D_{AB} (D_{BA}) is the binary diffusion coefficient of species A in B (B in A), C_A (C_B)is the spatially-dependent concentration of species A (B), and z is the characteristic dimension. Because diffusion requires, by definition, zero net flux, binary diffusion fluxes for dilute gases (10^{19} to 10^{20} per cm^{-3})[14] must be equal and opposite, that is $J_A^B = J_B^A$. Furthermore, given that $x_A + x_B = 1$, it is easily shown that the binary diffusion coefficients must be equal.

$$D_{AB} = D_{BA} \quad (3\text{-}9)$$

However, a pressure gradient within the system must concurrently exist for diffusion to occur with zero net flux. A binary system of species with unequal masses will have unequal velocities proportional to $1/\sqrt{m}$ with m being the molecular mass. As such, in the presence of a concentration gradient of species A or B or both, the lighter species will have a higher flux resulting in a non-zero net flux until a sufficient pressure gradient is developed to restore the net-zero flux condition.[14] Fortunately, the dependence of binary diffusion depends only negligibly on the pressure gradient, thus relieving calculations of the diffusion coefficient of any related complications.

Multicomponent mixtures, however, have diffusion coefficients for each species that are composition dependent. The restriction may be relaxed for a trace gas species diffusing through a multicomponent background gas where empirical evidence demonstrates the difference between the real and composition-independent diffusion coefficients is a few percent.[14] In this case, the solution of the Maxwell-Stefan multicomponent diffusion equation for the diffusion coefficient of the trace gas may be simplified to

$$\frac{1}{D_1} = \sum_{j=2}^{v} \frac{x_j}{D_{1j}} \tag{3-10}$$

which is a statement of Blanc's Law with the assumption that the ratio of the collision diameters is independent of energy.[13] Because empirical data on diffusion coefficients for all molecular species of interest is unavailable, Chapman-Enskog theory[16] allows one to approximate the binary diffusion coefficient under the assumptions of binary collisions (valid for gases with a mean free path to molecular diameter ratio on the order of 100 – N_2 at 100 °C and 1 atm has a ratio near 200), collisions are predominantly between gas molecules and not with the containment surface, the gas is only slightly perturbed from thermodynamic equilibrium (a necessary condition for the linearization of transport fluxes with gradients of the gas properties), and elastic collisions, whereby internal degrees of freedom are neglected and kinetic energy is conserved.[14] Equation (3-11) is the Chapman-Enskog equation for a binary diffusion coefficient to first order. For heavy, trace gases, the first order approximation is accurate to within 1% of the limit.

$$D_{12} = 0.008258 \left(\frac{M_1 + M_2}{2M_1 M_2}\right)^{0.5} \frac{T^{1.5}}{p\bar{\Omega}_{12}^{1,1}} \tag{3-11}$$

Here, D_{12} is the diffusion coefficient for gases 1 and 2, M is the molecular weight in grams per mole, T is the absolute temperature in Kelvin, p is the pressure in atmospheres, and $\bar{\Omega}_{12}^{1,1}$ is the collision integral in square angstroms.

The relative importance of diffusion to advection may be determined by the Péclet number, which is the ratio of the advective to diffusive transport, shown below

$$\mathrm{Pe} \equiv \frac{\text{advective transport}}{\text{diffusive transport}} = \frac{\mathrm{Lu}}{\mathrm{D}} \tag{3-12}$$

where L is the characteristic length of the system, u is the fluid speed, and D is the diffusion coefficient. The Pe number for most APCVD systems is sufficiently high to neglect diffusion for most of the precursor transport. However, through the boundary layer along the substrate, the Pe number rapidly decreases as the fluid velocity decreases, and the effect of diffusion on the deposition process becomes significant.

3.2.2 Software Packages

Simulations were performed using student licenses of two different software packages – Autodesk CFD and Ansys Fluent. Full explanations of these software can be found on their respective websites.[17,18] Autodesk CFD was chiefly used to monitor fluid flow with single particle tracking in 3D. To acquire the data from tracking multiple particles in Autodesk CFD, two identical simulations were run tracking different species between them. Complementary to Autodesk CFD,

Ansys Fluent was used for 2D fluid flow with multiple particle tracking. Ansys Fluent was also used to refine the CFD and CVD model.

Simulation of temperature changes, and therefore calculations using Equation (3-5) were neglected by assuming very little increase in the heat content of the gas streams because of the entropy of mixing and heat of reaction. Given the gases contain around 0.1% by mole of reactants, it was assumed that the heat released from the reaction did little to affect the overall temperature of the gas stream. Because the Mach number (ratio of the speed of the gas to the speed of sound) for the gas was less than 1 for the entire domain of the simulation, incompressible flow was assumed. Additionally, because of the relatively low Reynolds numbers (ratio of inertial to viscous forces) expected in the reactor, the exact turbulence model used was assumed not important and a simple $k - \epsilon$ model was used.

The boundary conditions used in the simulations to fully constrain the system were determined by the set of tunable variables – temperature, volumetric flow rate, pressure, and precursor concentrations. By defining volumetric flow rates into the reactor and the outlet pressure (0 psig), the flow and pressure throughout the internal body of the reactor could be simulated. While it was not necessary to solve the energy equation, the temperature still affected such parameters as the diffusion coefficient, which could strongly affect the deposition. With a given reactor design, material selection, boundary conditions, and mesh applied, simulations were performed. Due to the high computational resource requirements, the simulations were performed on both Google's and Amazon's cloud computing services in addition to a local desktop (Intel i7-10700 4.5 GHz × 8 cores 64 GB RAM).

3.3 Reactor Design

a

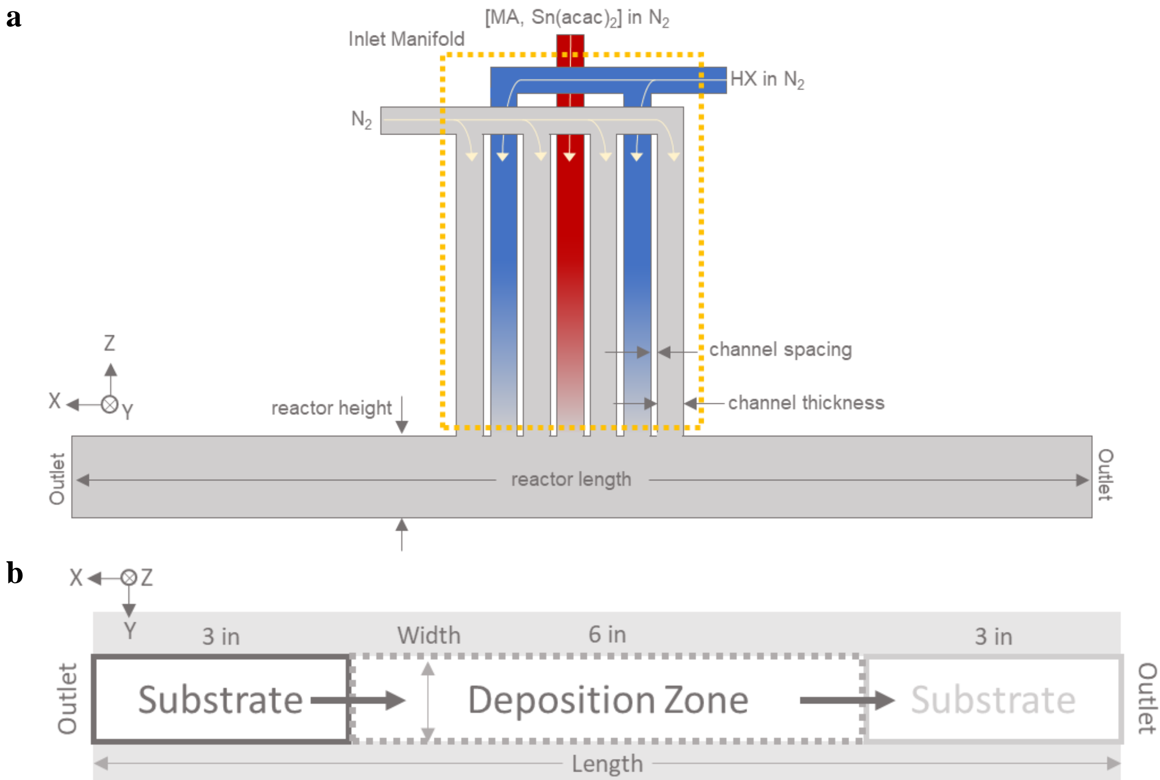

Figure 3-2: (a) Reactor illustration (b) Tope view of the reactor designed to hold a 3 in. substrate at least 3 in. away from the center of the deposition zone (6 in total). This amounted to a reactor length of 12 in.

The reactor design was inspired by one from the literature[8] and was developed into the one illustrated in Figure 3-2a. The reactor consisted of wide, thin inlet manifold channels to homogenize the gas velocity across the width of the sample deposition zone and two, symmetric outlet channels. The thickness of the inlet manifold channels was set to 1 mm, as had been previously done.[8] This was deemed thin enough to efficiently homogenize the gas flow but not too thin to introduce non-uniformity during fabrication. The reactor height was chosen to minimize turbulence in the deposition zone without dramatically increasing the demands on the manufacturing tolerance and resulted in approximately 3 mm (~1/8 in.). The total length of the

reactor was chosen as the minimum length required to achieve steady state of the flow prior to exiting and to hold a 3 in. long substrate at least 3 in. away from the center of the deposition zone in either direction (see Figure 3-2b). This amounted to a total of 12 in. This allowed a substrate to remain inside the cavity of the reactor with reduced surface exposure to ambient H_2O and O_2 in case multiple passes through the deposition zone were required. This design also afforded a purge of the gas lines during the warmup of the deposition process without substantially contributing to film growth while the substrate was outside the deposition zone. This later benefit was sacrificed during static depositions (no substrate translation) when the substrate was inside the deposition zone for the duration of the experiment. The potential drawbacks of this were minimized by decreasing the time to steady state delivery of the precursors (< 10 sec).

The inlet manifold channel length was chosen to homogenize the gas flow along the width of the channel prior to entering the deposition zone. Because the gas entered the reactor inlet manifold from tubing with a circular flow profile and needed to enter the deposition zone with a rectilinear flow profile, the length of the inlet manifold channels needed to accommodate this transformation. The length required was dependent on the inlet manifold design and was determined by simulation (*vide infra*).

The design of the inlet manifold required splitting 3 inlets into either 5 or 7 outlets, depending on whether additional N_2 curtains were used (see Figure 3-2a). The intent of the second set of nitrogen curtains was to further compress gas-phase reactions closer to the surface of the substrate and away from the reactor ceiling. In the second-generation inlet manifold, the extra N_2 curtains were removed to reduce the manufacturing and operating complexity.

The design of the reactor channel width was 1 in. (25.4 mm) in the first-generation reactor and 1.75 in. (44.5 mm) in the second-generation reactor. The 1 in. width was better suited for post

deposition analysis on various instruments (e.g. XPS, SEM) and was compatible with commercially available substrates, but the reactor walls affected the deposition center less with the wider channel.

The desired inlet manifold channel spacing was as thin as possible to minimize turbulence generated by the abrupt change in the flow channel. For the first-generation (Gen 1) inlet manifold, the spacing was modeled as 0.01 in. (0.25 mm). However, because the second-generation (Gen 2) manifold was manufactured by direct metal laser sintering (DMLS), the spacing was chosen to be 1 mm (0.04 in.) to provide sufficient support against collapse during the post-fabrication anneal.

Table 3-2:	Gen 1	Gen 2
Inlet manifold channel length	5.13 in	~2.35 in
Inlet manifold channel separation	0.25 mm	1 mm
Inlet manifold channel thickness	1 mm	1 mm
Reactor height	3.2 mm	3 mm
Reactor length	12 in	12 in
Reactor width	25.4 mm	44.5 mm
Number of N_2 curtains	4	2

3.4 Simulation Results

3.4.1 Gen 1 Reactor

A computer-aided design (CAD) model (Autodesk Inventor) of the Gen 1 reactor is shown in Figure 3-3 and Figure 3-4. This model was used to simulate the flow of gases using both Autodesk CFD and Ansys Fluent. The input parameters for the simulations are shown in Table 3-3.

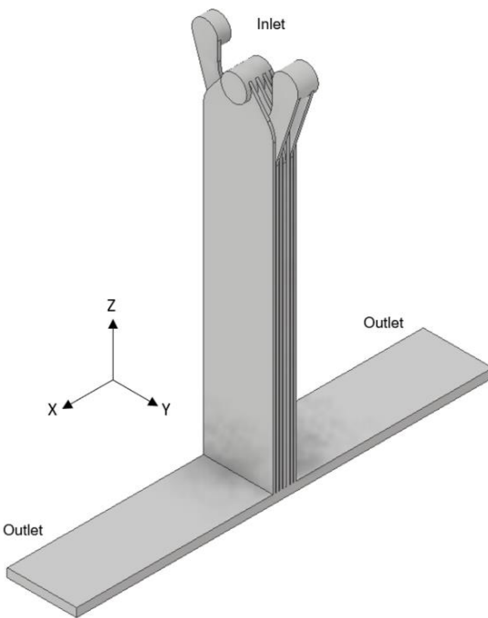

Figure 3-3: Complete diagram of the internal gas volume. The solid grey volume represents the space available to gases.

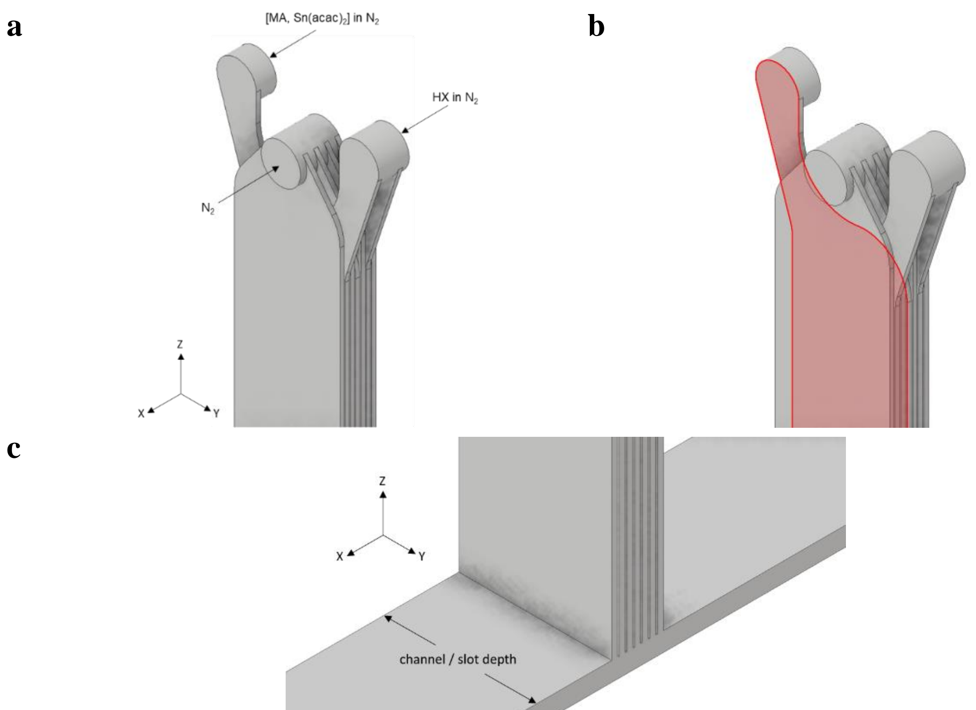

Figure 3-4: CAD models of the wetted reactor volume. The grey volume is the negative space inside the reactor for gas flow. (a) Path of inlet gases into the inlet manifold. (b) Highlighted path of the MA and $Sn(acac)_2$ channel, demonstrating the flow path of gases through the channels. (c) Isometric view of the inlet to the deposition zone

Table 3-3: Simulation input parameters	
Temperature (°C)	120
N_2 curtain flow rate per channel (sccm)	250
0.1% HX in N_2 flow rate per channel (sccm)	250
0.1% MA and Sn Acac flow rate (sccm)	250
Outlet pressure (psig)	0

The results of the simulations in Figure 3-5 and Figure 3-6 indicate that the reactor model is sufficient to uniformly deliver the precursors to the deposition zone.

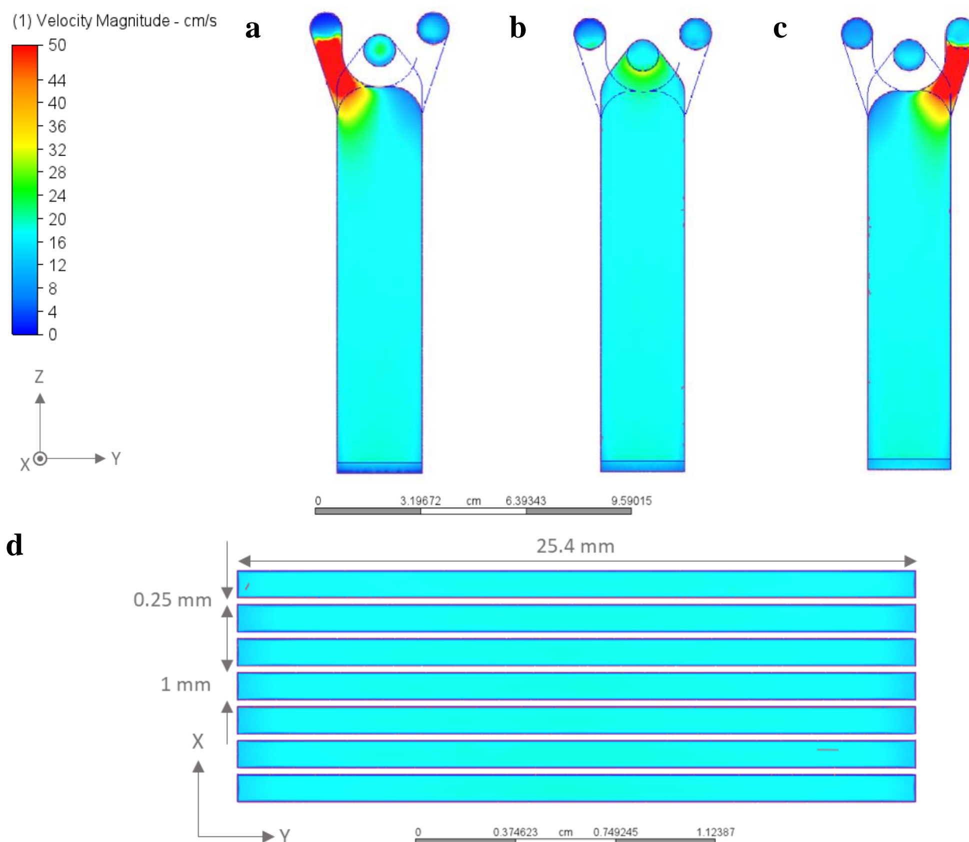

Figure 3-5: Velocity colormaps of the gas flow through the inlet manifold channels. (a) The gas flow through the MA and $Sn(acac)_2$ channel, (b) the gas flow through one N_2 curtain channel, and (c) the gas flow through the HX channel. The flow rate distribution in the $\hat{y}$-direction became uniform halfway down the channel. (d) Magnitude of the gas velocities in the 7 inlet manifold channels in a section parallel to the reactor channel. The velocity distribution was very uniform. The section is at the interface between the inlet manifold and the deposition zone, marked by the line at the bottom of the channels in (a)-(c).

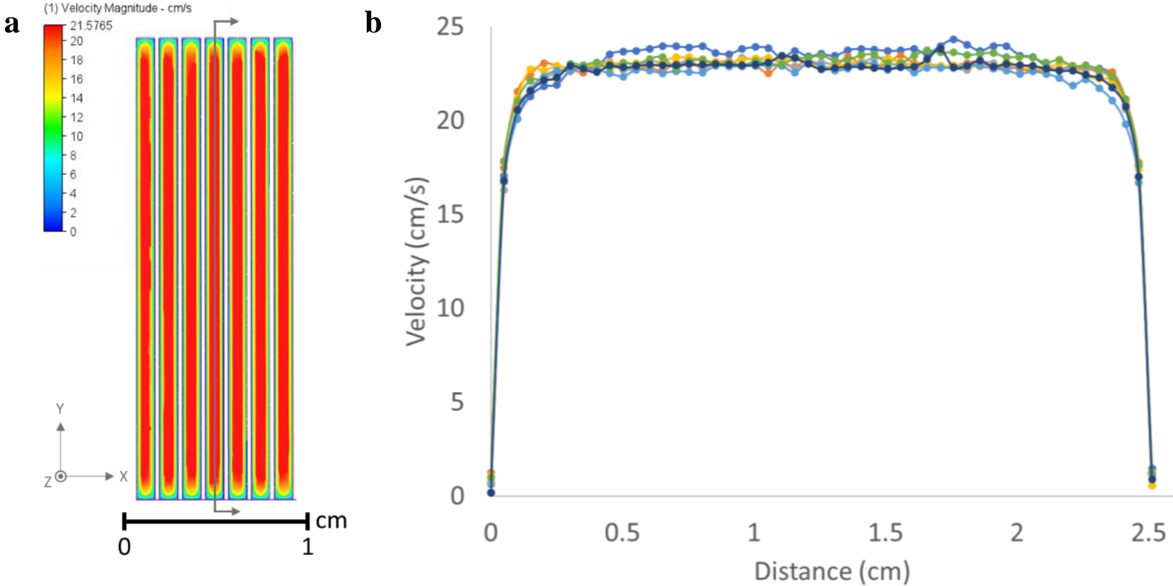

Figure 3-6: a) The velocity profile across the 7 inlet manifold channels 0.125 in above the deposition zone. Note the increase in average velocity compared to the distribution in Figure 3-5. b) The center of the inlet manifold channels is highly uniform across all the channels in the $\hat{y}$ direction.

To initially estimate the spatial dependency of the gas phase reactions, a map of the precursor concentration product was made. Figure 3-7a shows this concentration product and that the design prevents premature mixing which would have led to deposition on the inlet manifold channels and eventual clogging as seen in Figure 3-1.

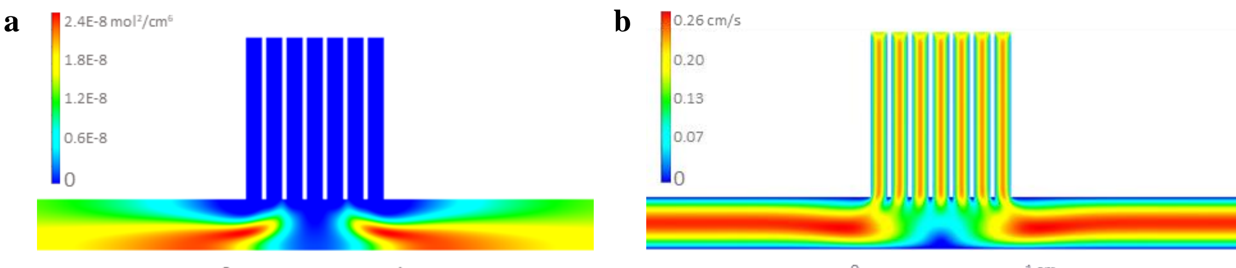

Figure 3-7: (a) The product of the concentrations of HI and MA for flow rates of 250 sccm per channel and estimated diffusion coefficients of 0.22 and 0.28 cm^2/s, respectively. This showed that the area immediately near the inlet was unlikely to achieve a high reaction rate as desired. (b) The velocity profile shows a stagnation point in the center consistent with no deposition.

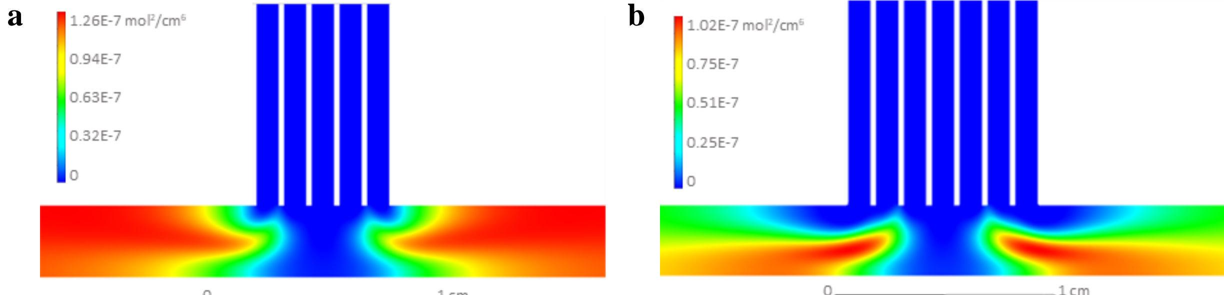

Figure 3-8: The extra flanking N_2 curtains (b) act to suppress the product of the concentrations of HI and MA over the design with only 2 N_2 curtains (a). The legend shows the product of the concentrations of HI and MA. The input conditions were 250 sccm for each channel with 0.1% MA and 0.15% HI in N_2. The results for HI were expected to carry over to HBr given that they are very similar and have a similar diffusion coefficient.

Figure 3-8 depicts the effect of having 4 vs 2 N_2 curtains is to reduce the reaction rate on the ceiling of the reactor and compressed the region of highest reactivity (assuming isothermal conditions) closer to the substrate. In real deposition experiments, consumption of the precursors would alter these plots as one moves away from the deposition zone center.

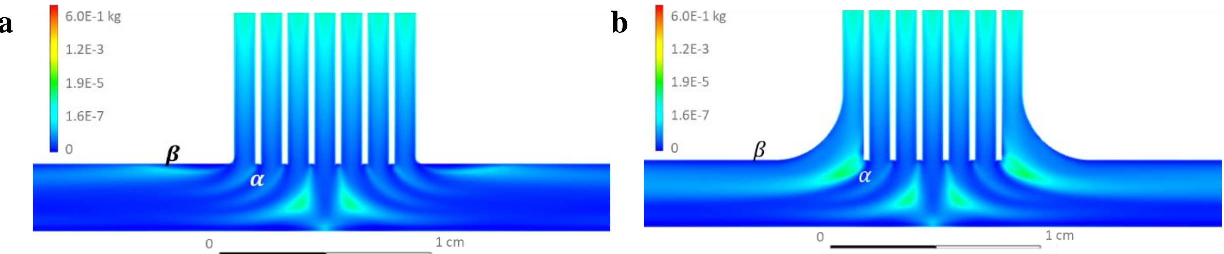

Figure 3-9: The turbulent kinetic energy (TKE) normalized by the velocity magnitude squared shows areas of high shear leading to turbulence. While the abrupt channel entrance to the deposition zone in (a) generated more shear at point β than in (b), much more shear was generated at point α in (b) than in (a). This, perhaps counterintuitively, suggested using an abrupt entrance is better than one with fillets for parallel channels.

The inlet design to the deposition zone should seek to minimize turbulence to avoid premature mixing leading to particle formation in the gas phase. When using parallel inlet manifold channels, an abrupt connection between the inlet manifold and the deposition zone was preferred

to using fillets at the edges. This avoided areas of high shear stress (assuming constant viscosity) depicted at point α in Figure 3-9b. The relation of shear stress to the generation of turbulent kinetic energy (G_k, TKE) is[10]

$$\mu G_k = -\rho \overline{u_i' u_j'} \tau_{ij} \tag{3-13}$$

where μ is the dynamic viscosity, ρ is the density, u_j' is the difference between the instantaneous and average velocity in the ĵ direction, and τ_{ij} is the shear stress. For low flow rates, the difference between the designs is likely unnoticeable. However, for higher inlet velocities, this could become significant as TKE is $\propto u^2$.

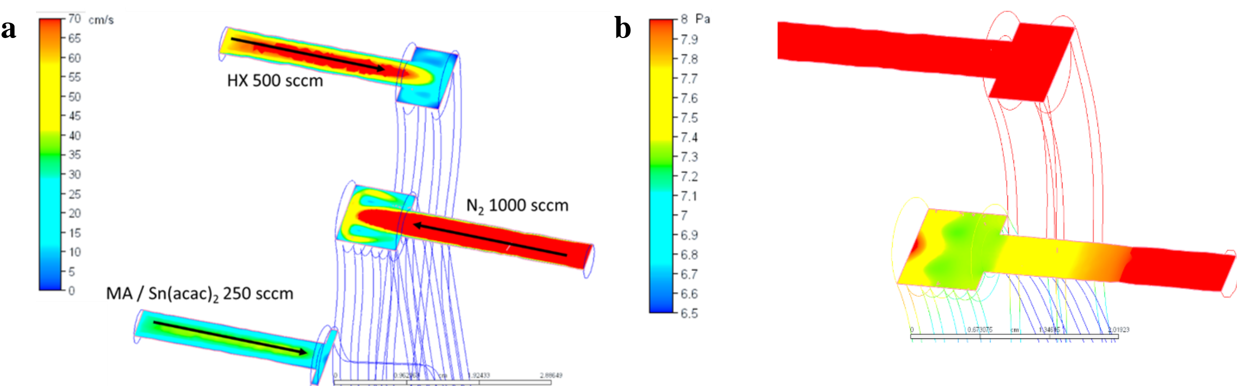

Figure 3-10: The distribution of gas into each inlet manifold channel depended on the dynamic effects of the gas velocity coming from the tubing. (a) As seen in the N_2 inlet (middle), the gas impinged on the rear wall and caused an increase in pressure (b) at this wall, which ultimately led to greater flow down the channel furthest away from the inlet. Effects of the gas dynamics on the distribution down the channels can be alleviated by having symmetric inlets to the inlet manifold and thinner channels (within manufacturing tolerance).

The inlet design to the manifold also needed careful consideration. The dynamic effect of the gas exiting the tubing and entering the inlet manifold could cause a pressure buildup (Figure

3-10a-b) that would lead to an uneven distribution of the flow through the channels. This effect is more pronounced for higher flow rates and greater division of the inlet stream into multiple channels. This deviation from even flow distribution could be reduced by having a larger inlet barrel and symmetric inputs (flow from both sides of the inlet manifold).

3.4.2 Gen 2 Reactor

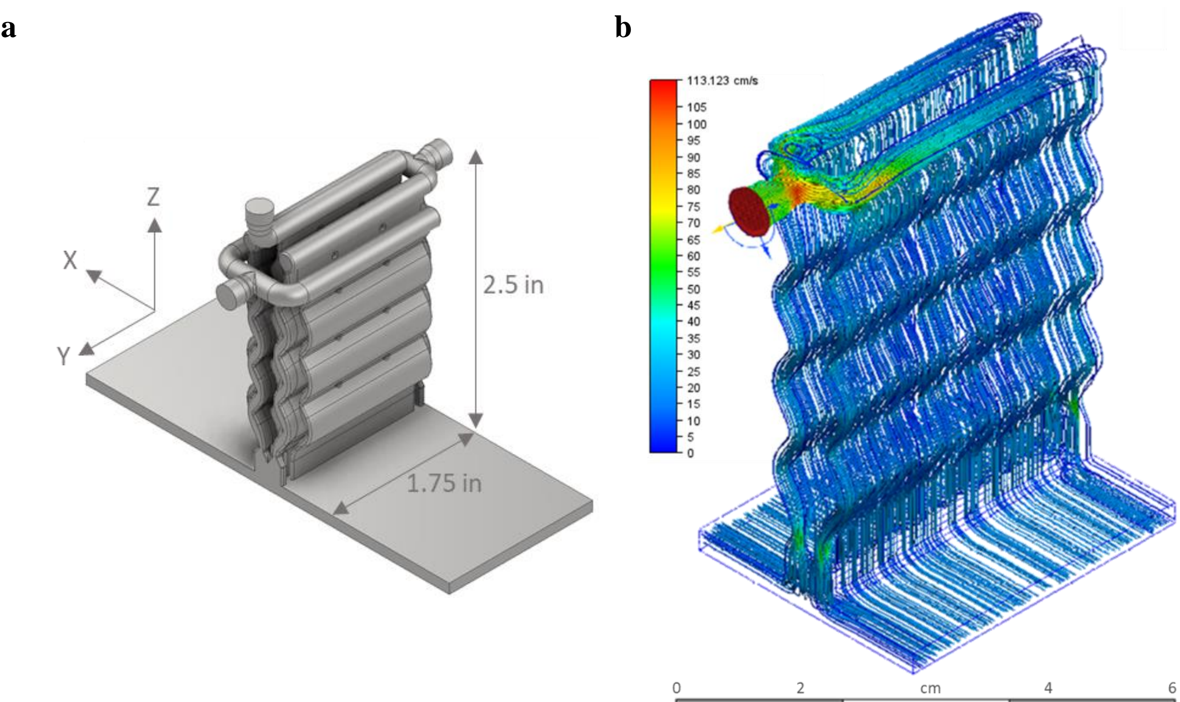

Figure 3-11: (a) The model of the Gen 2 inlet manifold was distinct from its predecessor in 3 key ways – the channels form baffles to more efficiently distribute the gas; a N_2 curtain was added along the outside wall to prevent deposition on the wall near the inlet manifold; the distribution of the gas into the manifold from the tubing is more even. (b) The traces show the path of idealized gas particles passing through the N_2 channels.

The purpose of the Gen 2 reactor was to improve upon the symmetry and reproducibility of the depositions resulting from the Gen 1 reactor. Specifically, this meant using a N_2 curtain along the wall in the immediate vicinity of the inlet manifold channels, increasing the width of the

deposition zone from 1 in. to 1.75 in. to avoid wall effects, and changing the gas inlet design to the manifold to ensure an even distribution into the channels. After iterating through several designs and optimizing the geometry, the model in Figure 3-11a was chosen (note: the length of the reactor channel is cut short for the sake of the image). The overall height of the inlet manifold was less than half that of Gen 1 because the baffle-like form of the channels greatly aiding in gas distribution, thus reducing the need of a long channel.

To add a N_2 curtain to the walls without adding an additional N_2 input line to the inlet manifold, a second splitting of the N_2 inlet manifold channels was designed (see Figure 3-12). This design enabled 1 MFC to control the delivery of N_2 to 4 channels. The N_2 distribution among the 4 channels was determined by the geometry. Notably, the second splitting (Figure 3-12c) of the N_2 curtains required numerous design iterations to achieve the desired N_2 distribution.

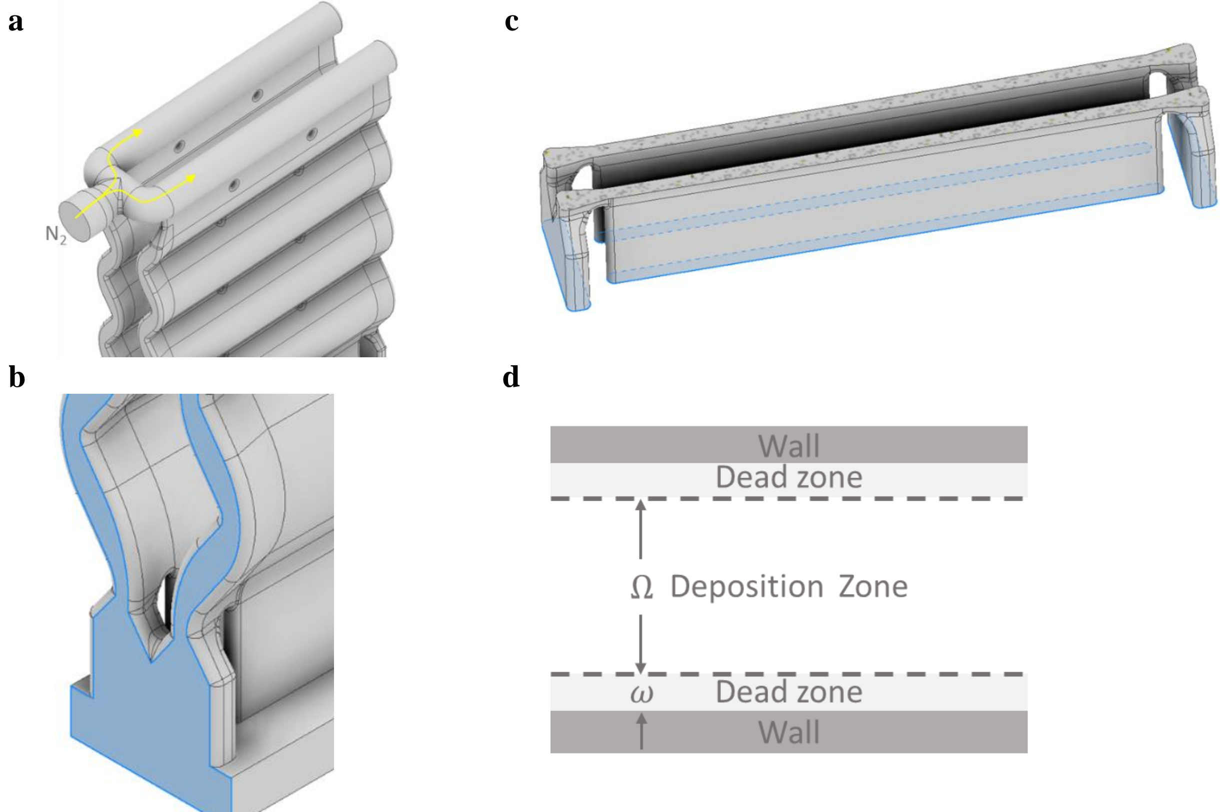

Figure 3-12: The Gen 2 inlet manifold design implemented a N_2 curtain along the wall of the deposition zone in the vicinity of the inlet manifold channels to prevent severe buildup of material along the wall. To accomplish this, (a) the N_2 input line was first split into two channels. (b) Then, at roughly 5-10 mm above the deposition zone, the N_2 channels split near the edges and recombined with those of the opposite channel. (c) This resulted in 4 N_2 curtain inlets (highlighted in blue) connected to the deposition zone using 1 MFC. The specific shape of the N_2 curtain channel ends prior to the second split was iteratively designed so that the two wall N_2 curtains delivered $\approx 17\%$ of the volume flow of the other two channels – a number equal to the ratio of the dead zone to deposition zone widths ($2\omega/\Omega$). This would minimize strong advective currents towards or away from the side walls.

As was done for the first reactor, the gas flow was simulated to ensure the design minimized the error in uniformity of flow through the inlet manifold channels and the reactor channel. Because the reactor height and flow velocities were nearly identical to the previous design and the channel separation only increased to 1 mm from 0.25 mm, it was expected that the reaction rates would also be sufficiently low or 0 near the inlet manifold channels to avoid clogging as in the previous design.

Table 3-4: Simulation input parameters

Parameter	Value
Temperature (°C)	120
N_2 curtain flow rate (sccm)	1062
0.1% HX in N_2 flow rate (sccm)	750
0.1% [MA, $Sn(acac)_2$] flow rate (sccm)	375
Outlet pressure (psig)	0

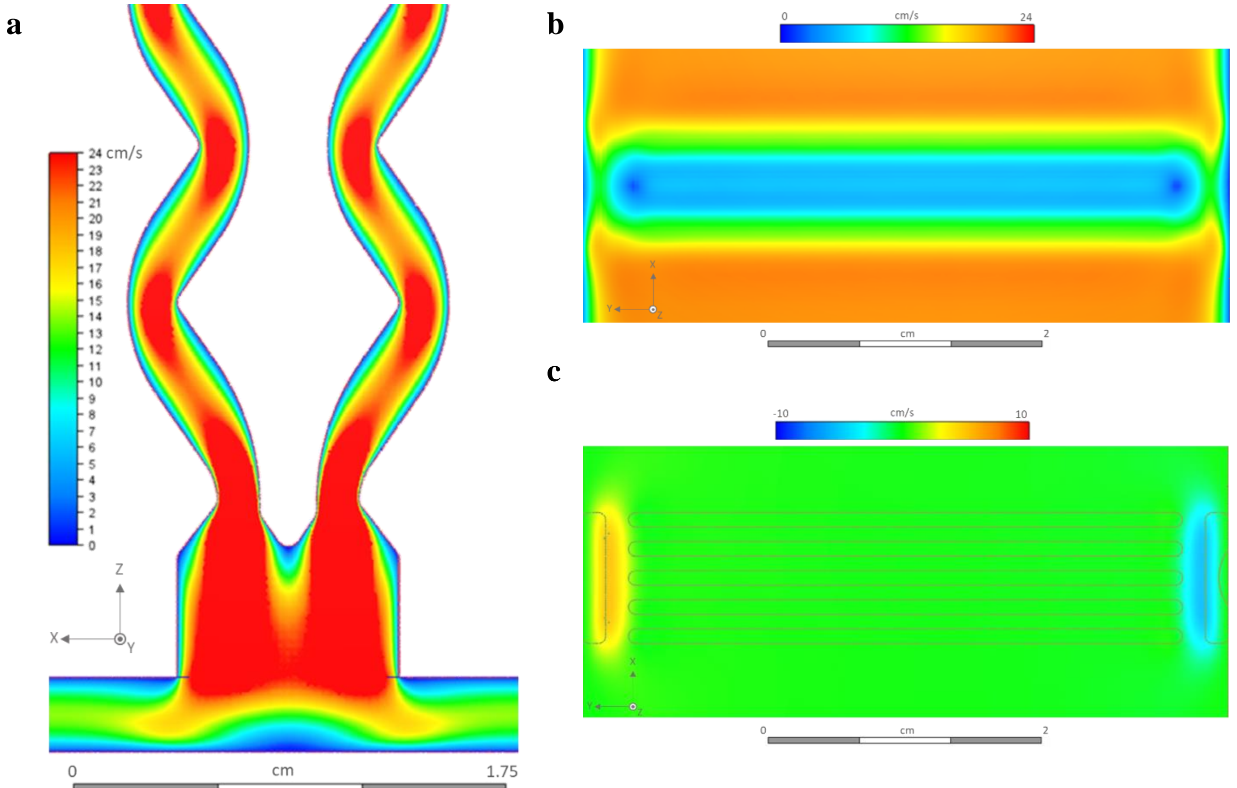

Figure 3-13: (a) The N_2 curtain along the wall, as seen in Figure 3-12, exhibited the desired symmetric flow. (b) A top view of the gas velocity in the center plane of the reactor channel shows a symmetric velocity distribution in the $\hat{x}$-direction and a uniform velocity distribution in the $\hat{y}$-direction around the deposition zone. (c) In the same plane, the $\vec{v}_y$ magnitude distribution shows the N_2 curtain along the wall prevented advection of precursors and products towards the wall near the channel inlet to the deposition zone.

Figure 3-13c shows the design of the N_2 curtain channel provided sufficient N_2 flow to prevent advection of the precursor gas streams towards the side walls in the vicinity of the inlet manifold. This was important to prevent repeated deposition near the inlets, which, over time, would lead to changes in the flow pattern. Figure 3-13b shows that the splitting of the N_2 inlet (see

Figure 3-12a) to the N_2 curtains along the side walls does not lead to a velocity gradient along the $\hat{y}$-direction in the reactor channel.

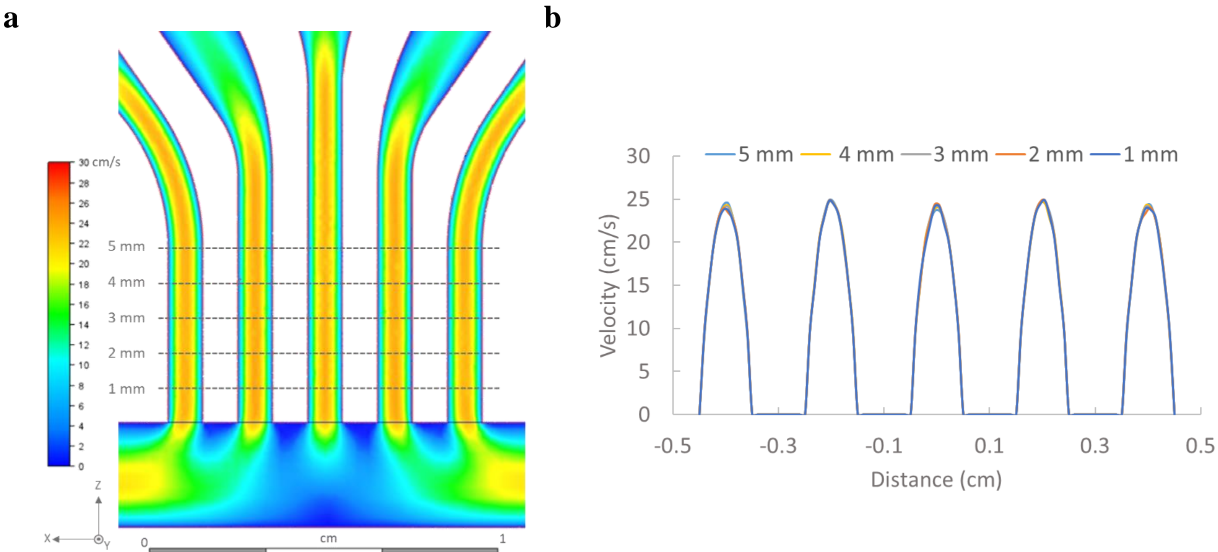

Figure 3-14: (a) The flow through the reactor channel was symmetric and increased further away from the center where there exists a stagnation point. (b) The velocity profiles across center of the channels in (a) were nearly identical and fully developed. The flow through the N_2 curtain channels was slightly greater than in the precursor channels, but this did not affect modeling or film deposition.

Figure 3-14 shows the center profile of the flow through inlet manifold channels near the entrance to the deposition zone. The flow in each channel approximated a parabola, consistent with fully developed plane Poiseuille flow. The slight deviation from a parabola is due to the discretization of the channels in the simulation. The negligible differences between the flow profiles for 1-5 mm above the deposition zone further indicated that the flow into the reactor was fully developed. This was critical for justifying the inlet conditions of the 2D CVD simulations using a reduced reactor geometry in Chapter 5.

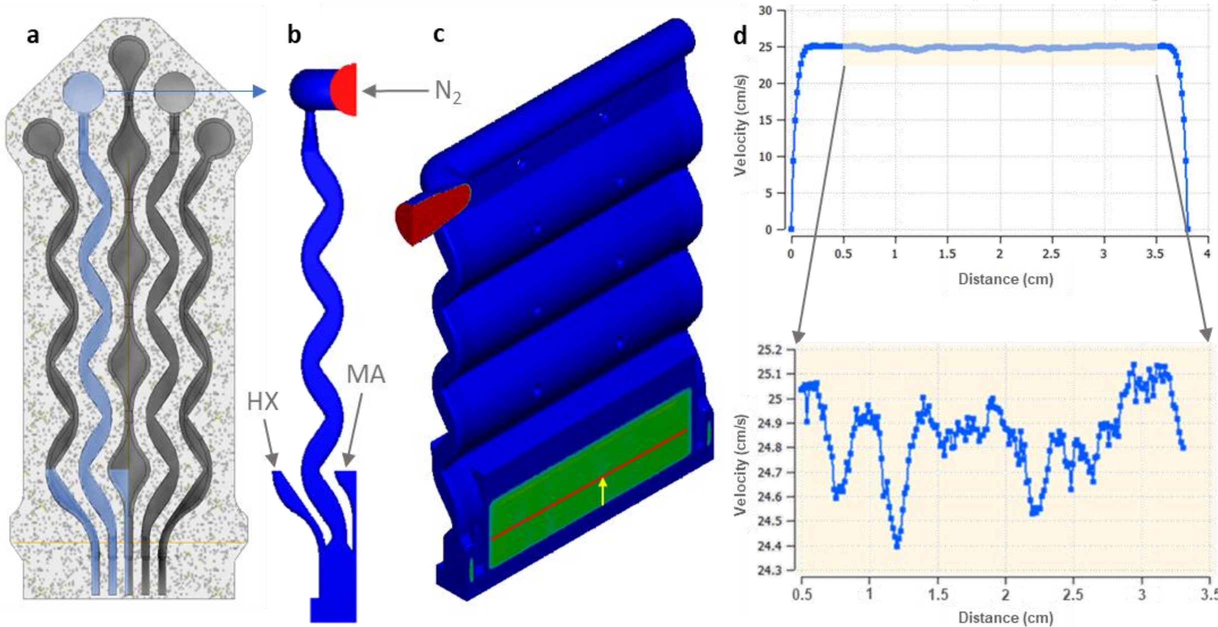

Figure 3-15: (a) The half-section view of the inlet manifold shows the baffle-like channels. The blue region was simulated to measure the uniformity of the gas flowing across the N_2 channel in the deposition zone. A significant reduction in CPU and memory requirements was obtained by not including the rest of the reactor geometry in the simulation. (b) The side profile of the simulation shows the entrance of N_2 into the inlet manifold as red (indicating a high flow rate) and blue along the walls (indicating zero flow). (c) An isometric view of (b) shows the channel near the deposition zone. The green color shows the uniformity of the flow velocity, and (d) shows a slice of the channel (red line in (c)) to highlight the magnitude. The lower velocity plot highlights the velocity variability and uncertainty in the simulation.

To better understand the flow distribution across the channels, the flow into three channels representative of the different gas streams – HX, [MA, $Sn(acac)_2$], N_2 curtain – was simulated. To increase the resolution across the channel width, the reactor geometry was reduced using symmetry planes and assuming uniform flow in the channels *not* under study. Figure 3-15a-c shows the setup for the simulation in the case of the N_2 curtain, where only half of the N_2 curtain geometry was simulated and the geometry for the other channels was drastically truncated to that necessary to achieve a fully developed flow at the inlet to the deposition zone. The flow rates of Table 3-4 were halved to accommodate this geometry reduction. This procedure helped increase the mesh count in the flow regions of interest while maintaining the memory requirement below the maximum

available (64 GB). Figure 3-15d shows the outcome of a single plot of velocity across the N_2 channel at a specific height above the deposition zone. The enlarged area shows the velocity variability.

Figure 3-16 depicts the flow velocity average and variability across each channel in the deposition zone. The 5 plots for each figure represent a velocity profile at a distance above the entrance to the deposition zone (see the yellow arrow in Figure 3-15c) and show the flow was fully developed inside the channel prior to entering the deposition zone. The right side of each figure demonstrates a noticeable deviation from the trend, especially in the case of Figure 3-16c. This could not be explained on any physical grounds. Given the expected total flow rate through each channel was 375 sccm, plane Poiseuille flow (flow between two narrowly separated planes) predicts an average velocity of 24.6 cm/s. However, the actual velocity may be slightly higher due to edge effects (see Figure 3-15d). This suggested the average velocity for the HX and [MA, $Sn(acac)_2$] channels are consistent with expectations. The flow through the N_2 curtain channels is slightly higher but still within 4% of the velocity of the other channels.

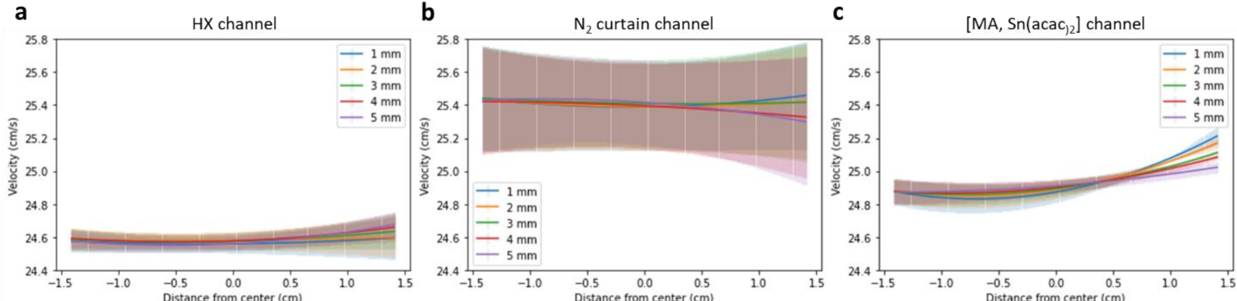

Figure 3-16: Plots (a)-(c) show 2nd order polynomial fits and the uncertainty (shading) to the velocity profiles across approximately 3 cm of each respective channel center, as was shown in Figure 3-15d. The legend indicates how far up from the base of the inlet manifold the data was recorded (see yellow arrow and red line in Figure 3-15c). The results of this study indicated that the uncertainty in the N_2 channel was much greater than in either the hydrogen halide (HX) channel or the [MA, $Sn(acac)_2$] channel. However, in all cases the uncertainty was less than 5% of the flow. The [MA, $Sn(acac)_2$] channel in (c) showed an unphysical uptick in velocity due to an unknown error, however the average velocity is consistent with expectations.

3.5 Reactor Fabrication

3.5.1 Gen 1 Reactor Fabrication

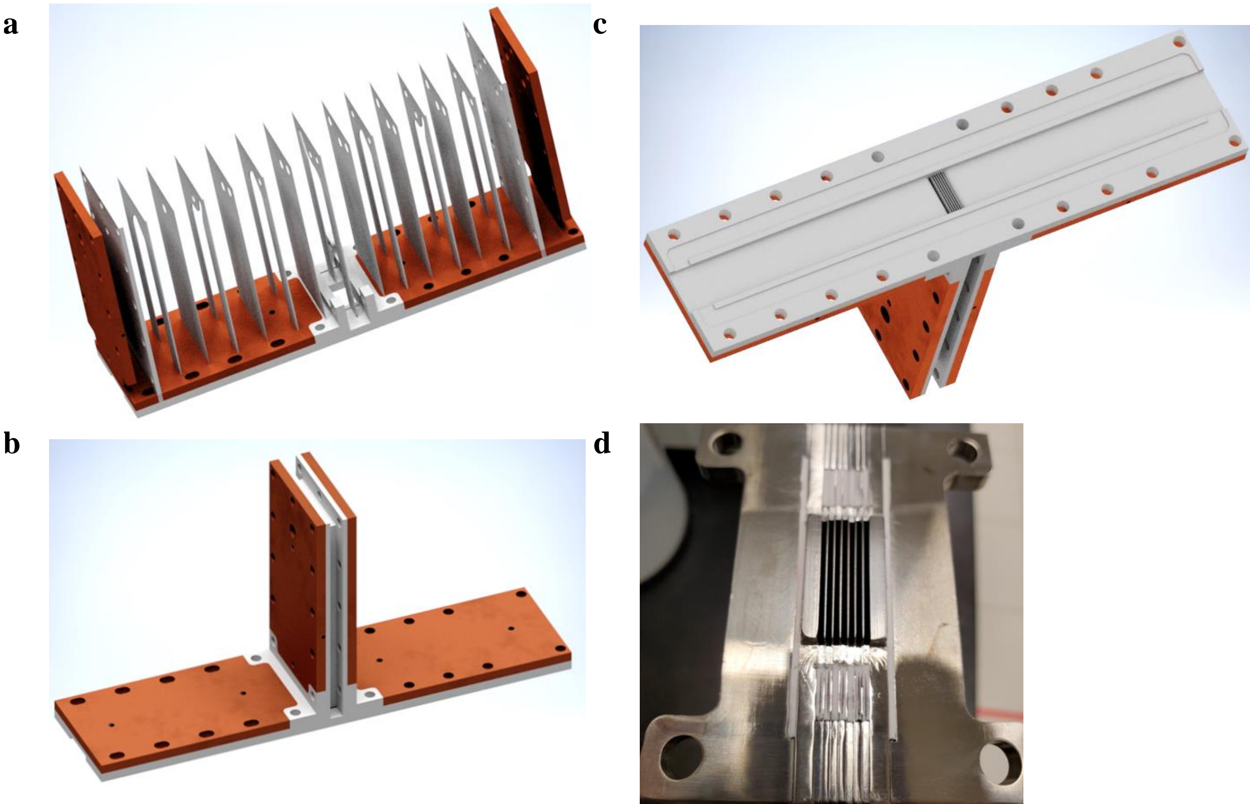

Figure 3-17: (a) An exploded view of the inlet manifold assembly shows how alternating plates and gaskets were used to define channels for gas flow. The channels in the manifold were connected by concentric holes in the plates and gaskets that form a "barrel" with the channels perpendicular to the barrel axis. The outside plates were 1/8 in. thick to sustain the compressive force in the interior. (b) the compressed assembly was roughly ½ in. thick. The two flanking brackets attached the inlet manifold to the top plate of the reactor with a gasket in between. (c) The inlet manifold recessed into the reactor top plate so that the base of the channel plates was flush with the reactor top plate. (d) The assembled inlet manifold prior to attachment to the reactor.

After several design iterations, the Gen 1 inlet manifold was constructed from a series of spacers and gaskets, idealized in Figure 3-17. During assembly, the gaskets were crushed to create an air-tight seal around the channel. To define these channel thicknesses, a spacer of known thickness (1 mm) was used on either side of the gasket. The channel spacings were defined by the

thickness of a second set of spacers (0.25 mm). The entire apparatus was compressed by bolts (<78 in-lbs torque with 316 stainless steel bolts) around the outside until metal-to-metal contact through all the spacers was achieved. The compression of the gasket was approximately 30%. To attach the inlet manifold to the reactor channel, two brackets were bolted on either side of the inlet manifold assembly and the reactor channel. A small, rectangular pocket in the top plate of the reactor channel allowed the extension of the inlet manifold channels into the reactor channel's top plate. Figure 3-17d shows the inlet manifold assembled with the gaskets (white areas) and the brackets. The base of the reactor was bolted to the reactor top plate (Figure 3-17c) to form a cavity 1 in. wide × 3.8 mm high. Figure 3-18 together with Table 3-5 shows a cross-sectional view of the inlet manifold and how a single channel is defined.

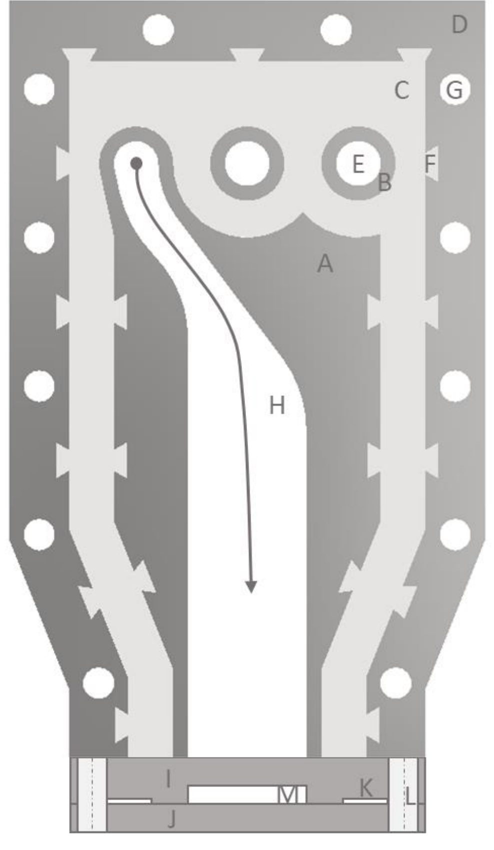

Figure 3-18: Section view of the inlet manifold and reactor channel.

Table 3-5:

	Material	Purpose
A	1 mm 316L SS	Define the flow path
B	1 mm 316L SS	Form a barrel for connecting multiple channels
C	1.5 mm ePTFE	Gasket to prevent gas exchange with the ambient
D	1 mm 316L SS	Outside gasket retaining plate
E	-	Manifold to transfer inlet gas from tubing to multiple channels
F	-	Dovetail to prevent gasket and plates from shifting during assembly
G	-	Bolt holes to compress gasket and form a metal-to-metal contact
H	-	Flow path for gases
I	0.375 in 316L SS	Top reactor plate
J	0.25 in 316L SS	Bottom reactor plate
K	1.5 mm ePTFE	Gasket to prevent gas exchange with the ambient
L	-	Bolt holes to connect the top and bottom reactor plates
M	-	Deposition zone channel

The materials used in the construction were 316L stainless steel for the wetted parts, ePTFE for the gaskets, and copper for the heat transfer plates (shown in red/orange in Figure 3-17a-c). 316L stainless steel was chosen for its acid resistance; ePTFE was chosen for its high temperature limit (~ 270 °C), elasticity, and resistance to creep;[19] copper for the heat transfer plates was chosen for its high thermal conductivity.

A CO_2 laser cutter (Kern) was used to fabricate the stainless steel plates and ePTFE gaskets for the inlet manifold. The reactor top and bottom plates as well as the copper heat transfer plates were machined on a mill by Harvard University's in-house machine shop. Swagelok VCR glands were silver soldered to the inlet manifold to connect with the inlet tubing.

3.5.2 Gen 2 Reactor Fabrication

The Gen 2 reactor fabrication for the inlet manifold was outsourced to Protolabs[20] for direct metal laser sintering (DMLS). The decision to 3D print this part was made for several reasons. It accommodated a more intricate design of the inlet channels than could ever be made by assembly, ensured that no gas exchange with the ambient occurred, and increased the temperature rating of the reactor by eliminating the use of gaskets. The body was made from 316L stainless steel.

Because the precision of the DMLS process is not as good as a mill (0.3 mm *vs* 0.03 mm), the as-printed inlet manifold was milled to better shape the channels near the connection to the reactor channel. A design for the reactor channel top and bottom plates similar to the Gen 1 reactor was used with the Gen 2 inlet manifold. The reactor plates were milled in-house using the student machine shop from 316L stainless steel. The inlet manifold was welded to the top plate by Harvard's in-house machine shop. Swagelok VCR glands were silver soldered onto the inlet manifold to connect to the inlet tubing. Images of the finished inlet manifold body and base connected through the reactor top plate are shown in Figure 3-19.

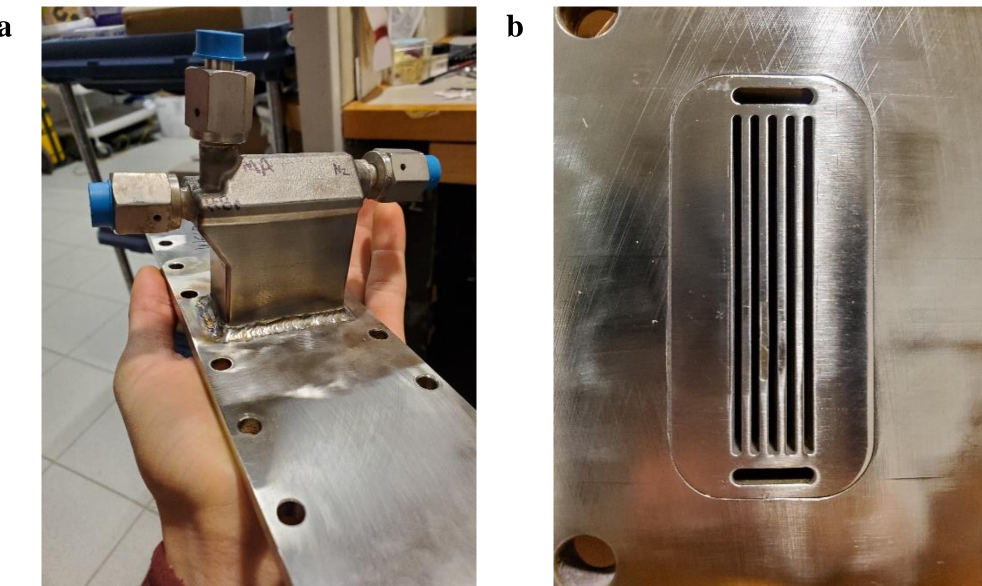

Figure 3-19: (a) Image of the 2nd generation inlet manifold. (b) Image of the base of the inlet manifold after attachment to the reactor top plate.

3.6 Conclusion

This chapter discussed the design, modeling, and construction of two similar lab-scale APCVD reactors. Simulations using Autodesk CFD and Ansys Fluent were used to predict gas flow in the different gas injector inlet manifold designs to ensure no mixing of the reactant gases occurred on the inlet. The Gen 2 design improved upon the Gen 1 model by eliminating deposition on the walls of the reactor near the deposition zone, increased the width of the deposition to mitigate wall effects, and more evenly homogenized the flow of gases through the inlet manifold. The reactors were constructed in Harvard's student machine shop and at Protolabs.

3.7 References

1. Pham, P. Atmospheric Pressure Chemical Vapor Deposition of Graphene. in *Chemical Vapor Deposition for Nanotechnology* (ed. Mandracci, P.) (IntechOpen, 2019)

2. Gordon, R. G., Barry, S., Barton, J. T. & Broomhall-Dillard, R. N. R. Atmospheric pressure chemical vapor deposition of electrochromic tungsten oxide films. *Thin Solid Films* **392**, 231–235 (2001).

3. Woods, L. & Meyers, P., *Atmospheric Pressure Chemical Vapor Deposition and Jet Vapor Deposition of CdTe for High Efficiency Thin Film PV Devices: Final Technical Report*. National Renewable Energy Laboratory (2002).

4. Sedgwick, T. and Agnello, P. Atmospheric pressure chemical vapor deposition of Si and SiGe at low temperatures. *J. Vac. Sci. Tech. A*, **10**, 1913 (1992).

5. Berry, N. et al. Atmospheric-Pressure Chemical Vapor Deposition of Iron Pyrite Thin Films. *Adv. Energy Mater.* **2**. 1124–1135 (2012).

6. Woodhouse, M. A., Smith, B., Ramdas, A., and Margolis, R. M. *Crystalline Silicon Photovoltaic Module Manufacturing Costs and Sustainable Pricing: 1H 2018 Benchmark and Cost Reduction Road Map*. National Renewable Energy Laboratory (2019).

7. Verband Deutscher Maschinen und Anlagenbau, International Technology Roadmap for Photovoltaics, Tenth Edition, website: https://itrpv.vdma.org/# (2019).

8. Strobl, K., Monville, M., Singhal, R., Wright, S., and Rosenbaum, L. Low-Cost, High-Volume Scale-Up of CVD Films and Nano-Structured Materials for Industrial Applications. *2014 NSTI Nanotechnology Conference and Expo* (Washington, D.C. 2014)

9. Proscia, J. & Gordon, R. G. Properties of fluorine-doped tin oxide films produced by atmospheric pressure chemical vapor deposition from tetramethyltin, bromotrifluoromethane and oxygen. *Thin Solid Films* **214**, 175–187 (1992).

10. Park, J.-W., Kim, B.-K., Kim, H. J. & Park, S. Experimentation and simulation of tin oxide deposition on glass based on the SnCl4 hydrolysis in an in-line atmospheric pressure chemical vapor deposition reactor. *Thin Solid Films* **550**, 114–120 (2014).

11. Versteeg, H. K. & Malalasekera, W. *An introduction to computational fluid dynamics: the finite volume method*. (Pearson Education Ltd, 2007).

12. ANSYS, Inc. *Fluent 2020 R1 User's Guide* (2020)

13. Mol, van, A. M. B. Chemical Vapour Deposition of Tin Oxide Thin Films. (Technische Universiteit Eindhoven, Netherlands, 2003)

14. Marrero, T. R. & Mason, E. A. Gaseous Diffusion Coefficients. *Journal of Physical and Chemical Reference Data* **1**, 3–118 (1972).

15. Petrovic, Z. The Application of Blanc's Law to the Determination of the Diffusion Coefficients for Thermal Electrons in Gases, *Aust. J. Phys* **39**. 237-47 (1986)

16. Chapman,.S., and Cowling, T. C. *The Mathematical Theory of Non-Uniform Gases. 3rd Edition* (Cambridge University Press, New York,1970)

17. ANSYS, Inc. *ANSYS Fluent Fluid Simulation Software*. website: https://www.ansys.com/products/fluids/ansys-fluent (2022)

18. Autodesk. *Computational fluid dynamics simulation software*. website: https://www.autodesk.com/products/cfd/overview (2022)

19. Eriks. *High Purity Valves, Instrumentation, Hoses, Seals, Elastomer and Plastic Guide*. (2022)

20. Protolabs. *Metal 3D Printing Service*. website: https://www.protolabs.com/services/3d-printing/direct-metal-laser-sintering/ (2022)

4 Characterization of MABr and $SnBr_2$ films

4.1 Motivation

The results presented in this chapter are the characterizations of thin films prepared after numerous precursor, reactor design, and process iterations. The goal was to deposit uniform films suitable for analysis, which would provide input data to fit a CFD/CVD reactor model. The acceptability criterion was a process that repeatably produced the desired films without precursor decomposition or severe gas-phase particle generation. The films were evaluated against this criterion using several techniques. X-ray Photoelectron Spectroscopy (XPS) and X-ray diffraction (XRD) were used to identify the compound produced. Scanning electron microscopy (SEM), profilometry, and Energy dispersive X-ray spectroscopy (EDS) were used to ensure that the processes afforded continuous coverage and avoided the generation of large, gas-phase particles. Attenuated Total Reflection Fourier-Transform Infrared Spectroscopy (ATR-FTIR) and Raman spectroscopy were used to determine if C and O contamination in $SnBr_2$ films could be assigned to specific molecules. Finally, EDS was used to help fit a CFD/CVD model.

4.2 Compound Identification

4.2.1 X-Ray Diffraction

XRD was used to determine the crystal structure of the deposited material, and, together with elemental analysis, identify the deposited materials. XRD is a characterization technique that

exposes a material to plane-parallel X-rays and measures the elastically scattered output intensity at specific angles of incidence. If the material is crystalline, the scattered X-rays may reveal information regarding orientation of the crystals, the degree of crystallinity, lattice constants, and many more attributes. The results in this thesis used a Bruker D8 Discover in High-Resolution XRD mode (HRXRD) with Cu Kα 1.54 Å radiation and a LYNXEYE detector.

4.2.1.1 MABr XRD Analysis

The XRD pattern of Figure 4-1 showed peaks corresponding to the MABr (001) family of planes. This indicated a highly textured crystal growth. The Si substrate was observed at 33°.

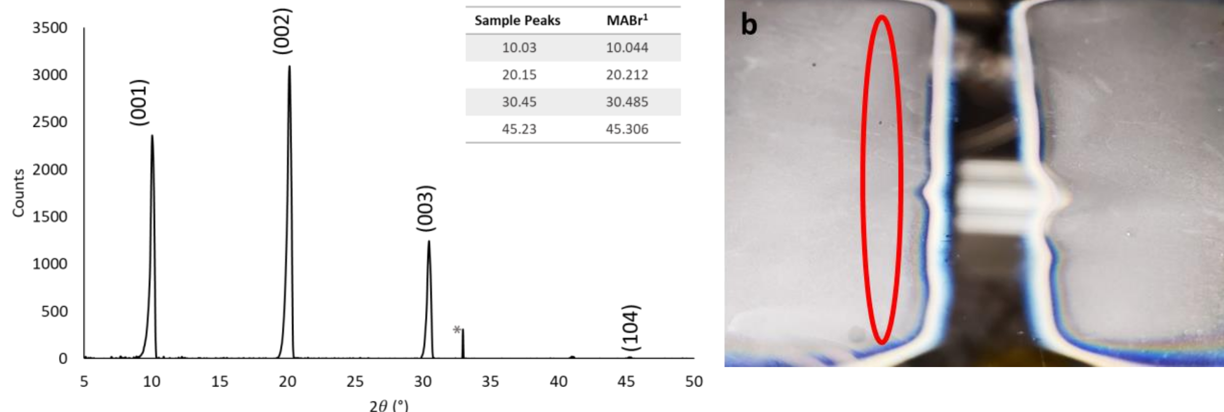

Figure 4-1: HRXRD of a MABr film deposited at 120 °C with 0.26 sccm of MA and 0.45 sccm of HBr with the reference MABr peaks[1] in the inset table. The three highest peaks shown correspond to the (001) family of planes. The small peak * near 33° is the Si substrate peak, Si (211)[2]. (b) Image of the MABr film deposited on Si wafer used in the XRD analysis. The red ellipse indicates the area of analysis.

XRD was also performed for a range of deposition temperatures, as shown in Figure 4-2. Despite the number of different smaller peaks, the (001) family of planes contributes ca. 90% of the net MABr XRD intensity. The appearance of the smaller peaks may be due to several reasons,

notwithstanding possible gas phase powder formation. However, the strong orientation of these films towards the [001] direction suggests that gas phase powder formation is negligible. Furthermore, these films passed the "Scotch tape" test showing good adhesion.

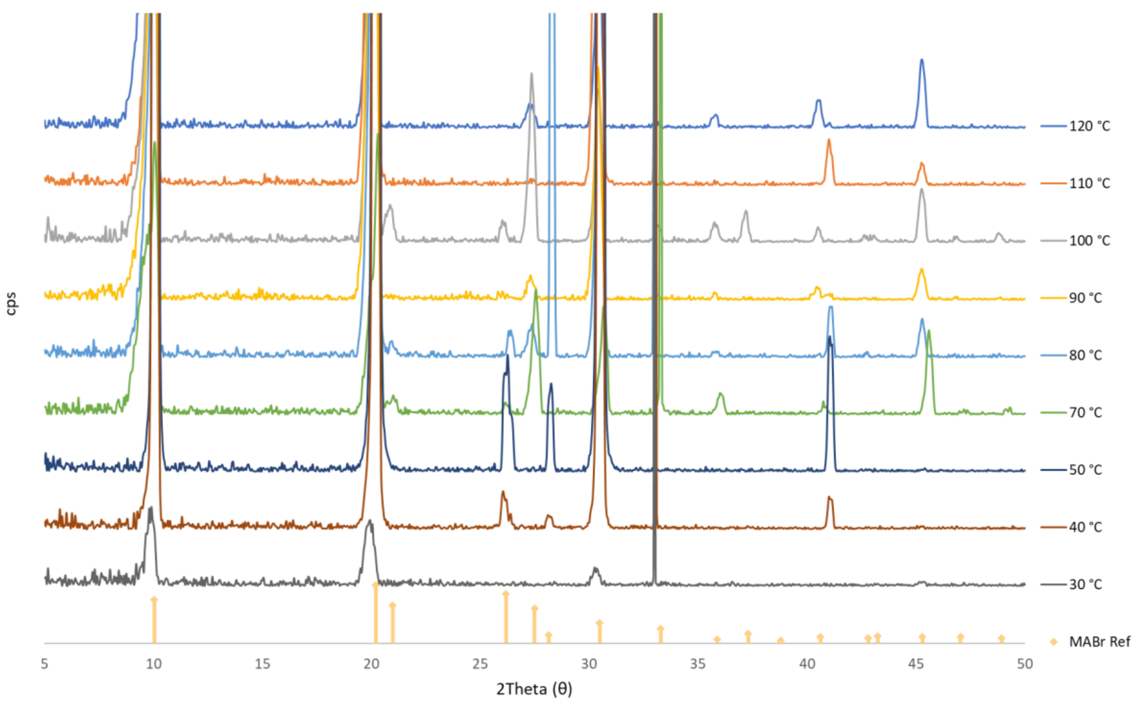

Figure 4-2: XRD of several MABr depositions at various temperatures. All peaks may be accounted for (MABr Ref) assuming ±0.5° uncertainty.[1] It is striking to see so many different peaks, and it remains unclear which deposition parameters most affect crystallinity.

4.2.1.2 $SnBr_2$ XRD Analysis

$SnBr_2$ films were analyzed with the same XRD system as with MABr. Because no XRD database for $SnBr_2$ was available, a $SnBr_2$ powder standard was made from commercially available $SnBr_2$ (99%, Beantown Chemical). As seen in Figure 4-3a, a series of three harmonic peaks at 13.5°, 27.1°, and 41.3° indicated the film is highly textured, suggesting minimal gas-phase powder formation. The distinction between "front" and "middle" in Figure 4-3a is made in Figure 4-3b,

where the "front" of the sample represented the edge of the deposition zone closest to the gas injector manifold inlet and the "middle" of the sample represented an area in the middle of the film. The sample in Figure 4-3b does not correspond to the sample analyzed by XRD but demonstrated a morphology difference observable by eye, typical of many $SnBr_2$ films in this work deposited at high temperature (>100 °C). The general trend was greater material deposition at higher temperatures led to larger, disparate crystalline rods, as also seen in the SEM micrographs (*vide infra*). It was hypothesized that the area in the middle of the film with less crystallinity (but also less material) observed by eye would have a weaker XRD signal and may even be largely amorphous. Table 4-1 shows the middle of the film, indeed, had a weaker XRD signal than the front of it. However, this difference is less pronounced than the appearance by eye and may be convoluted by the reduction in sample thickness further from the reactor center.

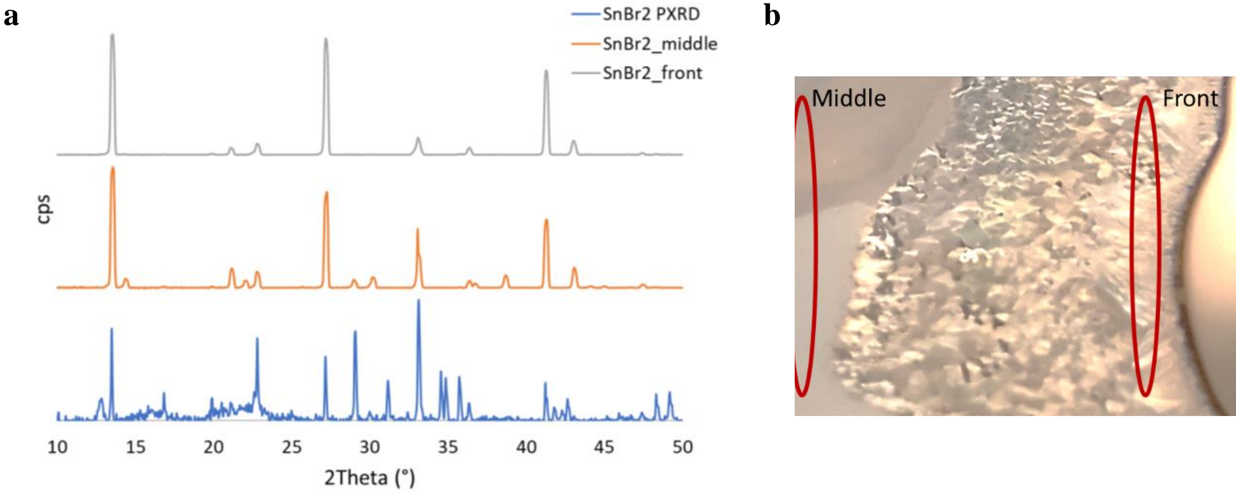

Figure 4-3: a) XRD of $SnBr_2$ film deposited at 120 °C with 0.4 sccm HBr and ca. 0.05 sccm $Sn(acac)_2$ for 15 min. The "front" and "middle" of the film can be seen in the example image in b), where the front is the area closest to the gas injector inlet manifold and the middle is further away.

Table 4-1:	∑ Harmonic Peak Areas	Total Sample Signal	Percentage of Total
Front	117000	103000	88%
Middle	31000	44000	70%

Contrary to the XRD patterns of Figure 4-3, Figure 4-4 shows almost no evidence for $SnBr_2$ formation suggested by the absence of the harmonic peaks and incongruency with the powder XRD spectrum. The absence of similar harmonic peaks can be attributed to the reduced amount of mass deposited and shorter deposition time in this temperature series of films than in the film in Figure 4-3, which was deposited for 3× longer. This is consistent with the trend in Table 4-1 and EDS results (*vide infra*), which show reduced signal further from the front of the sample suggesting less material was deposited. Interestingly, there are several peaks near 30° indicating some crystalline morphology. These may be strained $SnBr_2$ crystals corresponding to peaks in the $SnBr_2$ powder spectrum at 29°, 30°, and 31°. The total intensity from these peaks was an order of magnitude less than that observed in the middle area of Figure 4-3, suggesting less crystallinity, less material, or, likely, both.

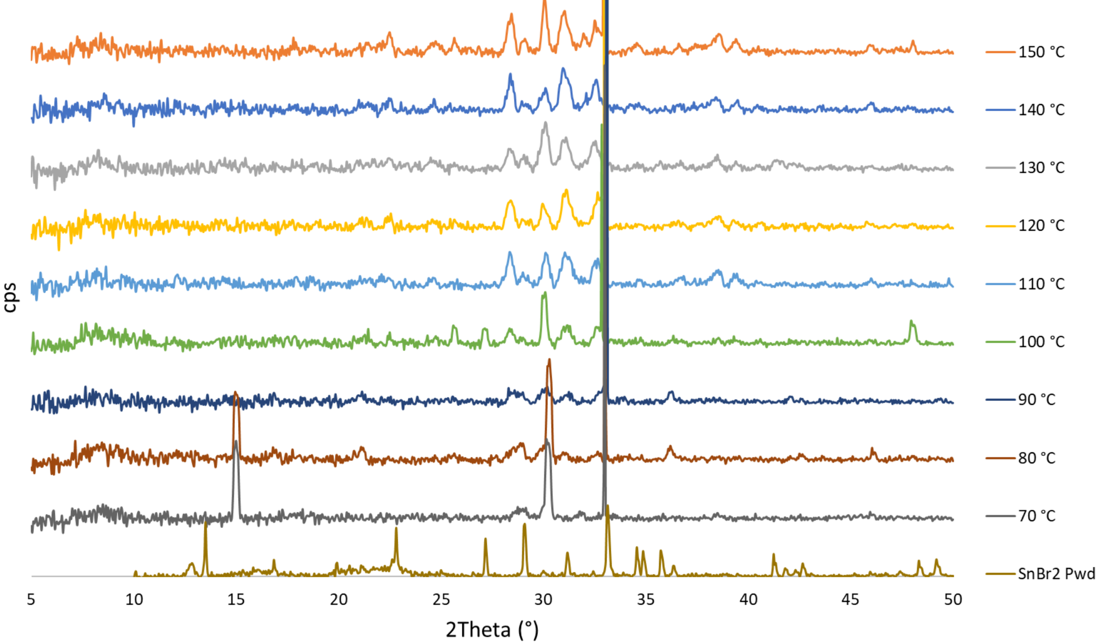

Figure 4-4: XRD patterns of $SnBr_2$ samples deposited at different temperatures. A powder XRD spectrum from commercial $SnBr_2$ powder is also shown. Note the absence of the strong harmonics observed in Figure 4-3 and the rise of several peaks near 30°. The strong peak near 33° is the Si background.

4.2.2 X-Ray Photoelectron Spectroscopy

In X-ray photoelectron spectroscopy (XPS), a sample is irradiated with X-rays, some of which collide with and eject electrons. If the electrons are sufficiently close to the surface (within 1-10 nm), these electrons may be ejected into the vacuum ($< 10^{-6}$ Pa) and collected. The resulting kinetic energy spectra of the collected electrons together with the incident X-ray energy can be used to identify the binding energy of the electrons, which represent elemental fingerprints to determine composition and chemical bonds. The XPS data was collected with a Thermo Fisher Scientific K-Alpha+ Surface Analyzer using a depth profile with 30 sec etch times and 1,000 eV Ar^+ sputtering at high current.

4.2.2.1 MABr XPS Analysis

The XPS spectra for a representative MABr film was consistent with the formation of MABr by evidence of a 1:1:1 ratio of C, N, and Br, as seen in the atomic percentage data of Figure 4-5 from high-resolution scans of the elements. The measurement accuracy is expected to be no better than ± 1 at.%, which suggests the composition percentages appearing between 32–34% are within the error bounds of the experiment. The slightly higher concentration of carbon at the surface was due to adventitious carbon from the environment.

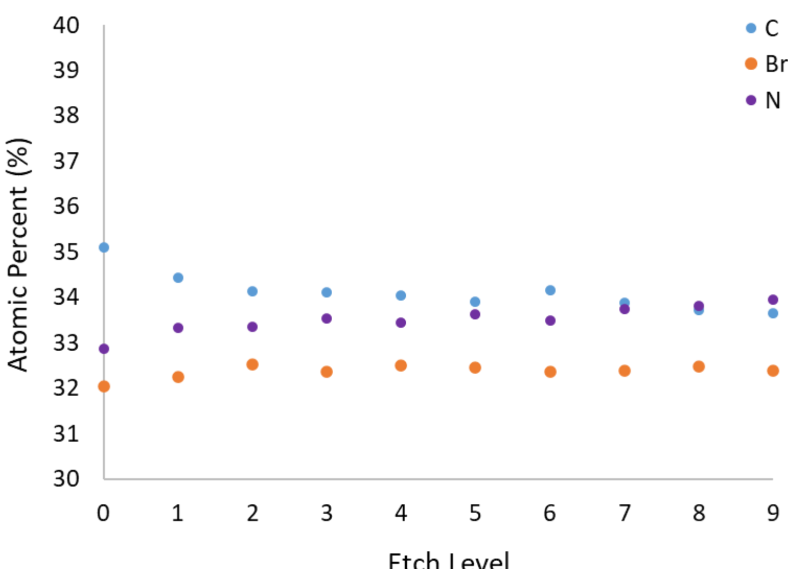

Figure 4-5: XPS atomic percent of a representative MABr film deposited at 120 °C for 5 min with 0.45 sccm of HBr and 0.25 sccm of MA.

4.2.2.2 $SnBr_2$ XPS Analysis

XPS characterization of $SnBr_2$ deposited on Si was less definitive. As seen in Figure 4-6a, the ratio of the elements near 400 s of etching is consistent with 2.5% SnO_2 and the remainder

$SnBr_2$ (excluding Si counts from the substrate). However, as the etch duration continued, the concentration of Br appeared to decrease relative to O and Sn, concomitant with an increase in Si. This would suggest Br was preferentially etched during the measurement. The apparent loss of Br also appeared to coincide with a rise in the metallic Sn signal in Figure 4-6b. It was hypothesized that the concentration of Sn and O did not change significantly compared to Br, because the increase in the relative concentration of Sn and O due to the faster loss rate of Br offset the reduction in absolute concentration of Sn and O due to etching (the film was porous, so the Si substrate was always sampled).

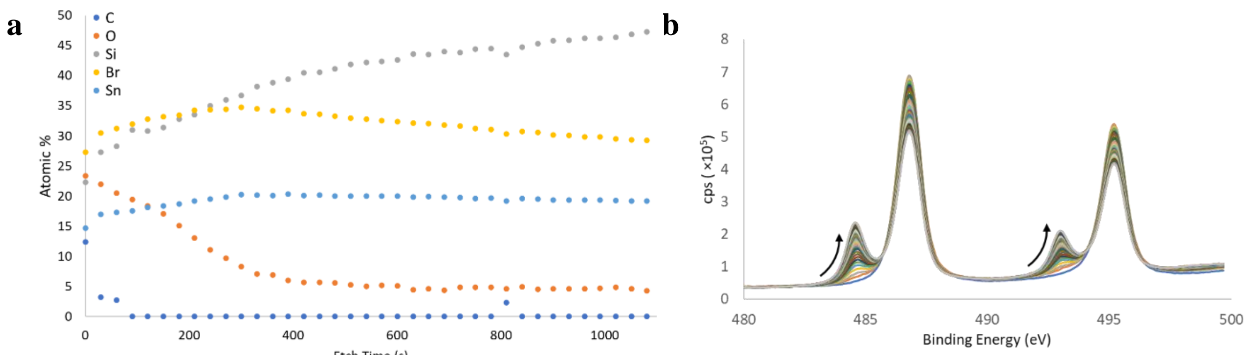

Figure 4-6: (a) Atomic percentages from an XPS spectra of a representative $SnBr_2$ film deposited at 140 °C and 0.4 sccm HBr and 0.05 sccm $Sn(acac)_2$. (b) High-resolution spectra of the Sn energy window showing an increase in the metallic Sn^0 signal with depth profiling.

To better understand this anomaly, a $SnBr_2$ standard was measured. The standard was made by melting $SnBr_2$ sandwiched between two Si wafers inside a glovebox. Upon cooling, the wafers were separated to reveal a relatively flat surface suitable for XPS. The atomic percentages of Sn and Br derived from the XPS spectra of the standard vs etch time, for the same measurement conditions as in Figure 4-6, is shown in Figure 4-7a, and the Sn high-resolution scans for each etch level are shown in Figure 4-7b. Near 400 s of etching, the ratio of Br:Sn is nearly 2:1 (note, C and O were intentionally not measured to speed up the experiment). However, the Br signal decreased

over time and similarly occurred with an increase in the signal of metallic Sn. This suggested that either the X-ray exposure or etching process may have caused a reduction in the Sn and oxidation of Br via reaction (4-1)

$$SnBr_2 \rightarrow Sn^0 + 2Br \quad (4\text{-}1)$$

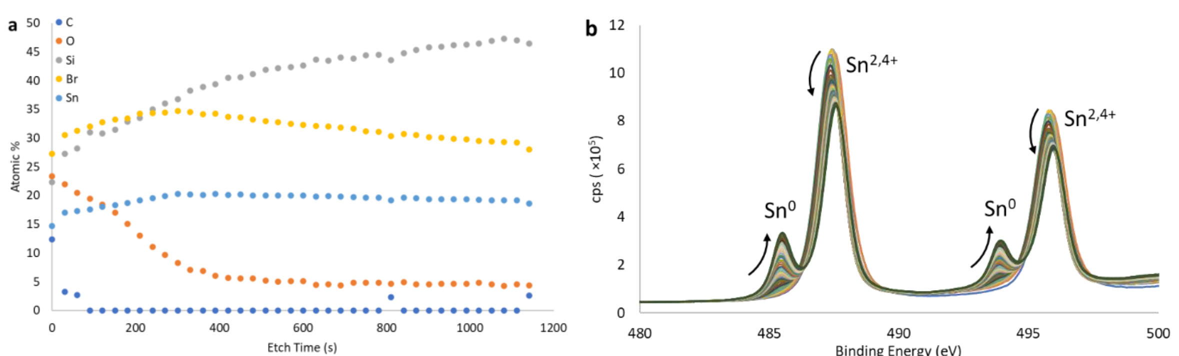

Figure 4-7: a) Atomic percentages derived from high-resolution XPS spectra of the $SnBr_2$ standard. b) High-resolution spectra of the Sn region for each etch level indicated an increase in Sn^0 over time.

To discern whether the X-ray beam or etching process caused the unexpected loss in Br, a series of measurements on the $SnBr_2$ sample were made. These measurements included depth profiling with minimal X-ray exposure by performing only 1 pass of the energy filter per etch level (as opposed to 10, previously) and blanking the X-ray beam during the etching process. The etching conditions were 1,000 eV monotomic Ar^+ at high current (the same as previously), 1,000 eV Ar^+ at low current, and 8,000 eV Ar cluster etch (approximately 1,000 Ar atoms per cluster). The results from these experiments demonstrated that the reduced X-ray exposure had little to no effect on reducing the amount of Br loss, and instead, showed that the etching rate had a significant effect, as shown in Figure 4-8. The rate of Br:Sn ratio reduction between the $SnBr_2$ sample and standard is nearly the same for the same etching conditions (1,000 eV monatomic high current)

and very different X-ray exposure times – the blue curve had less than one-tenth the exposure time of the yellow curve in Figure 4-8. However, after nearly 9,000 seconds of etching at 1,000 eV with Ar^+ at reduced current, the ratio of Br:Sn is nearly constant (orange curve). Therefore, future work using XPS for quantitative analysis should use low etching currents when analyzing $SnBr_2$.

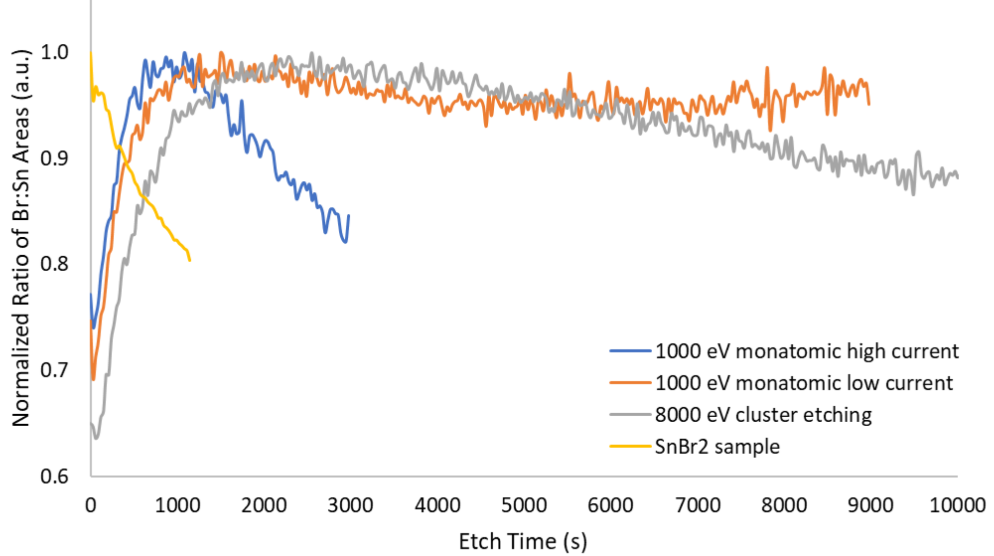

Figure 4-8: Normalized ratio of Br signal area to Sn signal area from high-resolution XPS depth profiling scans on a $SnBr_2$ standard and sample.

4.3 Morphology Characterization

The CVD model relied not just on composition variation but also on mass deposition variation to distinguish each reaction model's contribution and the importance of precursor diffusion to the amount of film deposited. To illustrate this, Figure 4-9a depicts four reaction mechanisms' spatial dependencies. Figure 4-9b shows MABr profilometry data, as a proxy for spatially dependent mass data, that suggested multiple reaction mechanisms would be required to completely model the deposition process. Previous attempts to translate the substrate under the reactor gas injector during deposition would convolute the impact of these different mechanisms

to the effect of reducing the modeling capability. Therefore, only static depositions were performed for the data presented for modeling.

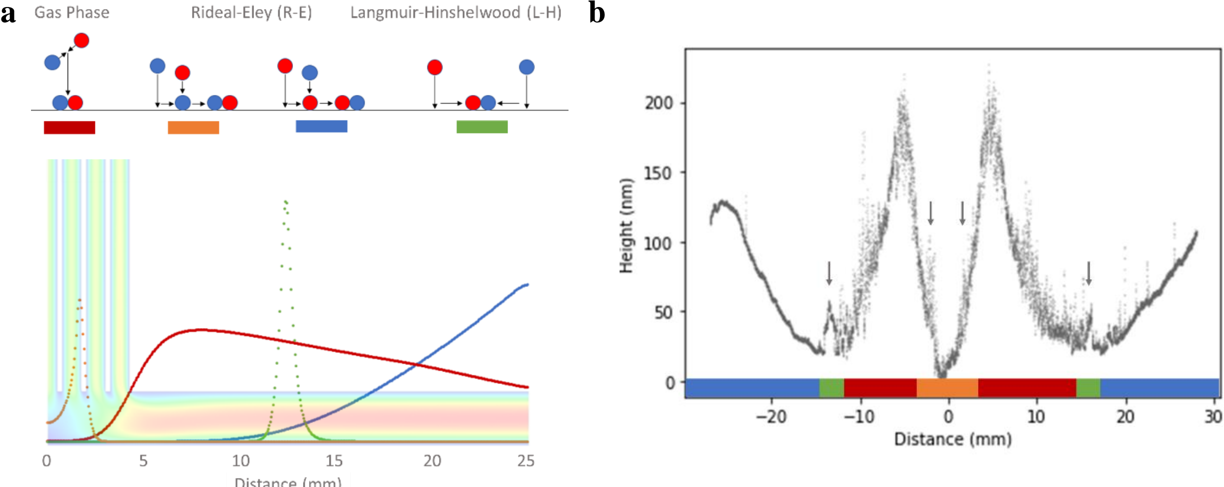

Figure 4-9: (a) The 4 reaction models considered show strong spatial dependencies. Four generic simulations for the deposition of MABr, one for each reaction model, are overlayed on half of the corresponding velocity map of the Gen 1 reactor. (b) MABr profilometry data for a deposition at 60 °C with 0.13 sccm of HBr and MA suggests multiple reaction mechanisms determined the film thickness. The color bar corresponds to the different reaction mechanisms suggested in (a). The arrows indicate possible contributions from gas-surface reactions to the overall film deposition.

4.3.1 Scanning Electron Microscopy

Scanning Electron Microscopy (SEM) was used to characterize the surface of the films and ensure they were free of particle clusters formed in the gas-phase. Analysis of gas-phase particle formation was not within the scope of this thesis, so no attempt was made to cause and or study this phenomenon. Instead, SEM images were collected to make sure the inlet precursor concentrations were sufficiently low and the N_2 curtain gas flow rate sufficiently high to prevent particle formation. Additionally, for $SnBr_2$ depositions, SEM images were used to determine the deposition time limit to prevent unwanted crystal growth that would drastically roughen the surface

and make further characterization challenging, if not impossible. All images were collected at an accelerating voltage of 12 keV and a working distance of 10 mm, if not otherwise specified, using a Jeol JSM-7900f FESEM or Zeiss Ultra Plus FESEM.

4.3.1.1 MABr SEM

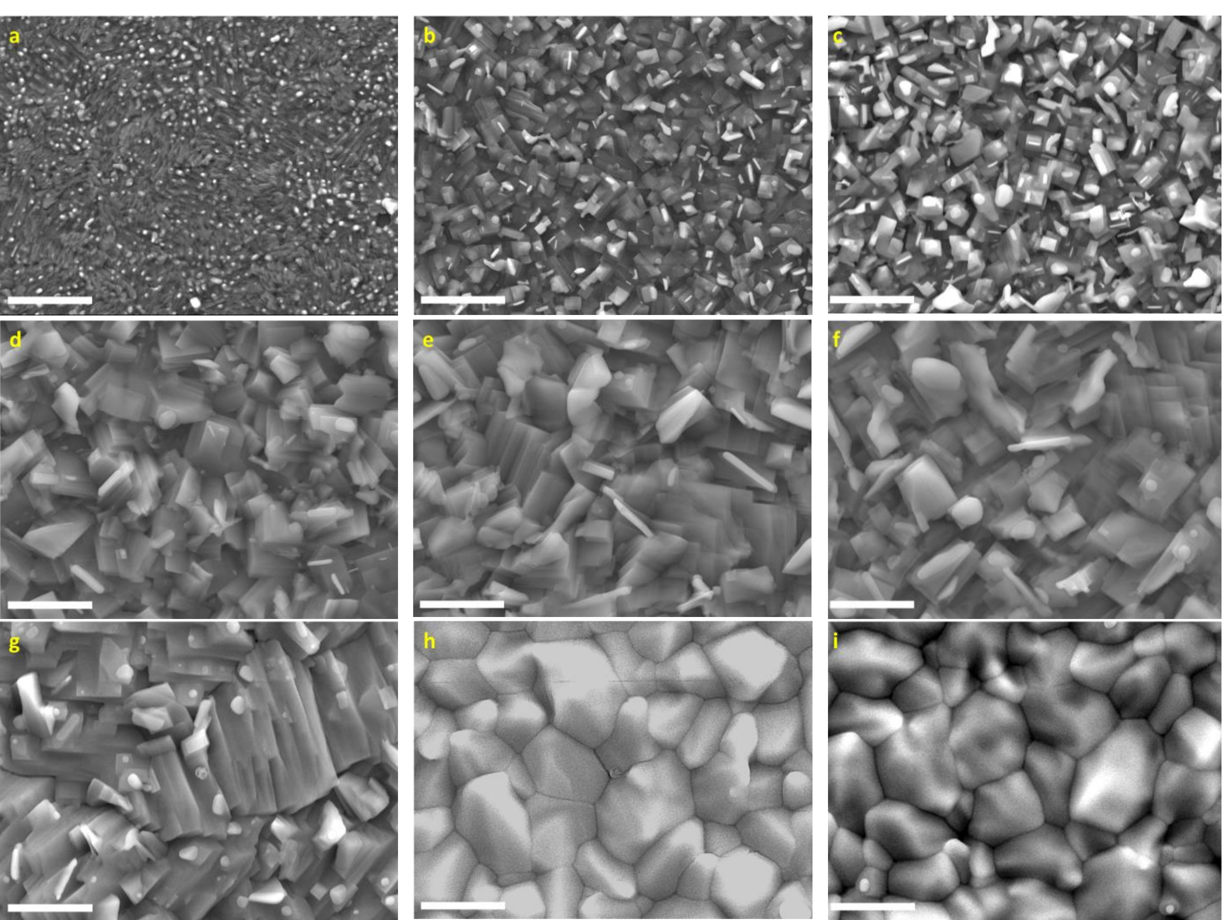

Figure 4-10: MABr SEM images (a-i) correspond to films deposited at increasing temperatures (30 °C, 40 °C, 50 °C, 60 °C, 70 °C, 80 °C, 90 °C, 110 °C, and 120 °C). The crystallites increased in size with increasing deposition temperatures from 30—90 °C, and then between 90—110 °C, they coalesce to form a smoother surface. This coincides with the growth transition from reaction rate limited to mass transport limited, although no conclusion on the effect of this transition on morphology was considered. The scale bar is 5 μm.

The SEM images of Figure 4-10 show a rough film that increased in surface roughness up to 90—110 °C deposition temperature (a-g) and then appeared to smoothen thereafter. This may be a combination of film softening at higher temperatures and the film coalescing to reduce the surface area as the film thickness increased, among other potential reasons. Noteworthy, the film appeared uniform in texture and absent of any large ($> 10\ \mu$m) particle deposits.

4.3.1.2 $SnBr_2$ SEM

Unlike MABr, $SnBr_2$ only forms smooth, continuous films at low temperatures. Above a ca. 70 °C and with enough deposited material, $SnBr_2$ films will rapidly crystallize into characteristic $SnBr_2$ rods. The progression from smooth to sparse "films" is shown in Figure 4-11.

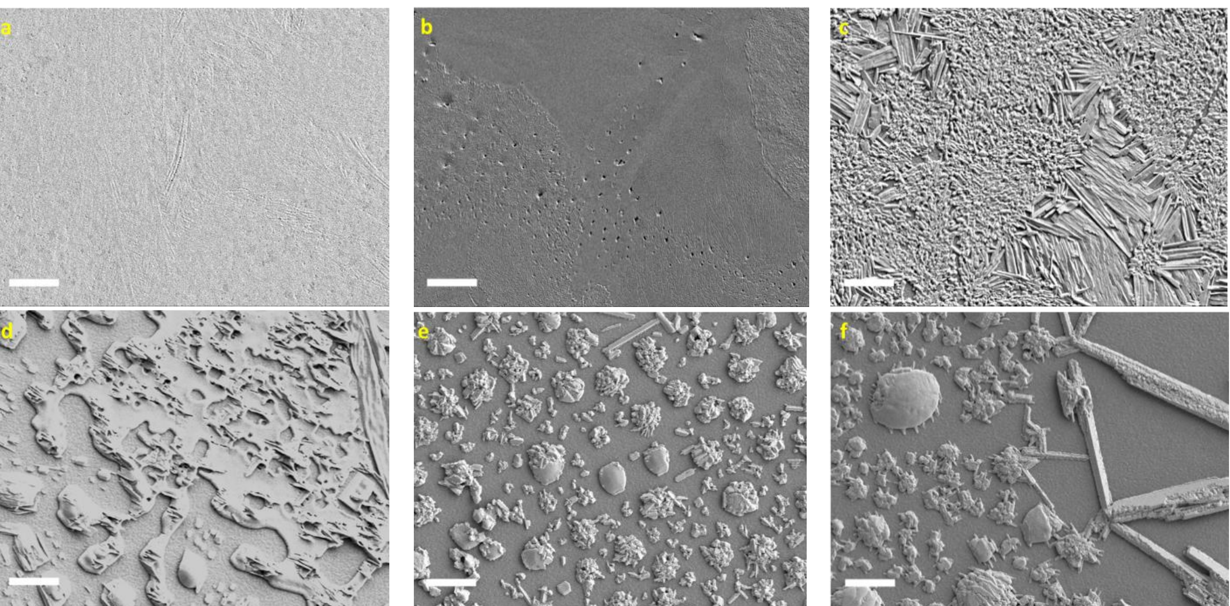

Figure 4-11: (a-f) SEM images of $SnBr_2$ depositions on Si at temperatures 50 °C, 60 °C, 70 °C, 80 °C, 90 °C, and 100 °C, respectively. Note the transition from a smooth surface at lower temperatures to a rough, porous "film" at higher temperatures. The relative ease of $SnBr_2$ crystal formation is responsible for the film disaggregation into small (or large) crystals. This has also been a problem in the literature for forming pin-hole free tin-based perovskites.[3] The scale bars are 5 μm.

If given sufficient time, temperature, and a high enough precursor concentration in the gas phase, $SnBr_2$ formation can proceed very far from the surface and generate a “forest” on the substrate, as seen in Figure 4-12.

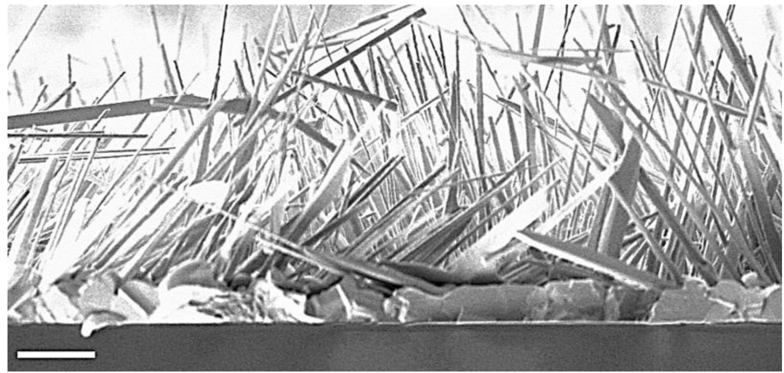

Figure 4-12: SEM cross-sectional image of a $SnBr_2$ “forest” deposited at 160 °C for 20 min with $Sn(hfac)_2$ at a source bubbler temperature of 65 °C. The accelerating voltage was 3 keV at a working distance of 7 mm. The scale bar is 10 μm.

To limit this uncontrolled growth behavior of $SnBr_2$ for characterization, the deposition time and precursor concentration were limited. This aided forming a uniform deposition without large outgrowths away from the surface that would shadow and distort analysis. The $SnBr_2$ films in Figure 4-13 are composed of many small islands likely because of a high surface free energy mismatch for $SnBr_2$ on SiO_x.

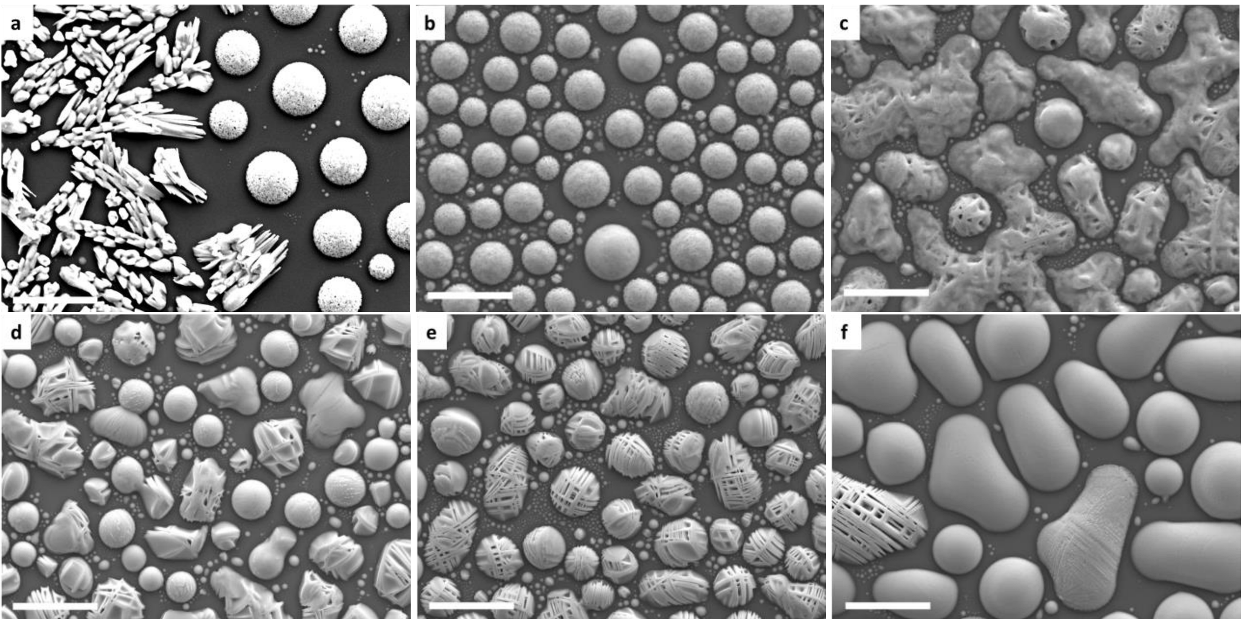

Figure 4-13: SEM images of $SnBr_2$ depositions showing a mixture of nano/microcrystals with amorphous material. It was important for later EDS analysis that these samples do not have large overhanging features which could obscure the electron beam, not be too thick, and that the samples be homogenous. (a-f) were deposited at temperatures of 70, 80, 100, 110, 120, and 130 °C and 0.4 sccm of HBr and 0.05 sccm of $Sn(acac)_2$. The scale bar is 10 μm.

4.3.2 Profilometry

Profilometry was used to characterize the spatial variation in thickness. In a typical experiment, a film was deposited on a silicon wafer (no pre-etching), and the edge of the film was removed by mechanically rubbing the surface with a Q-tip soaked with isopropanol to expose approximately 2 mm of the bare wafer. This section was first scanned with the profilometry to determine the tilt correction to apply to the stage and if there was any non-linear deviation in the measured height. Once the stage tilt was corrected, the sample was measured with a 5 μm radius tip and 3 mg of contact force.

To demonstrate that the profilometer reasonably captured the thickness variation across the sample, a comparison was made to an SEM cross-section. As seen in Figure 4-14, the profilometer was able to measure the film thickness with decent accuracy. Moreover, the profilometer could

provide data on the roughness of the film at the micron scale, although this information was not considered in later analysis. All profilometry experiments were conducted using samples from the Gen 1 reactor.

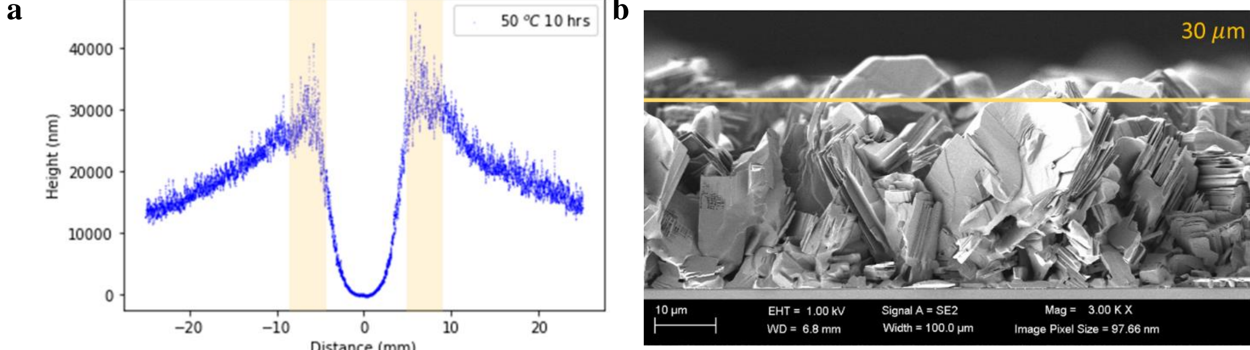

Figure 4-14: (a) Profilometry data and an SEM cross-section (b) of a 10 hr deposition of MABr at 50 °C and 0.043 sccm of MA and HBr. The SEM cross-section was viewed near the film peak thickness within the vanilla bands in (a). The yellow bar across the top of the SEM image indicates a height of 30 μm as measured by the scale bar. This height matches that expected in the profilometry data in the vanilla bands. The profilometry also captures the film roughness apparent in the SEM image.

4.3.2.1 MABr Profilometry

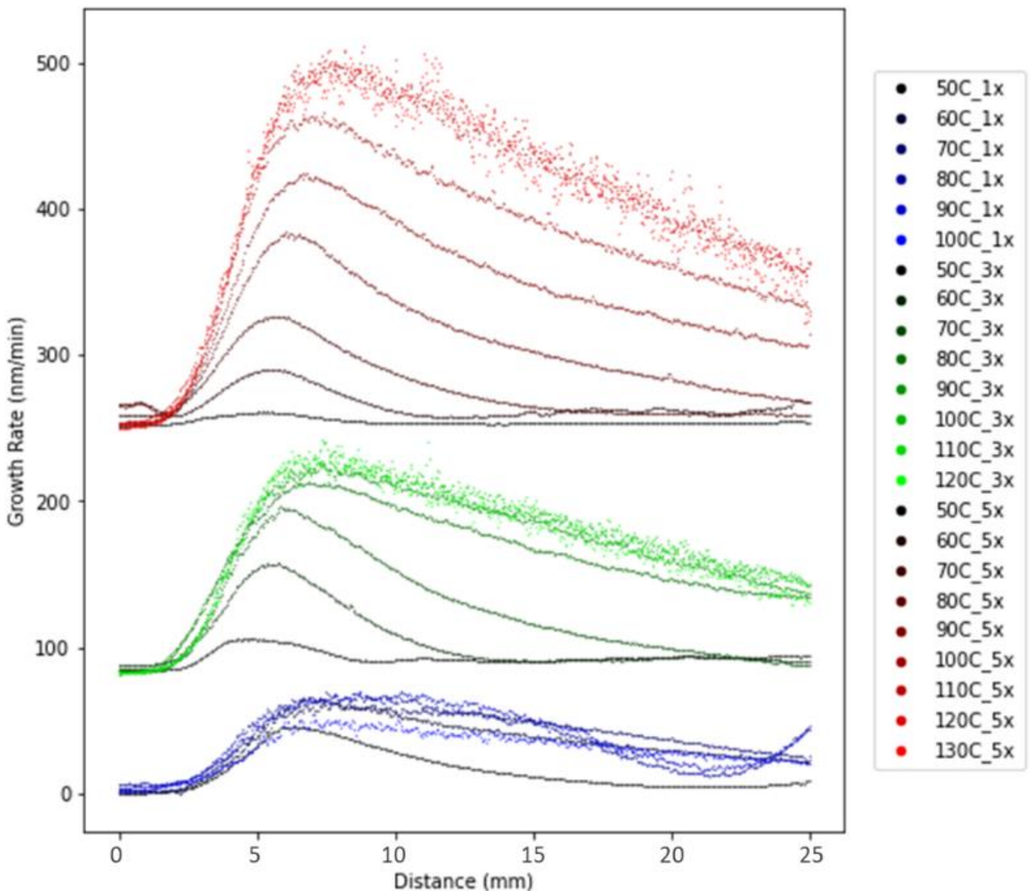

Figure 4-15: Profilometry data for MABr films deposited on Si wafers. The legend indicates the isothermal temperature of the reactor and the factors 1x, 3x, 5x indicate multiples of a baseline precursor flowrate of 0.043 sccm for MA and HBr (e.g. 110C_3x was MABr deposited at 110 °C with 0.13 sccm of MA and 0.13 sccm of HBr). These films were produced with the Gen 1 reactor.

Figure 4-15 shows the growth rate variation across the sample where the growth rate was determined by normalizing the profilometry height data by the duration of the deposition. Additionally, due to the symmetry of the reactor, the profilometry data was averaged about the symmetry plane in the center of the sample to help offset the effects from any slight asymmetry in the flow. This is opposed to Figure 4-9b where the data is presented without averaging. The plots

corresponding to the same flow rate of precursors (0.043 sccm, 0.13 sccm, or 0.22 sccm) were offset for clarity.

Based on the shapes of the thickness variation and those in Figure 4-9a, there appeared to be a possible gas phase reaction contribution to the film thickness at higher temperatures. However, there are also indications of Rideal-Eley (R-E) reactions at either the lower flow rate and higher temperature (near 25 mm) or lower temperature and higher flow rate (near 0 mm). Overall, this profilometry data suggests the MABr deposition process could be modeled by the simple reaction mechanisms proposed.

The average growth rate was calculated by normalizing the average profilometry height across 50 mm of the sample by the deposition duration. This data was used to determine the trend in growth vs temperature and duration. Figure 4-16a demonstrates that the average growth rate appeared constant vs deposition duration up to 60 min and then increased beyond that. However, this trend may have been an artifact of the stylus' inability to effectively track the topology of the film as the film became rougher or the film porosity increased. This is discussed further in the following paragraphs and is one reason the profilometry data was not used for modeling.

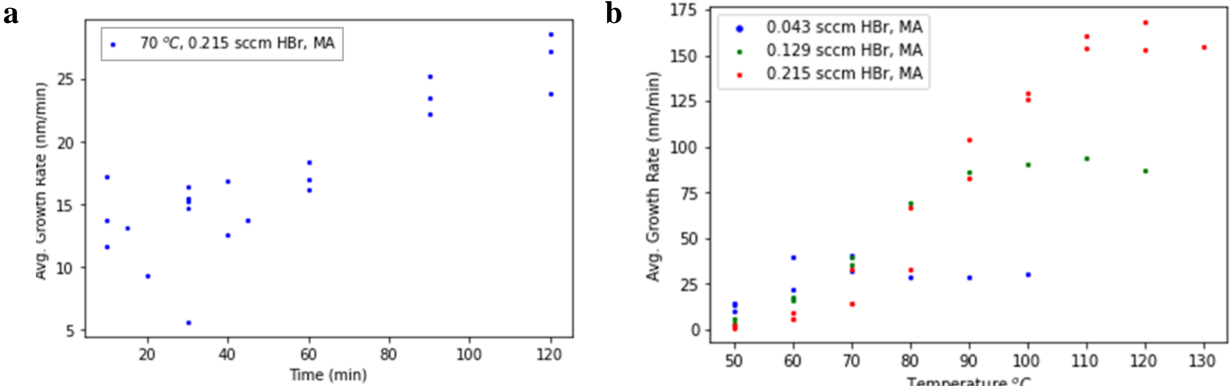

Figure 4-16: The average growth rate (nm/min) was calculated by normalizing the average profilometry height across 50 mm of the sample by the duration of the deposition. (a) Experiments that varied the deposition duration while keeping the temperature fixed at 70 °C suggested the average growth rate was constant up to 60 min and then increased beyond 60 min of deposition. (b) When the temperature was varied and the deposition duration was fixed at 30 min, the average growth rate appeared to linearly increase until a saturation plateau was reached.

Assuming the deposition rate is constant up to 60 min, films were deposited for 30 min at varied reactor temperatures to determine the effect of temperature on the growth rate. Figure 4-16b shows that the growth rate linearly increased with temperature until saturating at a level dependent on the precursor flow rate. When the precursor flow rate increased by factors of 3 and 5, the growth rate saturation increased by approximately the same factor. This suggested that the growth rate was reaction rate limited below the saturation temperature and mass transport limited above it. The mass transport limitation was expected to be due to diffusion and the limit of mass flow into the reactor. As seen in the velocity map of Figure 4-9a, the boundary layer fully formed by 10 mm from the reactor center, which implied the dominant transportation mode to the surface beyond this point was diffusion and not advection.

To confirm the growth rate saturation was not an artifact from the profilometry measurement, the masses of deposited films were measured on a Ohaus microbalance with 0.01 mg resolution. This was done by depositing MABr on Kapton tape attached to a silicon substrate with 0.215 sccm of HBr and MA flowing for a duration of 30 min. After the deposition, the tape

was carefully peeled off the silicon substrate and attached to tare paper. This transfer was necessary to lower the total tare weight for more accurate measurements and to cut off the sides to remove edge effects on the deposition. The sample dimensions used for the mass measurements were 1.7 cm × 5 cm. The film mass was calculated by subtracting the weight of the Kapton tape after wiping off the film with a damp cloth from the weight of the Kapton tape with the deposited film. Between wiping and weighing the tape, the surface was wiped again with a dry cloth and allowed to air dry. Figure 4-17b shows results of the measurements normalized by area and deposition duration vs deposition temperature. Below 100 °C, the growth rate increased approximately linearly and saturated between 90-110 °C. These trends were consistent with the results in Figure 4-16b for 0.215 sccm of HBr and MA and supported the hypothesis that the film growth rate in the saturation region was mass transport limited.

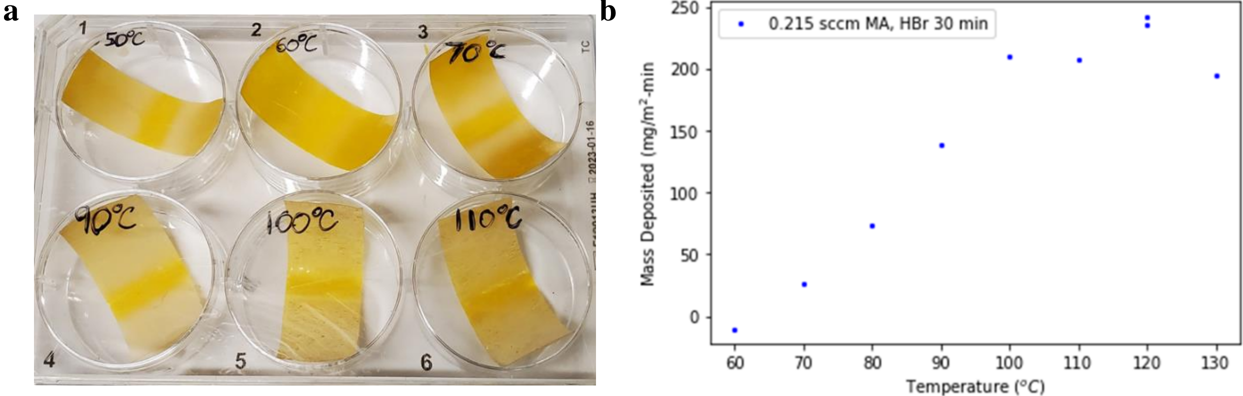

Figure 4-17: Films were deposited on Kapton tape attached to a silicon wafer with 0.215 sccm HBr and MA flowing for a duration of 30 min. (a) Sample Kapton pieces from the depositions showed a middle section without deposited material consistent with depositions directly on silicon wafers. The widths of the Kapton pieces were 1.7 cm. The remainder of the Kapton was discarded due to edge effects from the reactor walls. To weigh the film mass, the Kapton tape was transferred to tare paper, weighed on a microbalance, wiped clean with a damp cloth and dried, and then weighed again. The film mass was calculated by subtracting the weight of the clean Kapton tape from the one with MABr. (b) A plot of the area-normalized mass growth rate vs temperature showed a growth rate saturation beginning between 90-110 °C.

As mentioned, the average growth rate as seen in Figure 4-16a suggested that for deposition durations beyond 60 min, the average growth rate increased. To determine if this was an artifact of the profilometer measurement or if the growth rate was correlated to surface area, the growth rate was compared to the growth rate variance. The hypothesis was that if the growth rate increased due to an increase in surface area (and surface chemistry kinetics limited the growth rate), then the variance in the growth rate should correlate with surface roughness and, therefore, surface area. The average growth rate variance was calculated for a profilometry data series of samples deposited at 70 °C and with 0.22 sccm of HBr and MA. To calculate the variance, a ~40-order polynomial was fit to the data and used as the mean, as seen in Figure 4-18c.

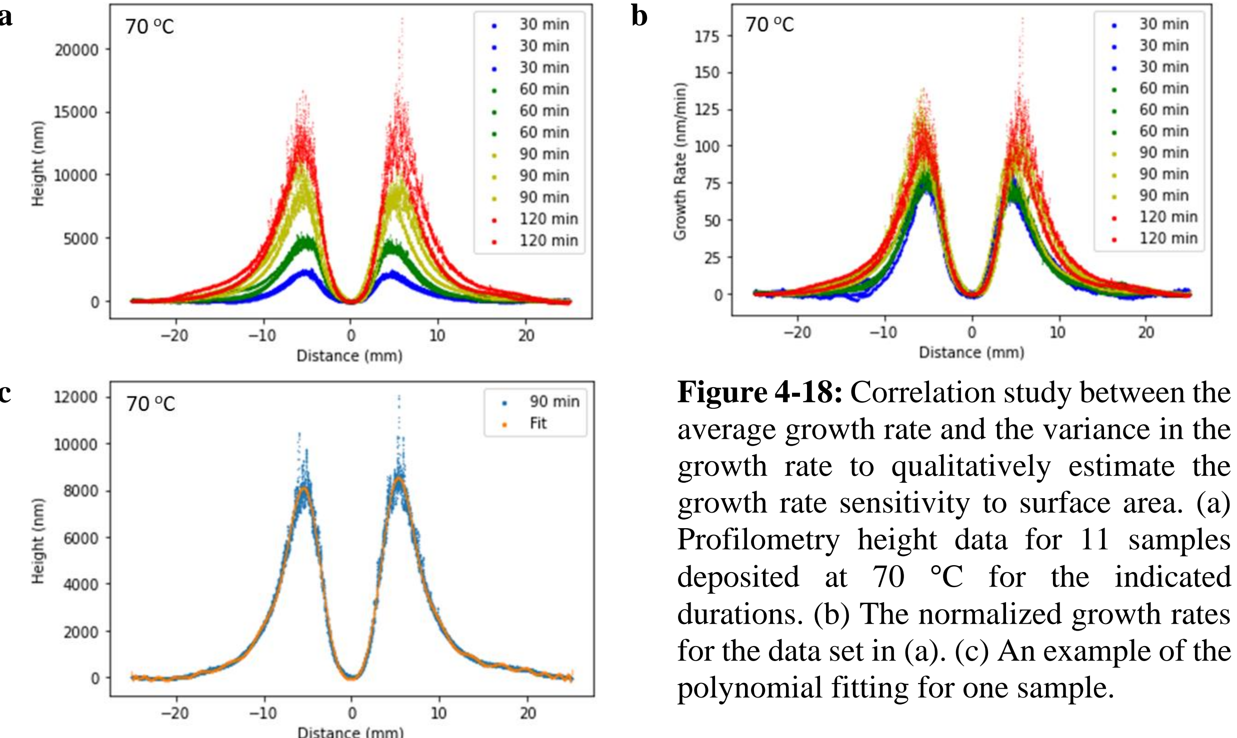

Figure 4-18: Correlation study between the average growth rate and the variance in the growth rate to qualitatively estimate the growth rate sensitivity to surface area. (a) Profilometry height data for 11 samples deposited at 70 °C for the indicated durations. (b) The normalized growth rates for the data set in (a). (c) An example of the polynomial fitting for one sample.

The results of the correlation study are shown in Figure 4-19 below. Figure 4-19a shows the average growth rate and average growth rate variance vs duration, and Figure 4-19b shows the

same data but normalized by the values for a 30 min deposition. Figure 4-19b illustrates that the normalized growth rate variance exponentially increases up to a factor of ~18× by 120 min from the value at 30 min, but the increase in the normalized average growth rate over the same deposition duration increases by less than 2×. Given surface area is correlated with film roughness, and hence growth rate variance, these results suggested that the surface chemistry was not limiting to the overall film growth at 70 °C. Furthermore, because 70 °C is within the temperature range where film growth is reaction rate dominated, these results are likely to hold for depositions at hotter temperatures approaching and into the mass transport dominated region. Thus, the increase in the average film growth rate in Figure 4-16a was suspected to be a result of the increase in film roughness and concomitant inability of the profilometer stylus to fully penetrate film voids.

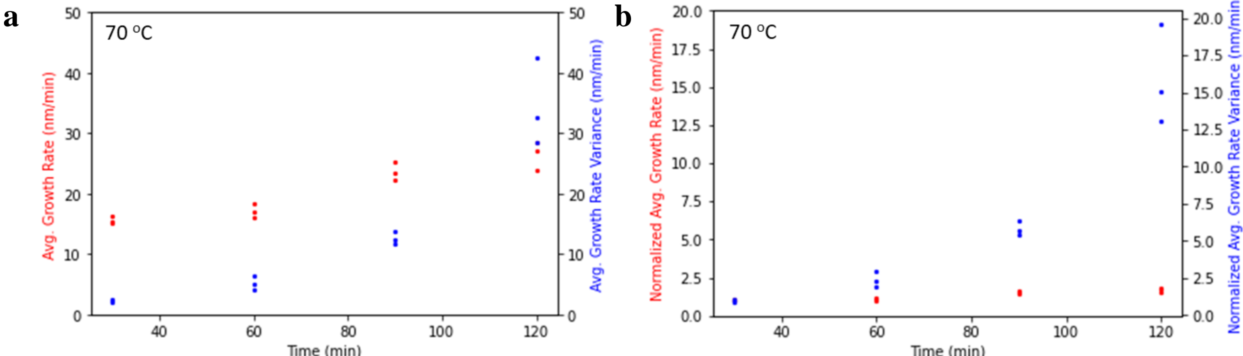

Figure 4-19: (a) Plot of the average growth rate and average growth rate variance vs duration. (b) Plot of values in (a) normalized by the values at 30 min. The trend in (b) shows the growth rate increased by ~2× while the growth rate variance increased ~18×

This latter issue of the profilometry's inability to accurately characterize a rough or porous film prompted a search for an alternative means of quantifying the spatial deposition.

4.3.2.2 $SnBr_2$ Profilometry

$SnBr_2$ was less studied with profilometry for several reasons. The first, as mentioned previously, was that profilometry failed to capture the film topography with high fidelity as the surface roughness increased. Secondly, the profilometer occasionally failed to capture even the overall trend and injected gross error into the height data. Thirdly, the profilometer could not distinguish impurities from the desired compound as it only recorded surface topography. This last reason was inherent to the deposition of $SnBr_2$, which may deposit at least four separate species in the reaction of $Sn(acac)_2$ with HBr – $SnBr_2$, SnBr(acac), SnO_2, and SnO.

However, profilometry did prove useful in cross validating the use of Energy Dispersive X-Ray Spectroscopy (EDS) to estimate the growth rate in the CFD/CVD model.

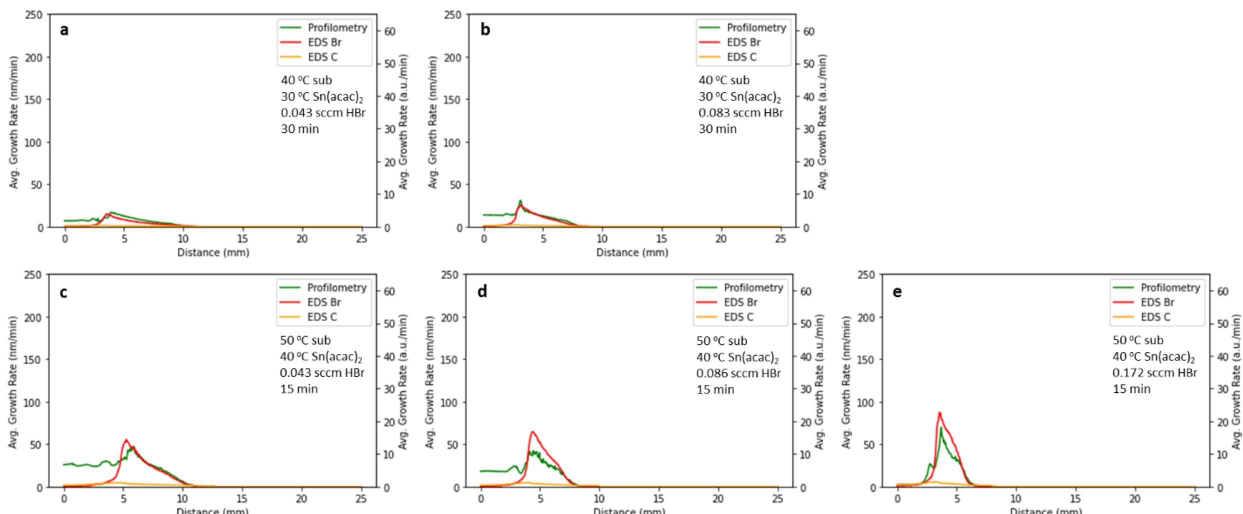

Figure 4-20: EDS and profilometry data for $SnBr_2$ depositions. The left and right axes correspond to profilometry and EDS intensity data, respectively. Note the strong correlation between the Br EDS signal and the profilometry data. All samples were made with the Gen 1 reactor.

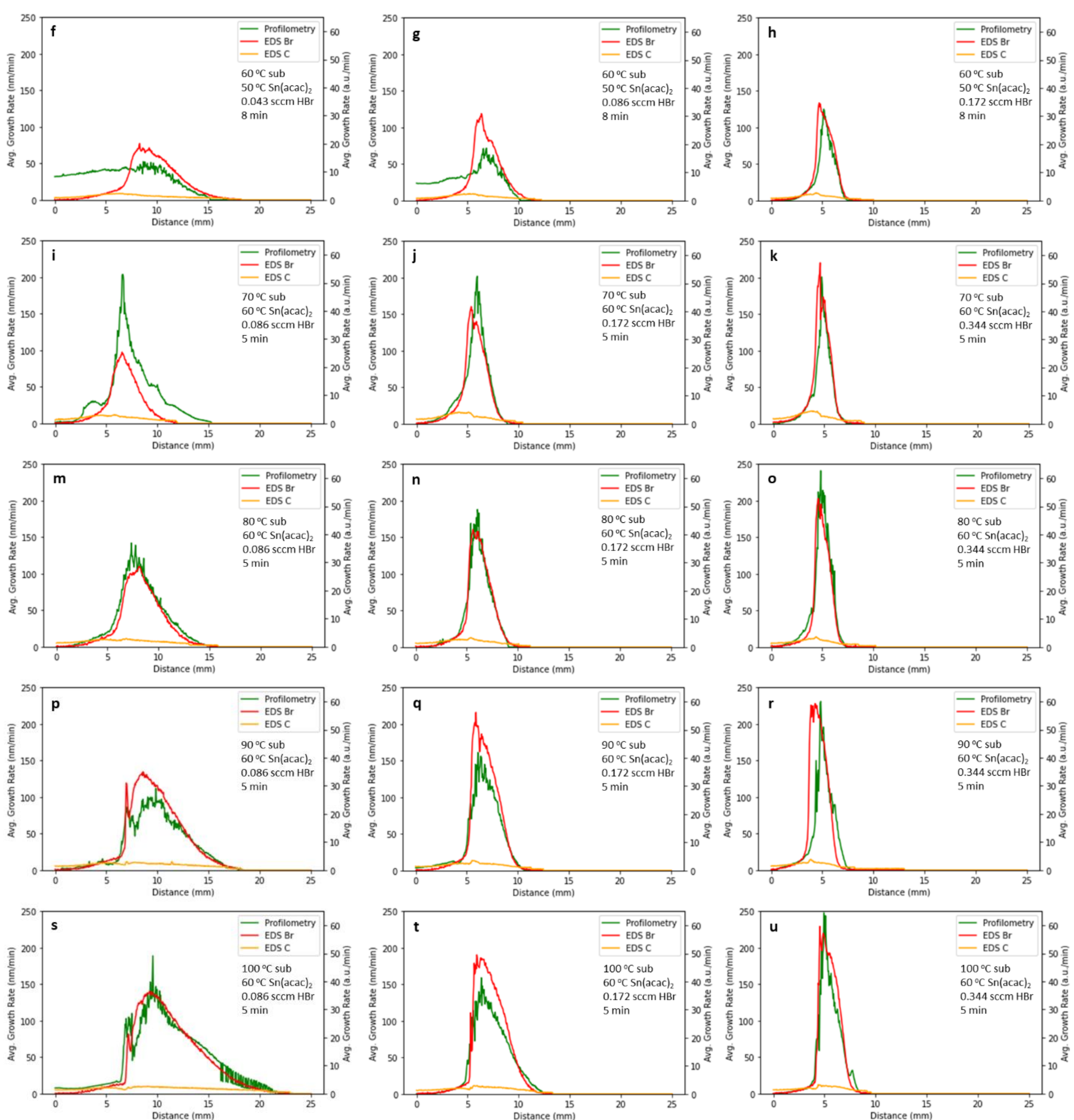

Figure 4-21 (Continued)

Shown in Figure 4-21, the $SnBr_2$ profilometry and Br EDS signals strongly overlap suggesting that EDS could be a good replacement for profilometry measurements to model the film deposition process. Note in Figure 4-21a,b,c,d,f,g where the profilometry data incurred a large

offset near the zero position (center of the reactor) that is absent from the EDS data. This was an issue with the profilometer on occasion, especially when descending a steep gradient.

Overall, the plots in Figure 4-21 suggested a trend where the spatial extent of the deposition compressed closer to the center of the reactor as the precursor concentration increased while the film appeared to expand upon increasing the temperature deposition. These effects of the deposition input parameters on the resulting film morphology and composition afford the opportunity to model the deposition process from a retrosynthetic perspective.

4.3.3 Energy Dispersive X-Ray Spectroscopy

EDS was used to measure the spatial dependence of the growth rate and fit a CFD/CVD model. EDS is a non-destructive analysis technique whereby electrons from the SEM scatter as they penetrate the sample and cause the emission of characteristic X-rays as electrons in the elements transition between states due to the collision. The X-rays are collected and processed to separate them by energy, and thereby identify the element from which they came, assuming minimal peak overlap. The system used in this work included an Ultim Max SDD EDS from Oxford Instrument attached to a Jeol JSM-7900F FESEM. To gather the spatial EDS data, a Large Area Mapping (LAM) tool from Oxford Instruments was used to automate the imaging and stitching of maps. Once collected, the maps were averaged into a line scan along the gas flow direction across the substrate. The working distance and accelerating voltage used were 10 mm and 12 keV. All EDS data collected in this section were from the Gen 2 reactor.

4.3.3.1 MABr EDS

The MABr EDS data was collected after performing a series of depositions with increasing temperature from 50—120 °C. The flow rate of the HBr was maintained constant at 0.45 sccm. The flow rate of MA was decreased from 0.26 sccm for samples deposited at 50 °C and 60 °C to 0.13 sccm for all other samples. The time for the deposition also gradually reduced from 5 min to 2.5 min. The aim of these two reductions in flow rate and time was to minimize the peak film thickness to prevent saturation of the EDS signal (the EDS signal must always measure the Si substrate to ensure the *full* sample is always analyzed). The constant background signal from each element was also subtracted.

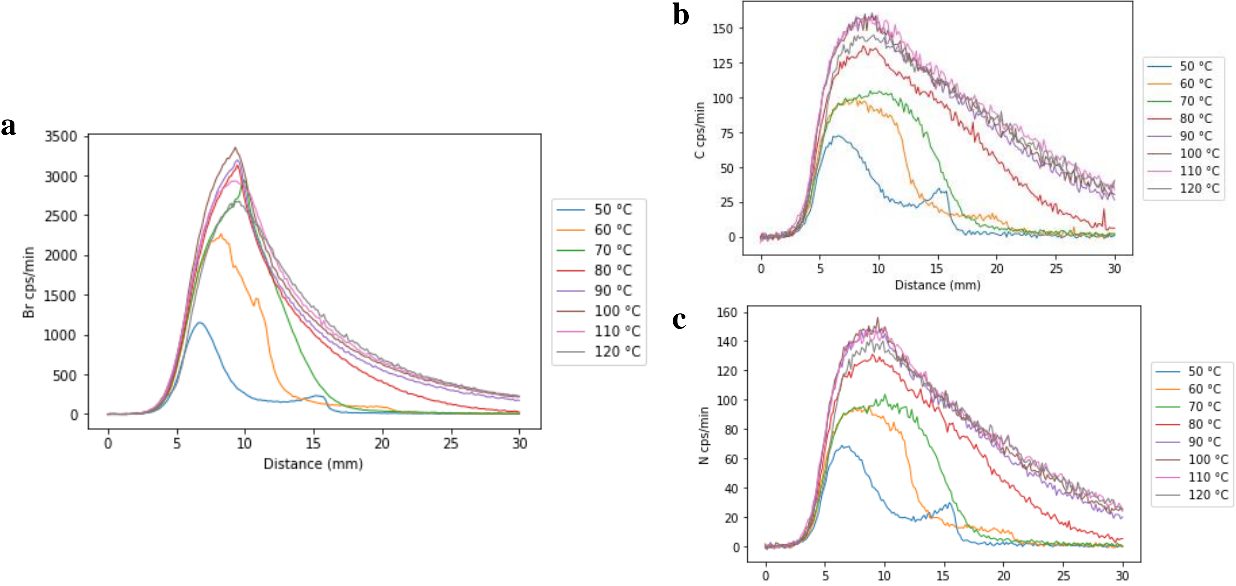

Figure 4-22: a) Shows the EDS intensity profile for Br over 30 mm of the substrate. b) and c) show the EDS intensity profiles for C and N, respectively. The Br data was used to fit the model, because the higher excitation efficiency of Br afforded it a higher signal-to-noise ratio than either C or N. Note the small, satellite peak in the 50 °C curve, which suggests a different growth mechanism than the primary peak.

Figure 4-22 shows the results of the EDS characterization. The Br signal in (a) showed the highest signal-to-noise ratio as Br has a higher X-ray generation efficiency than the lighter elements C and N in (b) and (c), respectively. Strangely, the growth limiting shape of the deposition profile for Br is different than that of C and N, which are similar to themselves. It is unclear what the cause of this difference is. Interestingly, the small satellite peak in the data at 50 °C suggests a L-H type reaction by the peak shape and location relative to the deposition onset. This peak likely shifted towards the main peak and appeared at 12 mm when the deposition temperature increased to 60 °C. This is consistent with a L-H type reaction upon an increase in temperature for this deposition chemistry.

The integral of the Br EDS signals (Figure 4-23) also comported with previous attempts to measure the transition temperature between reaction rate and mass-transport limited growth via profilometry and mass measurements. The results indicate a possible transition temperature between 90—100 °C, which compared favorably with the previous results. Interesting to note is the downturn in the signal at 120 °C. A small downturn was also observed in Figure 4-17b at 130 °C. The cause of this is not currently understood, but simulations suggest that a greater rate of desorption leading to a reduction in R-E and L-H type reactions can play an important role.

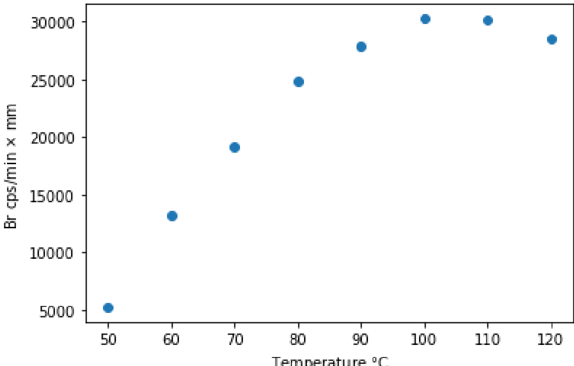

Figure 4-23: Integral of the Br EDS intensity data in Figure 4-22. The data clearly show a plateauing beginning around 100 °C and a possible reduction in growth rate at 120 °C.

4.3.3.2 $SnBr_2$ EDS

The $SnBr_2$ EDS signals shown in Figure 4-24a-d (offset for clarity) indicated that the width of the deposition increased more dramatically than the localized deposition rate as the temperature increased. This is different than in MABr depositions where the growth rate increased everywhere up to saturation. As the temperature increased, the front edge of the deposition shifted closer to the center of the reactor just as the extent of the sample increased, which moved the tail end of the deposition further away from the reactor center. This is shown in three example depositions of increasing temperature in Figure 4-25.

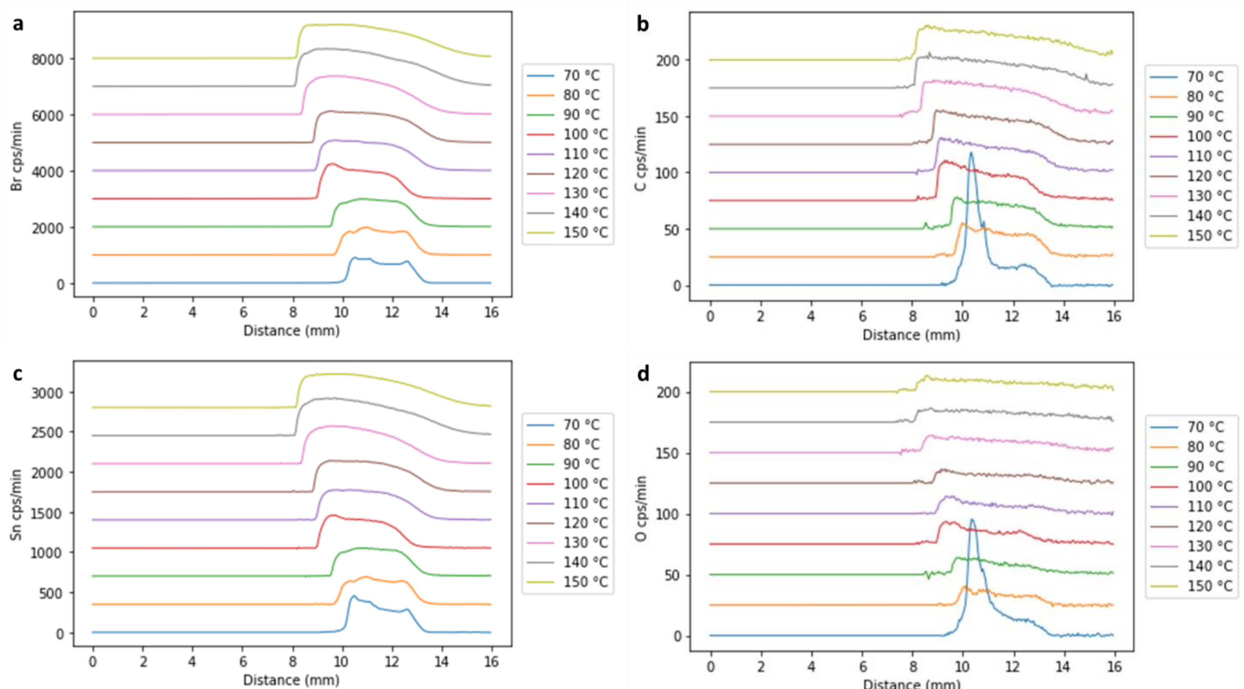

Figure 4-24: EDS intensity signals for $SnBr_2$ samples prepared with 0.4 sccm HBr and 0.05 sccm $Sn(acac)_2$ at temperatures between 70—150 °C.

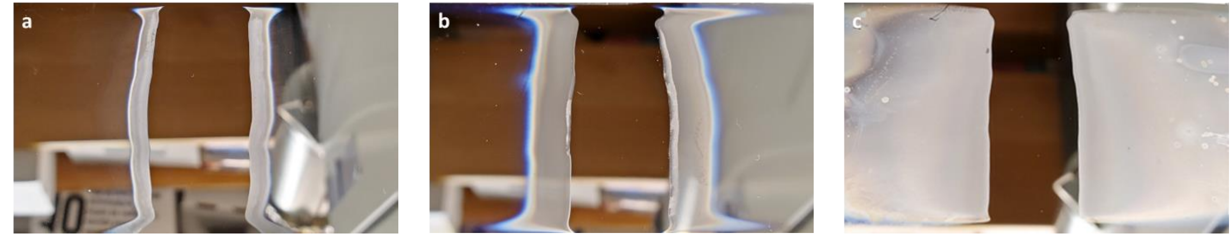

Figure 4-25: (a-c) Optical images of three $SnBr_2$ depositions with (b) deposited at a hotter temperature than (a), and (c) deposited at a hotter temperature than (b). These images agree with the spreading of the deposition width as shown in Figure 4-24.

As the temperature increased, the slope of the Br signal after the initial rise began to straighten into a linear decrease with distance in the direction of the gas flow (away from the origin). This was more clearly seen at even higher temperature in Figure 4-26. One hypothesis for this behavior was the reaction rate had become mass transport limited at the higher temperatures, so the growth rate was dominated by the diffusion of the precursors (or gas phase products) to the surface. Diffusion is considerably slower than advection, which in the limit of negligible diffusion

and very high gas flows (a very high Péclet number), would produce a strongly linear deposition profile.

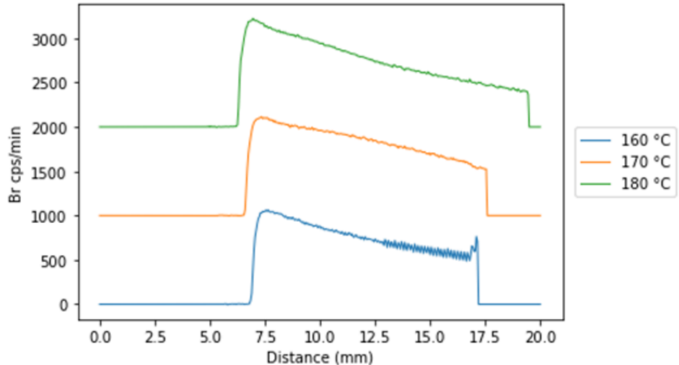

Figure 4-26: Br EDS intensity signals from a $SnBr_2$ sample deposited with 0.4 sccm HBr and 0.05 sccm $Sn(acac)_2$ at temperatures 160, 170, and 180 °C.

One issue that arose when performing EDS measurements of $SnBr_2$ deposited on Si was the phenomenon of "pulse pileup". This occurs when the intensity of the X-ray signal is strong enough that two X-rays trigger the detector within the processing time with the detector failing to record them as separate peaks. Instead, the detector sums the energies and records a new peak at the energy sum. Coincidentally, Si has a peak at 1.74 keV and Sn has a peak at 3.44 keV, which will cause any Si pulse pileup to be recorded as a Sn peak. This artifact can be reduced or eliminated by using shorter processing times or by post-process removal. The artificial Sn peaks were removed from this work's EDS samples by calibrating a 4th order polynomial transfer function using a bare Si substrate as the standard. The calibration data is shown in Figure 4-27a. In this experiment, a base Si substrate was exposed to varying electron beam currents and the spectra of C, O, Si, Br, and Sn were collected at each current. Assuming no contribution from *actual* elements on the surface or subsurface of the Si wafer, the counts represented artificial

counts, and in the case of Sn, pulse pileups from the Si substrate. All subsequent EDS $SnBr_2$ spectra for Sn had this artificial Sn signal removed using the calibration.

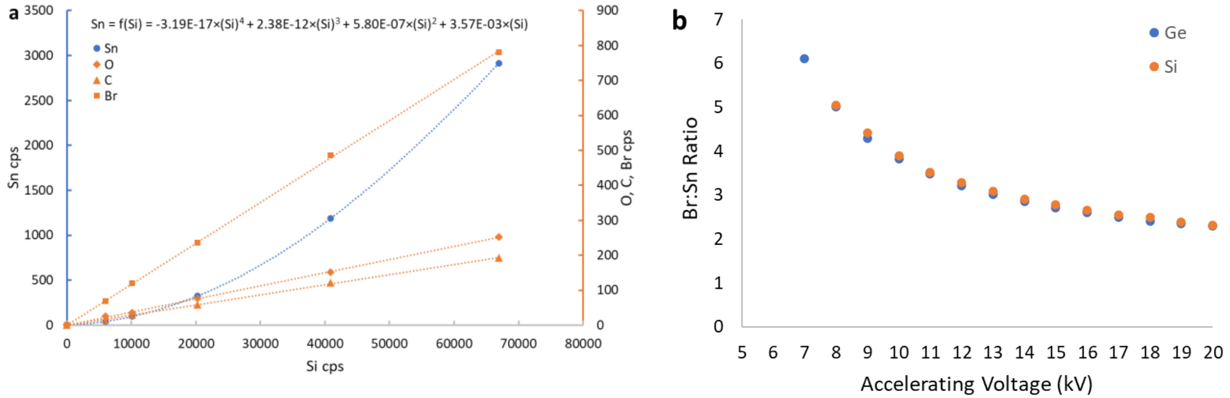

Figure 4-27: (a) Calibration of the artificial Sn peaks from pulse pileup when detecting Si at high intensity. The measurements were conducted on a bare Si wafer at 12 keV with a 10 mm working distance. The different Si intensities were obtained by varying the electron beam current. Note the stark difference in shape and artificial counts between Si and the other elements. A 4th order polynomial was fit to the Sn curve to estimate the number artificial Sn peaks to remove based on the local Si count. (b) The ratio of Br:Sn EDS intensities were compared at different electron accelerating voltages on Ge and Si wafers to determine if the Si emission at 1.74 keV caused a secondary emission from Br at 1.48 keV. This could manifest as a change in the Br:Sn ratio as more of the Si substrate was detected. Fortunately, there appeared to be little response from Br due to the X-ray response from Si.

Another potential issue was whether emission from Si at 1.74 keV would be scattered by Br and cause emission at 1.48 keV. The variation in the sample thickness would cause a variation in the penetration depth of the electrons, and thus, a variation in the emission of X-rays from Si. If it were true that the X-ray emissions from Si were scattered by Br with subsequent emission of a characteristic Br X-ray, then this would change the detection efficiency of Br vs Sn (3.44 keV) as the sample thickness changed. To confirm this, a $SnBr_2$ sample was deposited on Ge (1.188 keV) and Si, and the Br:Sn ratio of EDS intensities were recorded at different electron beam penetration depths by varying the accelerating voltage. Fortunately, there appeared to be no strong emission

from Br due to the characteristic Si X-rays as evident in the near overlapping Br:Sn ratios for Si and Ge substrates of Figure 4-27b. The increase in the ratio at lower accelerating voltages was due to the more greatly reduced scattering efficiency of Sn at these lower electron energies.

4.4 Impurity Analysis

Unlike MABr, $SnBr_2$ is not formed from a single addition reaction. Instead, it proceeds in two steps – 1) protonation and exchange of the first $Acac^-$ ligand with Br^- from an HBr molecule; 2) a second protonation and exchange of the remaining $Acac^-$ anion with Br^- from a second HBr molecule. This reaction scheme is shown in reactions (4-2) and (4-3). The intermediary in this process – Sn(acac)Br – may enter the film and increase the background impurity if the concentration of HBr and/or the mixing of HBr and $Sn(acac)_2$ is insufficient during the residence time in the reactor.

+ HBr (4-2)

+ HBr (4-3)

From the previous XPS and EDS analyses for the $SnBr_2$ depositions, the films contained some carbon and oxygen, which suggested that potentially some free ligand or $Acac^-$ anion was trapped in the film. To test this hypothesis, EDS, FTIR, and Raman analyses of the $SnBr_2$ films were performed.

4.4.1 $SnBr_2$ EDS Impurity Analysis

Ideally, EDS quantification with a standard would be able to provide compositional accuracy to $\pm 2\%$.[2] However, the measured "compositions" were exceedingly off the expected values, sometimes suggesting compositions of $SnBr_3$. Most notable among the many sources of possible errors was the irregular geometry of the surface (see Figure 4-13). However, because the scattering efficiency of C and O may be considered similar given their proximity on the periodic table, a ratio of their signal counts was predicted to contain useful information regarding their elemental ratios.

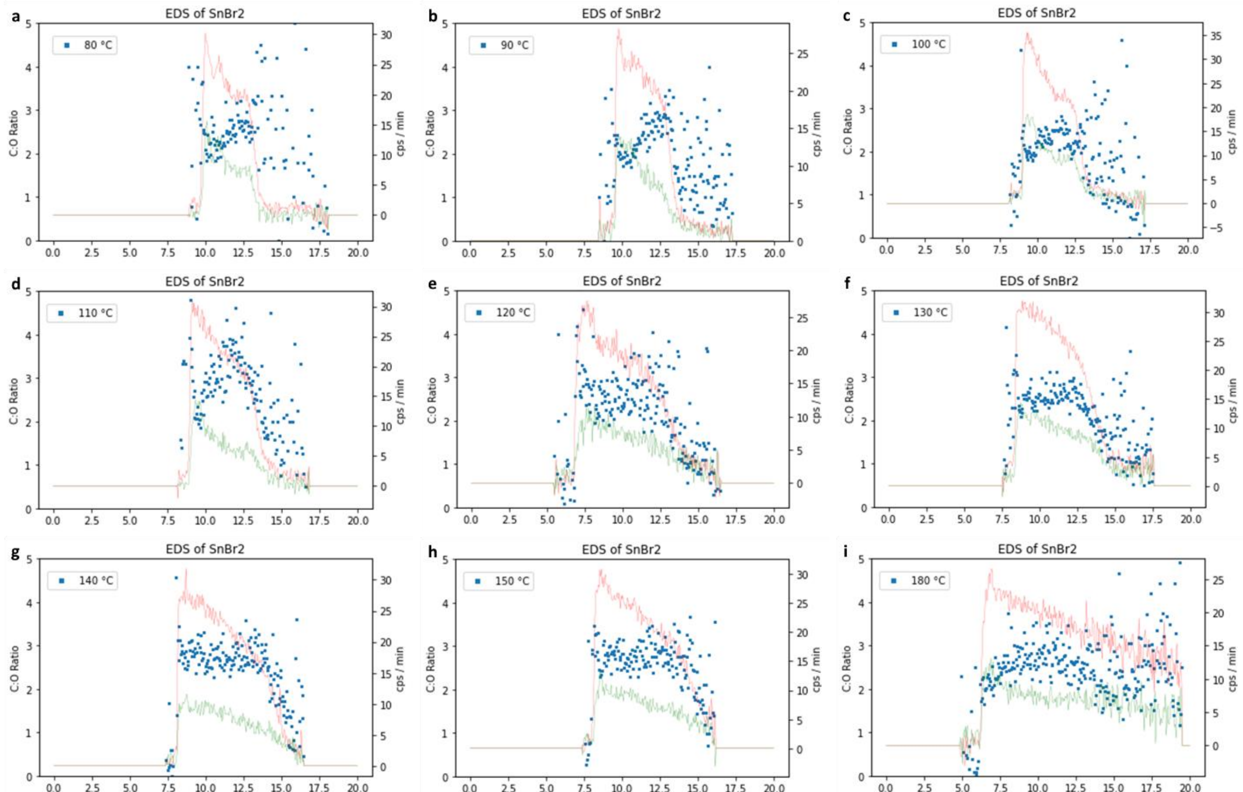

Figure 4-28: (a-i) C and O EDS signals on the right axis and their ratio on the left axis. The data was collected from $SnBr_2$ depositions made with 0.4 sccm of HBr and 0.05 sccm of $Sn(acac)_2$ between temperatures of 80—180 °C. Notably, the ratio of C:O is near 2.5, the ratio of C to O in acetylacetone and the acetylacetonate anion ($Acac^-$). The abscissa is the distance, measured in millimeters, from the center of the reactor.

When this ratio was plotted for several $SnBr_2$ samples characterized by EDS, a clear trend showed an average ratio very near 2.5 for C:O, which is the ratio of C to O in the free, protonated ligand acetylacetone (H(acac)) and the acetylacetonate anion ($Acac^-$). The variation away from a ratio of 2.5 could be due to additional SnO_2 caused by post-deposition oxidation in air or additional carbon contamination from the environment. These results, while not conclusive, supported the hypothesis that the measured C and O in the film were not random, atomic impurities but could potentially be assigned to specific molecules, which then could be included in defining and fitting a CVD model.

To measure the extent of oxidation post-deposition after the film had quickly cooled to room temperature, a $SnBr_2$ film was analyzed by EDS multiple times after three different timed delays from when the sample was first removed from the reactor. The results of this experiment, shown in Figure 4-29 suggest that most of the oxidation of Sn occurred during retrieval from the reactor while the film was still above room temperature or during the residence in the reactor.

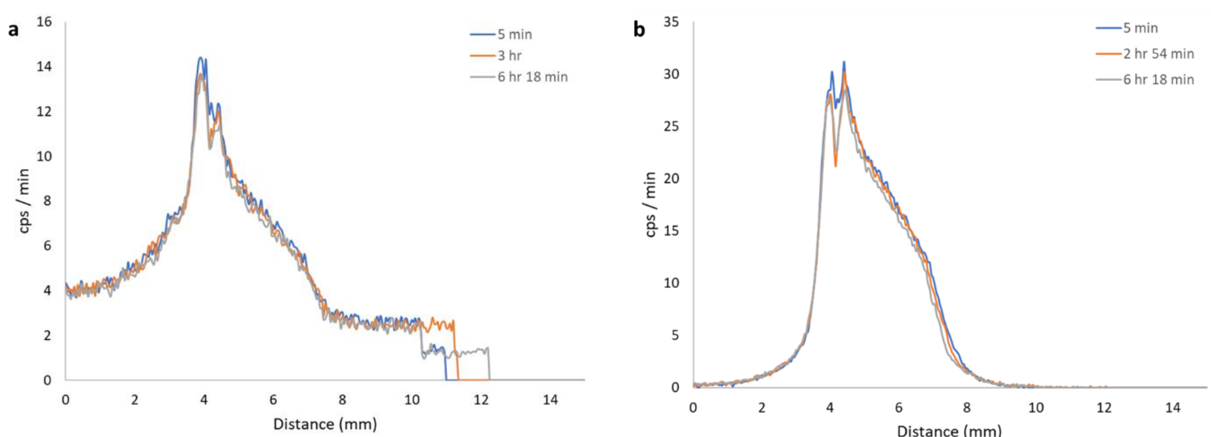

Figure 4-29: EDS results of an oxidation study on a $SnBr_2$ sample deposited at 80 °C with 0.025 sccm of $Sn(acac)_2$ and 0.17 sccm of HBr. The EDS intensity data were collected after waiting the 5 min, 3 hrs, and 6 hrs 18 min after removal from the reactor. The signal difference between the different time points suggested a loss of Br of approximately 1% per hour when left in air. The Sn signal showed negligible loss. Note, the Sn signal was not corrected for artificial Sn peaks caused by the Si substrate. This sample was made with the Gen 1 reactor.

4.4.2 $SnBr_2$ ATR-FTIR Analysis

To attempt to identify the molecular origins of the C and O impurities in the $SnBr_2$ depositions, Attenuated Total Reflection Fourier Transform Infrared Spectroscopy (ATR-FTIR) measurements were performed. ATR-FTIR works by measuring the spectral dependence of the energy lost in the evanescent waves that extend 0.5—5 μm from the surface of a polished crystal when a sample is in intimate contact.[5] The ATR-FTIR used in this work was a Thermo Fisher Scientific Nicolet iS50 ATR-FTIR with a diamond crystal operated in the Far-IR range (100-1800

cm^{-1}). Because the greatest C and O signal strength in the $SnBr_2$ deposition series came from films deposited at 70 °C (see Figure 4-24), the sample prepared for ATR-FTIR was deposited at 70 °C with 0.084 sccm of HBr and 0.025 sccm of $Sn(acac)_2$ for 15 min on a Si substrate.

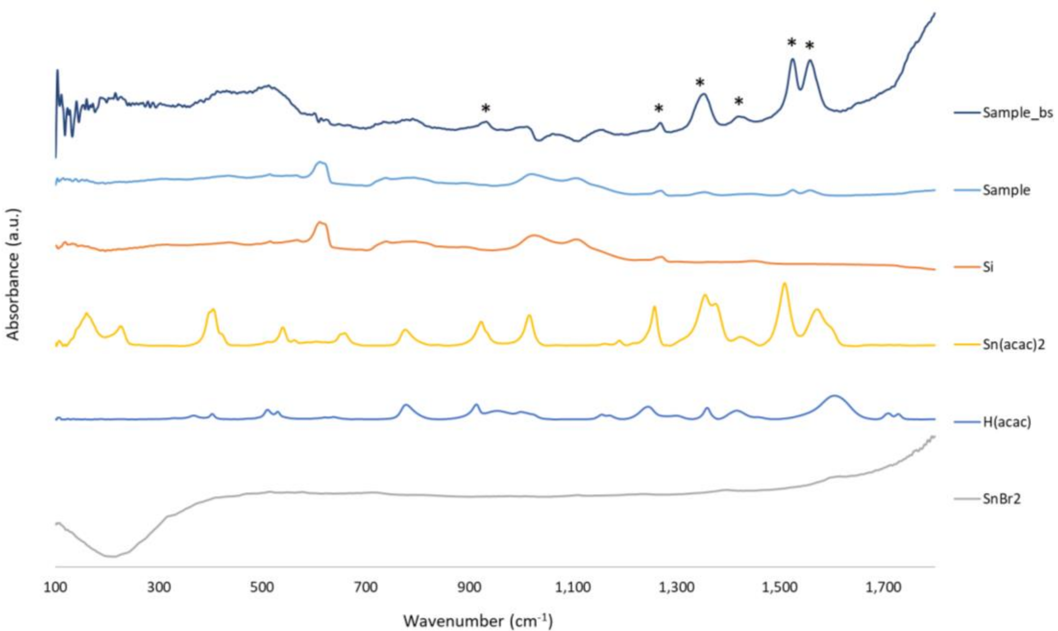

Figure 4-30: ATR-FTIR absorption data of a $SnBr_2$ film and several standards for comparison. The * indicate peaks in the absorption spectra of the sample with the Si background subtracted (Sample_bs) that best match the absorption peaks of $Sn(acac)_2$ (99%, Sigma Aldrich). Some peaks from H(acac) (99%, Beantown Chemical) also match the sample, but they overlap with the $Sn(acac)_2$. The strong rise in the peak near 100 cm^{-1} is due to $SnBr_2$.

The results of the ATR-FTIR analysis of the $SnBr_2$ sample and those of several relevant standards are presented in Figure 4-30. The sample showed a strong signal from the Si substrate that greatly dominated the response. However, if the response of the Si substrate was subtracted and the difference was magnified, the spectrum showed several peaks (*) in the FAR-IR region between approximately 300-700 cm^{-1} that strongly match the $Sn(acac)_2$ standard. It is possible that there is a mixture of contributions from Acac$^-$ anions and free H(acac) molecules in the film, but the absence of the dominant peak in H(acac) at 300 cm^{-1} suggested that H(acac), if present, was

less abundant than $Acac^-$. This hypothesis is also consistent with H(acac) being easily removed from the film at 70 °C given its vapor pressure is estimated to be greater than the concentration of generated H(acac) (boiling point is near 140 °C).

4.4.3 $SnBr_2$ Raman Analysis

To complement the ATR-FTIR results and further test the hypothesis that C and O impurities in the $SnBr_2$ films resulted from $Sn(acac)_2$, SnBr(acac), SnO, SnO_2, or H(acac) molecules, Raman Spectroscopy was performed. Raman Spectroscopy is a non-destructive chemical analysis technique that measures low-frequency modes of molecule vibration. These modes of vibration are detected from inelastically scattered light because of changes in the molecules' polarizability. In this work, a Horiba XploRA Plus Raman Spectrometer equipped with a 785 nm laser at 10.4 mW was used in brightfield mode with a collection time of 20 min and 2 accumulations (to filter out cosmic ray spikes).

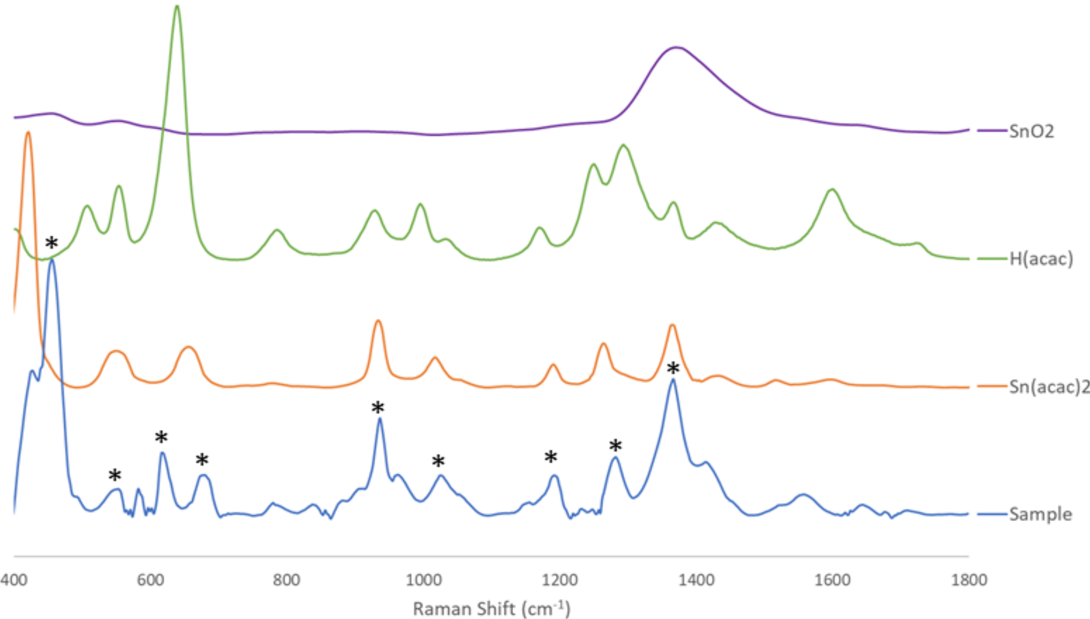

Figure 4-31: 785 nm brightfield Raman data for a $SnBr_2$ sample and several relevant standards. The * peaks in the sample correspond closely to $Sn(acac)_2$ and, to a lesser extent, H(acac). This data strongly suggests the preponderance of C in the film may be associated with unprotonated $Acac^-$ ligands. The broad SnO_2 peak is also observed in the sample. Whether SnO_x is formed *in-situ* or *ex-situ* immediately upon air-exposure is unclear.

Figure 4-31 shows the results of this measurement and those for several relevant standards. After the fluorescent background was subtracted via a polynomial fit, the sample peaks were clearly seen to align with the $Sn(acac)_2$ and H(acac) standards. The strong sample peak near 450 cm^{-1} was expected originate from the strong $Sn(acac)_2$ signal near 400 cm^{-1}. A similar peak closer to 450 cm^{-1} was observed for $Fe(acac)_3$ (data not shown), so it was inferred that the 450 cm^{-1} peak correlated with the strong $Sn(acac)_2$ peak near 400 cm^{-1}. The $SnBr_2$ signal was virtually silent in this spectral window and was not shown. The only conclusive evidence of H(acac) in the sample occurred near the 620 cm^{-1} peak where H(acac) has its strongest response. Altogether, this suggests that the majority of C in the sample (other than adventitious carbon) can be assigned to unprotonated $Acac^-$ ligands. The broad SnO_2 peak is also observed in the film near 1400 cm^{-1}. It is unclear if SnO_x is formed *in-situ* or *ex-situ* as the samples were removed from the reactor while

hot into the open air before quickly being shuttled into a N_2 rich environment in the glovebox. This brief time could add significant oxidation to the films.

4.5 Conclusion

The results presented in this chapter aimed to characterize the MABr and $SnBr_2$ films for elemental composition, morphology, crystallinity, and impurities. XRD was used to verify that the deposition processes were successful in depositing both MABr and $SnBr_2$. XPS results supported this result by identifying stoichiometric ratios of C, N, and Br for MABr formation within the expected error of the XPS instrument. However, XPS results for $SnBr_2$ were complicated by the gradually loss of Br due to the impact of etching. Despite this, the initial results during the depth profiling suggested a 2:1 ratio of Br with surface carbon and 2.5% SnO_2. SEM and EDS results were used to characterize the morphology of the surface and define the spatial extent of the deposition profile for both MABr and $SnBr_2$. $SnBr_2$ suffered from rapid crystallization, which compelled a reduction in deposition time and precursor concentration to avoid generating severely rough films. Finally, EDS, FTIR, and Raman were used to identify the most plausible origins of the C and O contamination in the film.

4.6 References

1. PDF 10-0699, www.icdd.com
2. PDF 72-1088, https://icsd.products.fiz-karlsruhe.de/
3. Ke, W. *et al.* Enhanced photovoltaic performance and stability with a new type of hollow 3D perovskite {en}FASnI $_3$. *Sci. Adv.* **3**, e1701293 (2017).

4. Newbury, D. E. & Ritchie, N. W. M. Performing elemental microanalysis with high accuracy and high precision by scanning electron microscopy/silicon drift detector energy-dispersive X-ray spectrometry (SEM/SDD-EDS). *J Mater Sci* **50**, 493–518 (2015).

5. Pike Technologies. ATR Theory and Applications. (Madison, WI 2022)

6. Thompson, T. Fundamentals of Raman Spectroscopy. *Laser Focus World* (Accessed: May 2022)

5 Modeling of MABr Depositions

5.1 Motivation

Modeling chemical reactions provides a means to both understanding the underlying mechanisms of a reaction – qualitatively and quantitatively – and the ability to harness this knowledge to optimize the reaction process. This is especially useful in attempting to deposit perovskites by a ternary APCVD process. In such a process, 10+ reaction mechanisms could occur simultaneously, greatly confounding a chemist's ability to predict which conditions best optimize the deposition rate, film quality, etc. However, modeling each step of the process by separately examining the depositions of MABr and $SnBr_2$ can help distill the entire process into understandable pieces.

This chapter discusses efforts to this effect and presents qualitative estimates of the important reaction mechanisms involved in the depositions of MABr films. Modeling $SnBr_2$ was not possible within the timeframe of this thesis and was left as future work. Br EDS linescans of deposited films were compared with simulations of mass deposition rates to make mechanistic determinations. DFT and CCSD(T) *ab-initio* methods were also used to provide initial estimates to activation energy barriers.

5.2 CVD Modeling Framework

5.2.1 Classical Kinetic Theory

CVD simulations have been previously performed for a number of thin films including SnO_2[1,2] and Si.[3] Simulating CVD reactions in a CFD model involves determining the kinetics of the relevant reactions. The rate of mass change of a species i is calculated according to Equation (5-1)

$$\dot{m}_i = M_i \sum_{r=1}^{n} R_{r,i} \tag{5-1}$$

where $\dot{m}_i$ is the rate of mass change of species i, M_i is the molecular weight of species i, and $R_{r,i}$ is the molar rate of creation/destruction of species i according to reaction R_r for all n possible reactions.[2] Such reactions were modeled both in the gas phase and at the substrate. Assuming negligible effects of third-bodies on the reactions (i.e. restricting to bimolecular reactions only) and negligible reverse reactions, the molar rate of change of species i in reaction R_r was modeled with an Arrhenius type model according to Equation (5-2)

$$R_r = \nu \alpha e^{-\frac{\Delta E_a}{k_B T}} \tag{5-2}$$

where ν is a pre-exponential factor that describes the frequency of collisions (i.e. reaction attempts), T is the temperature, α includes stereodynamic effects on the reaction (e.g. sticking

coefficient in adsorption simulations, dynamics of gas phase reactions involving anisotropic molecular geometries), and E_a is the activation energy barrier (strictly positive). For gas phase reactions, ν_{gas} is directly proportional to the concentrations of the reactants, area swept out by their motion, and the speed of the A, B system center of mass. The form of ν can be derived from kinetic theory[5,6] and is assumed to be

$$\nu_{gas} = [A][B]\sigma_{AB}^2\sqrt{\frac{8\pi k_B T}{\mu_{AB}}} \tag{5-3}$$

where [A], [B] are the molar concentrations of species A, B, σ_{AB} is the molecular diameter of A + B and μ_{AB} is the reduced mass of system A, B. This model for gas phase CVD reactions assumes ideal gas behavior and only binary collisions occur (no third-body effects).

For surface-gas reactions (Rideal-Eley mechanism – R-E), the form of ν depends on the flux of species A coming to the surface from the gas phase and interacting with an adsorbed species B_s. Therefore, ν_{R-E} was assumed to take the form of Equation (5-4)

$$\nu_{R-E} = \left[\frac{p_{atm}}{\sqrt{2\pi m_A k_B T}}\frac{T}{273}\frac{[A]}{n_0}\right] \times \left[\frac{[B_s]}{n_s}\right] \tag{5-4}$$

where p_{atm} is the atmospheric pressure in S.I. units, m_A is the molecular mass of species A, n_0 is the molar density at standard temperature and pressure (STP), $[B_s]$ is the surface density of B, and n_s is the total surface site density for B. The assumptions in the R-E model include the surface site density for species B is independent of temperature, only a monolayer coverage (Langmuir

assumption), N_2 adsorption/desorption is sufficiently fast or insignificant to meaningfully affect surface coverage, and only binary reactions. The independence of the surface site density with temperature can be expected to hold only in the temperature range where the surface roughness remains relatively constant. Other models allow a variable surface area with temperature, but this was not pursued in this thesis.

For surface-surface reactions (Langmuir-Hinshelwood mechanism – L-H), the form of ν depends on the density of adsorbed surface species A_s, B_s, the diameter of the combined molecule $A + B$, and the surface velocity of the A, B system center of mass according to Equation (5-5)

$$\nu_{L-H} = [A_s][B_s]\sigma_{AB}\sqrt{\frac{\pi k_B T}{2\mu_{AB}}} \tag{5-5}$$

where $[A_s]$ is the surface site density of species A. The assumptions in the Langmuir-Hinshelwood reaction include that the adsorbed species behave as a 2D ideal gas and only binary collisions occur. The assumption of a 2D ideal gas certainly fails for strongly chemisorbed species at low temperatures but is more accurate for adsorbed species at higher temperatures where the activation barrier to diffusion is easily overcome with thermal energy.

Adsorption and desorption were modeled assuming only an attractive potential as demonstrated in Figure 5-1.

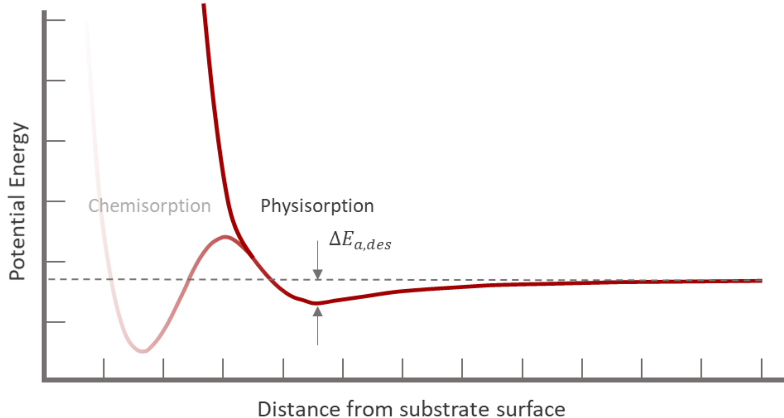

Figure 5-1: Model potential energy curve for a molecule approaching a surface. The CVD model employed in this thesis assumed reversable adsorption of gas phase molecules without an activation barrier to adsorption, unlike chemisorption. Chemisorption was modeled through Rideal-Eley reactions as previously defined.

Adsorption was modeled assuming a barrierless reaction ($\Delta E_a = 0$) between a gas phase species near the surface and an open-site, θ_s, for adsorption. The open-site density was assumed to be unaffected by temperature or N_2. The form of ν_{ads} for adsorption of species A was modeled as Equation (5-6)

$$\nu_{ads} = \left[\frac{p_{atm}}{\sqrt{2\pi m_A k_B T}} \frac{T}{273} \frac{[A]}{n_0}\right] \times \left[\frac{[\theta_s]}{n_s}\right] \tag{5-6}$$

where $[\theta_s]$ is the concentration of open-sites, n_s is the density of total surface sites, and p_{atm}, m_A, T, and n_0 are atmospheric pressure, molecular mass of species A, the temperature, and the ideal gas density at STP, respectively.

Desorption was modeled assuming a pre-exponential factor proportional to the adsorbed species concentration and a typical lattice vibration frequency – on the order of 10^{13} s^{-1}.[7] In this

model, the "attempt" frequency of desorption is assumed to originate from the thermal energy of the lattice. The form of v_{des} is shown in Equation (5-7)

$$\nu_{des} = f_{lat}[A_s] \tag{5-7}$$

where f_{lat} is the lattice vibration frequency and $[A_s]$ is the adsorbed species concentration for species A.

The overall reaction rates for the various reaction mechanisms are listed in Table 5-1.

Table 5-1:	Model Reaction Equation
Bimolecular gas phase reaction	$R = \alpha\sigma_{AB}^2 \sqrt{\frac{8\pi k_B}{\mu_{AB}}} \times T^{0.5} e^{-\frac{E_a}{k_B T}}[A][B]$
Rideal-Eley gas-to-surface reaction	$R = \frac{\alpha p_{atm}}{273 n_0 n_s \sqrt{2\pi m_A k_B}} \times T^{0.5} e^{-\frac{E_a}{k_B T}} [A][B_s]$
Langmuir-Hinshelwood surface reaction	$R = \sigma_{AB} \sqrt{\frac{\pi k_B}{2\mu_{AB}}} \times T^{0.5} e^{-\frac{E_a}{k_B T}} [A_s][B_s]$
Adsorption	$R = \frac{p_{atm}}{273 n_0 n_s \sqrt{2\pi m_A k_B}} \times T^{0.5}[A][\theta_s]$
Desorption	$R = f_{lat} \times e^{-\frac{E_{des}}{k_B T}}[A_s]$

5.2.2 *Ab-initio* Estimates of Activation Energy Barriers

To estimate the activation energy barriers for the four types of reaction mechanisms presented in Table 5-1 (assuming adsorption is barrier-less), density functional theory (DFT) and coupled cluster theory with singles, doubles and approximate triples (CCSD(T)) *ab-initio* methods were used. DFT,[6] in particular Kohn-Sham DFT, takes advantage of the Hohenberg-Kohn theorem

– that the ground state energy of a system is uniquely determined by the electron density – to replace an intractable problem of solving the Schrodinger equation for many, interacting electrons with a "fictitious" system of non-interacting electrons described by an electron density. In this framework, the exchange and correlational terms, as well as the external potential, can all be described using "functionals" – functions of the electron density. Coupled cluster theory,[9] instead, attempts to solve the actual Schrodinger wavefunction and uses an exponential ansatz for the correlation operators. The accuracy of this theory depends heavily on how many terms in the Taylor expansion of the exponential operator are used. In CCSD(T), the expansion is included to the second order and the third order term is approximated. For the purposes of this thesis, both DFT and CCSD(T) calculations were carried out using the Orca software package.[10]

To estimate the gas phase reaction activation energy, the Orca software package was used, and in particular, the Nudge-Elastic Band Transition State search algorithm (NEB-TS). The details of this algorithm may be found elsewhere.[11,12] The activation energies for the gas phase reactions in this thesis were assumed to be equal to a single minimum transition state energy where the transition state was located on a saddle-point on the potential energy surface between the products and reactants for the respective reaction. To use NEB-TS, the reactants and product geometries were first optimized using a range-separated hybrid functional from Head-Gordon with a nonlocal dispersion correction.[13] The geometries were first optimized using the PBE0 functional and a triple-ζ doubly polarized basis set for all elements except bromine, which used the minimally augmented version to account for diffuse electrons on the anion. The geometry was then further optimized using the conditions in Table 5-2. The final single point energies were evaluated using the Domain-based Local Pair Natural Orbital (DLPNO) approximation to CCSD(T), which results in near linear scaling and captures approximately 99% of the correlation energy.[12] Table 5-3 shows

the values for the final energy calculations and that MABr has an enthalpy of formation of -45 kJ/mol.

Table 5-2: **MABr**

		Reactants	Transition State	Products
Geometry Optimization	Method	DFT wB97x-V	DFT wB97x-V, NEB-TS	DFT wB97x-V
	Basis Set	H, C, N: ZORA-def2-QZVPP, Br: ma-ZORA-def2-QZVPP	H, C, N: ZORA-def2-TZVPP, Br: ma-ZORA-def2-TZVPP	H, C, N: ZORA-def2-QZVPP, Br: ma-ZORA-def2-QZVPP
	Relativistic Correction	ZORA	ECP	ZORA
	Approximations	RIJCOSX	RIJCOSX	RIJCOSX
Final Energy Calculation	Method	DLPNO-CCSD(T)	-	DLPNO-CCSD(T)
	Basis Set	H, C, N: ZORA-def2-QZVPP, Br: ma-ZORA-def2-QZVPP	-	H, C, N: ZORA-def2-QZVPP, Br: ma-ZORA-def2-QZVPP
	Relativistic Correction	ZORA	-	ZORA
	Approximations	DLPNO, RIJCOSX	-	DLPNO, RIJCOSX

Table 5-3:

HBr	**MA**	**MABr**
-2623.9331 E_H	-95.8032 E_H	-45 kJ/mol Δ

* white – H, red – Br, grey – C, blue – N

The results of the simulations suggested that no transition state exists for the gas-phase reaction of HBr and MA. This was not surprising considering the reaction is a simple acid-base reaction. To further evaluate this conclusion, the potential energy at fixed distances between the acidic proton and nitrogen was estimated with all other atomic coordinates optimized. The wB97x-

v functional was used for the geometry optimization with a def2-TZVPP basis set for all elements except Br, which had an augmented version. The final energies were calculated using the DLPNO approximation to CCSD(T) with a 3/4 basis set extrapolation using the def2 series. The results of this study are presented in Figure 5-2, which confirm no transition state exists.

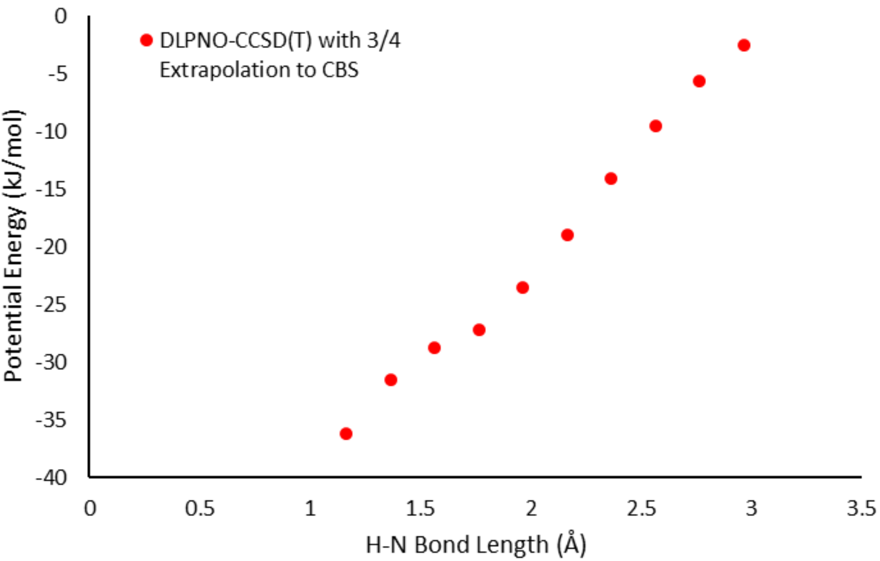

Figure 5-2: Plot of the potential energy of MA interacting with HBr with fixed H-N distances where the H is the acidic proton from HBr. The monotonically decreasing energy with shortening H-N distance further supported the conclusion that no transition state exists between HBr reacting with MA to form the salt MABr. The zero energy was the energy calculated at a H-N separation distance of 3.164 Å.

Desorption activation energy barriers can be predicted by evaluating the interaction energy between an adsorbed species on a surface composed of a finite number of repeating unit cells of the substrate.[13,14] The number of repeating unit cells used in the calculation is a tradeoff between accuracy and computer wall-time/memory. In this work, the (001) plane of a 4x4x1 supercell was exposed with a unit cell consisting of a pair of MABr molecules (Figure 5-3a). The geometry of the adsorbed molecule was optimized using the PBE0 functional with D4 dispersion correction and the def2-TZVPP basis set while the lattice was fixed. The single point energies were calculated

with the wB7x-V functional and the def2-TZVPP basis set. However, because there is a tendency to artificially lower the intermolecular interaction energy due to a basis set superposition error, a counterpoise correction strategy following Boys and Bernardi (1970)[15] was implemented. As shown in Figure 5-3, the energies of desorption were estimated to be -23 kJ/mol and -39 kJ/mol for HBr and MA, respectively.

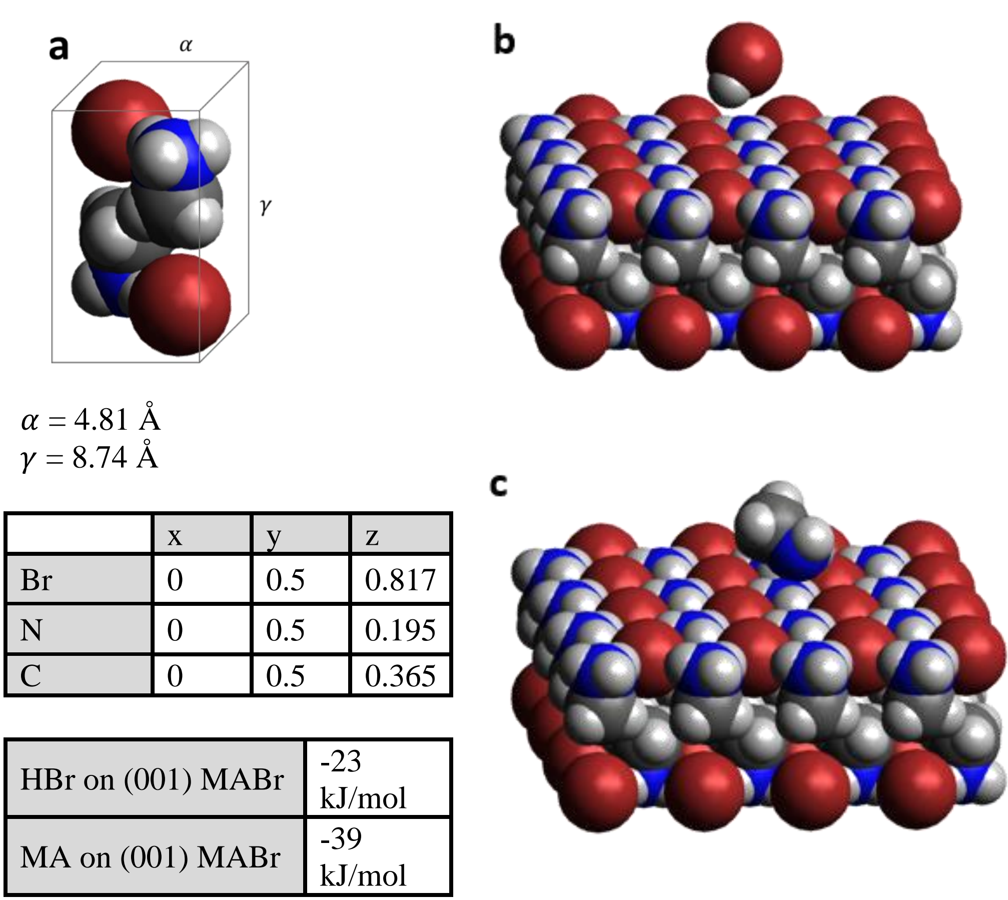

	x	y	z
Br	0	0.5	0.817
N	0	0.5	0.195
C	0	0.5	0.365

HBr on (001) MABr	-23 kJ/mol
MA on (001) MABr	-39 kJ/mol

Figure 5-3: (a) The unit cell for MABr[18] with P4/nmm space group with the axial lengths presented below. The inset table shows the fractional coordinates for one-half of the unit cell molecules. The other has x,y swapped and z inverted. (b) HBr and (c) MA were simulated on a 4x4x1 supercell on the (001) plane. The calculated energies are shown in the second inset table. Note: Br – red, H – white, N – blue, C – grey.

5.2.3 Initial Model Estimates

Diffusion coefficient estimates were implemented in the Ansys Fluent software as a 1-D polynomial fit vs temperature. The coefficients of this line fit were determined by finding the slope and intercept of solutions to either the Chapman-Enskog formula (Chapter 3) or the Fuller Method,[19,20] a semi-empirical approximation to the Chapman-Enskog formula where the interaction potential term Ω is replaced by a sum of elemental volumes determined from linear regression and the 1.5 exponent replaced with 1.75 to account for more realistic interactions than the "hard-sphere" model. For HBr, the ϵ and σ terms to the Chapman-Enskog formula were estimated using viscosity data from the literature.[21,22] Both MA and MABr coefficients were estimated using the Fuller Method.

Assuming all steric factors of unity and using the estimated parameters in Table 5-4 and Table 5-5, the initial model parameters for simulating the fluid flow and CVD reactions of HBr and MA were calculated and are shown in Table 5-6. It was assumed that the Gas-Surface (R-E type) reactions required the adsorbate to break free from any Coulombic or van der Waals forces before the reaction proceeded. Therefore, the activation energy for these reactions was initially assumed to be equal to that of the desorption energies. Likewise for surface (L-H type) reactions, it was assumed the precursors needed to overcome both of their adsorption energies to react. Therefore, this activation energy was assumed to be equal to the sum of the desorption energies. Nitrogen was used as the background carrier gas, and its properties were used as provided in the software.

Table 5-4:

σ_{HBr}	4.45 Å
σ_{MA}	5.40 Å
σ_{N_2}	3.68 Å
n	7.2×10^{-9} kmol/m^2

Table 5-5:	**a0** (m^2/s)	**a1** (m^2/s-K)
HBr	-1.64×10^{-5}	1.02×10^{-7}
MA	-1.76×10^{-5}	1.14×10^{-7}
MABr	-1.28×10^{-5}	8.62×10^{-8}

Table 5-6:		**Frequency Factor**	**Activation Energy (kJ/mol)**
Adsorption	HBr(g)	9.1×10^{8} m^5/(kmol-s)	0
	MA(g)	5.6×10^{8}m^5/(kmol-s)	0
Desorption	HBr(a)	10^{13} m^2/s	23
	MA(a)	10^{13} m^2/s	39
Gas-Phase Reaction	HBr(g) – MA(g)	1.41×10^{10} m^6/(kmol-s)	0
Deposition Rate	MABr(g)	3.4 m^3/s	0
Gas-Surface Reaction	HBr(a) – MA(g)	9.1×10^{8} m^5/(kmol-s)	23
	HBr(g) – MA(a)	5.6×10^{8} m^5/(kmol-s)	39
Surface Reaction	HBr(a) – MA(a)	2.28×10^{18} m^4/(kmol-s)	62

5.3 EDS Training Sets

To train the simulation models, EDS data for different temperature series was collected, as shown in Table 5-4. The different data sets were distinct in the relative ratio of precursor concentrations. This was intended to force different reaction mechanisms to predominate in one series over the other. If a single reaction mechanism was known to dominate the shape of the deposition profile, and if each mechanism could be isolated and modeled in turn, it was hypothesized that any deposition could be deconvoluted into its mechanistic parts.

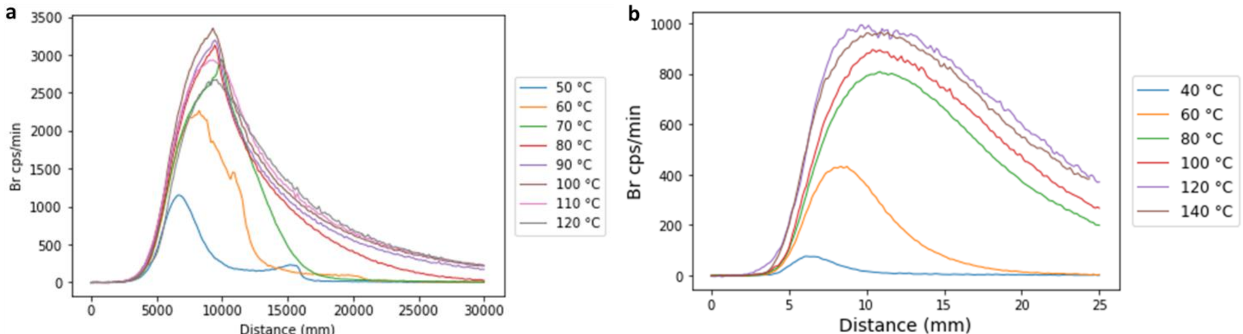

Figure 5-4: (a) EDS intensity plot of MABr deposited with flow rates of 0.45 sccm HBr for all temperatures and 0.26 sccm MA for temperatures 50—60 °C and 0.13 sccm for 70—120 °C. (b) EDS intensity plot of MABr deposited with flow rates of 0.12 sccm HBr and 0.89 sccm MA for all temperatures.

5.4 CFD/CVD Simulation Results

5.4.1 Absence of Gas Phase Reactivity

Despite the assumption that MA and HBr would easily react in the gas phase, there was little evidence this occurred. This was surprising given that the CCSD(T) calculations predicted zero required activation energy, that the chemical accuracy of the CCSD(T) method is purported to be near 4 kJ/mol, and that the gas phase reaction of two simple molecules would seem to be *perfect* for *ab-initio* QM analysis. To further confirm the absence of a gas phase reaction, the 40 °C data in Figure 5-4b was compared against 100 simulations with varying Arrhenius rate constants for a gas phase reaction. All other reaction mechanisms were suppressed, and the diffusion coefficients of Table 5-5 were used. The results are shown in Figure 5-5a with a conversion factor applied to the EDS data. The conversion factor assumed the maximum EDS intensity in Table 5-4b corresponded to the maximum intensity observed in the simulations. Interestingly, the simulation results do not even qualitatively agree with the data. To further clarify

this difference, the peak location and full-width-half-maximum (fwhm) of 200 additional simulations at 60 and 80 °C (100 each) were plotted along with the dataset in Figure 5-4b. The results, shown in Figure 5-5b, indicate that none of the 40, 60 or 80 °C data can be fitted by a gas phase reaction. The solid colors indicate the reactor temperature simulated, and the colors' shading indicate simulations with different Arrhenius parameters at the same temperature.

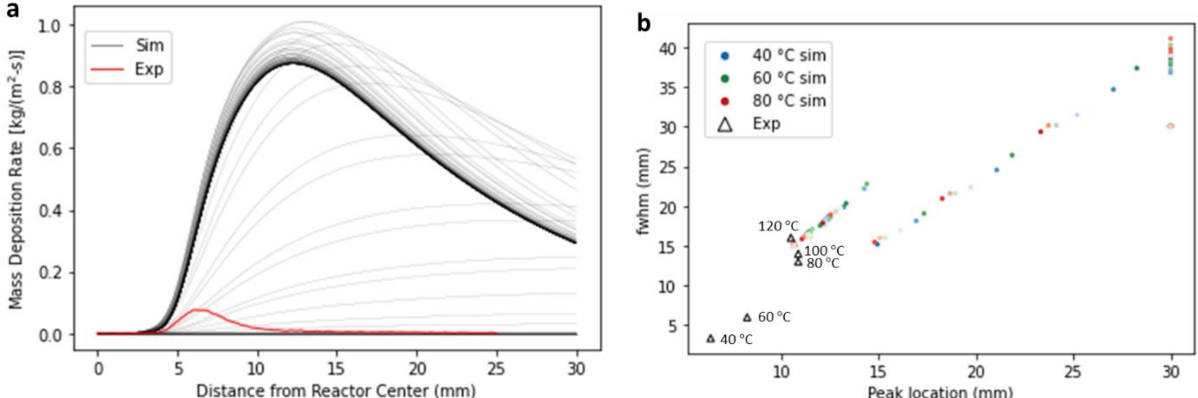

Figure 5-5: (a) EDS data for a MABr deposition at 40 °C plotted alongside simulations assuming a purely gas phase reaction. The complete absence of similarity between the two strongly suggests that gas phase reactions are insignificant at that temperature range. (b) Plots of the peak location vs fwhm of the simulations and dataset of Figure 5-4b indicate zero correlation between the simulations at 40, 60, and 80 °C and the simulations for these two characteristic parameters.

However, the deposition at 120 °C in Figure 5-5b does appear to show some overlap with the simulation data. Supposing that gas phase reactions may contribute significantly at 120 °C or above, 208 simulations with varying diffusion coefficients and Arrhenius rate parameters for a gas phase reaction were performed and compared against this 120 °C data. The results, as shown in Figure 5-6a, suggest that gas phase reactions could affect the total deposition rate at this temperature.

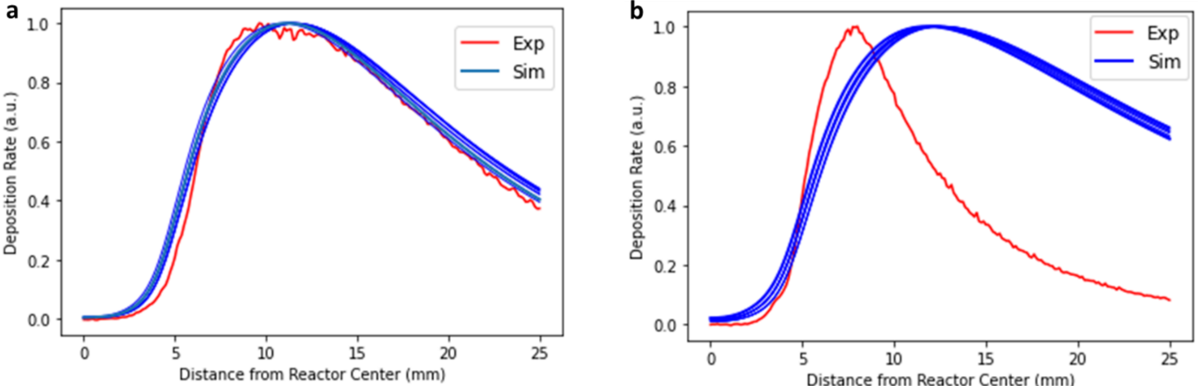

Figure 5-6: (a) 10 simulations ranked by least-squares deviations from the 120 °C experimental data from Figure 5-4b. (b) Using the same Arrhenius parameters and diffusion coefficients as in (a) but with the precursor flow rates of Figure 5-4a, the simulations fail to capture the deposition trend. The ordinate axis values were normalized by their respective peak value, assuming the reaction rate was diffusion limited in each case.

To test the hypothesis that gas phase reactions required a higher than expected temperature to be "activated," the 10 best performing simulations out of the 208 (shown in Figure 5-6a) were re-run with updated precursor flow rates to match the 120 °C deposition conditions in Figure 5-4a. The results in Figure 5-6b, again, do not match the data, which suggested that the best performing simulations in Figure 5-6a are coincidental, overfitting, or lacking additional mechanistic pathways.

However, if the CCSD(T) calculations are to be believed that no activation barrier should exist, then how could this be? One possible explanation is that the reaction, for some reason, is not first order in either or both reactants. A second possible explanation is that the reaction is "frustrated" by conservation of angular momentum. By this law, the total angular moment of the two separate precursors plus their relative, orbital angular momentum must equal the total angular momentum of the adduct immediately before and after the collision. The difficulty in this reaction lies in aligning the vector sum of the precursor angular momenta and the angular momentum of

their relative motion to one of a *discrete* set of possible product angular momenta vectors, as shown in Figure 5-7a. In the liquid or solid state, this is usually not a problem, because the high density of both phases supports a third body to give or receive angular momenta as necessary. However, in the gas phase, the density is orders of magnitudes less, resulting in far fewer third-body type collision events, even at atmospheric pressure.

To estimate the potential impact of angular momentum constraining the reaction, a series of simulations were performed in which the colliding precursors were assumed to 1) be rigid rotors, 2) have aligned rotational angular momentum vectors, $\vec{J}$, through their respective principal axis of rotation, and 3) collide with an orbital angular momentum aligned with $\vec{J}$ (see Figure 5-7b). These conditions maximize the likelihood of satisfying conservation of angular momentum and reduce the problem's geometrical complexity to simple scalar addition of angular momentum values.

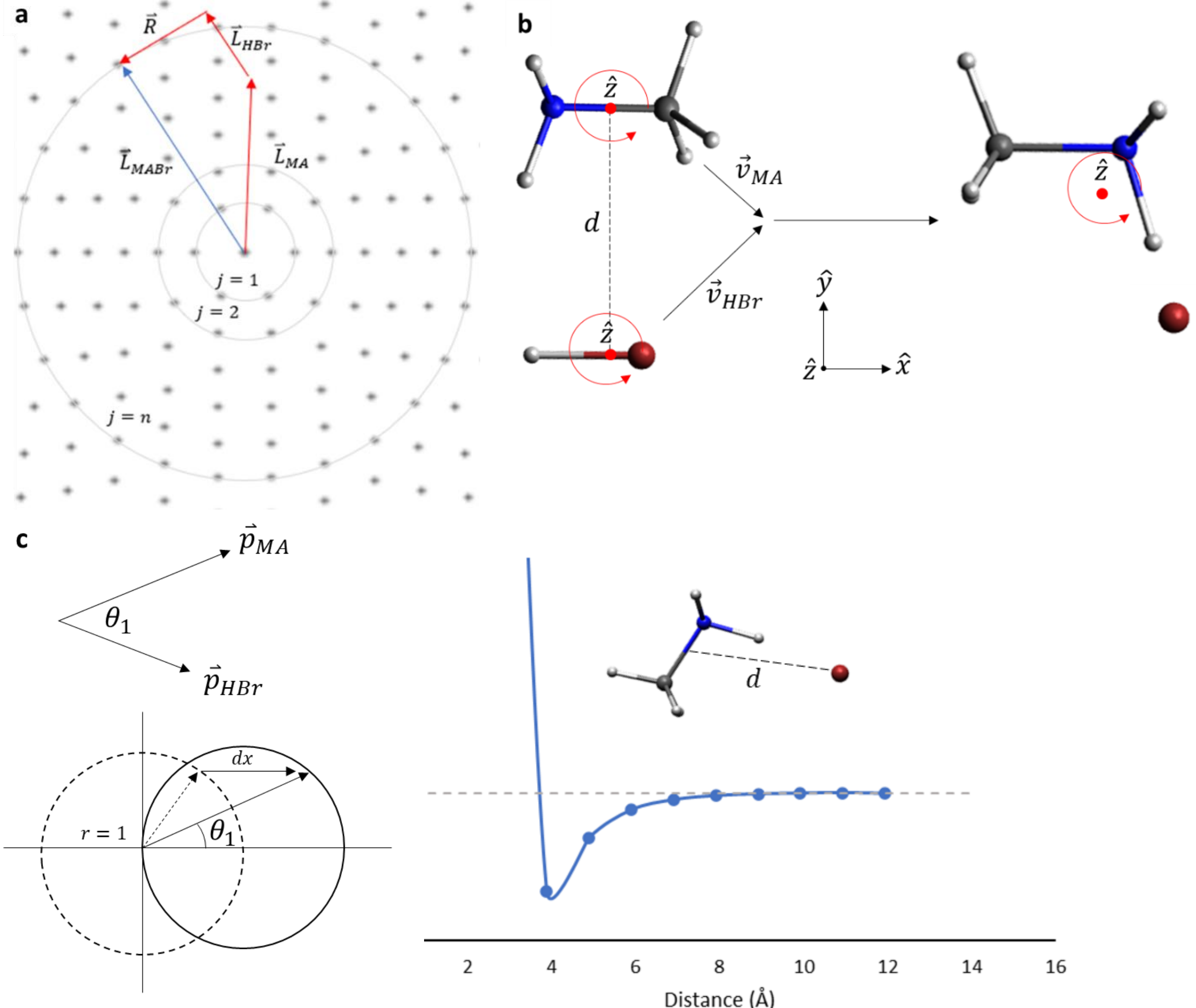

Figure 5-7: (a) Illustration of the difficulty in having all three initial angular momentum vectors add successfully to obtain a rotational eigenstate in the adduct. (b) Illustration of a simulated collision whereby the precursors' and adduct's angular momenta are aligned along the same axis, and the precursors "react" at a fixed distance, d, after colliding in the $\overline{xy}$ plane. (c) Schematic of how the random collision angle was selected along with Equations (5-1), (5-11), and (5-12). (d) Potential energy diagram of the separation of centers of mass of the colliding precursors. The reaction was therefore assumed to occur at 4, 5, and 6 Å for 3 separate simulation series.

The simulations selected random j states for each precursor as well as random initial velocities according to their respective probability density functions (PDFs) (Equations (5-8) and (5-9)). The moment of inertia was calculated for the $\hat{z}$—axis as shown in Figure 5-7b.

$$\mathrm{PDF(j)} = \frac{(2j+1)e^{-\frac{j(j+1)h^2}{8\pi^2 IkT}}}{\sum_{j=0}^{\infty}(2j+1)e^{-\frac{j(j+1)h^2}{8\pi^2 IkT}}} \tag{5-8}$$

$$\mathrm{PDF(v)} = \left(\frac{m}{2\pi kT}\right)^{\frac{3}{2}} 4\pi v^2 e^{-\frac{mv^2}{2kT}} \tag{5-9}$$

The collision angle was first determined by selecting a random point on the unit circle. The x-coordinate was then scaled by dx according to Equation (5-10) and Figure 5-7c to account for the higher probability of "head-on" collisions at similar speeds and more random collision angles at more unequal speeds. Using this angle, the relative speed, Δv (Equation (5-11)), was calculated, and together with the reduced mass of the colliding precursors and a random distance of impact between $[-d,d]$ with d randomly between 4 and 6 Å, as determined in Figure 5-7d, the orbital angular momentum value, $|R|$ (Equation (5-12)), was determined.

$$dx = 1 - \frac{|v_{MA} - v_{HBr}|}{2\bar{v}} \tag{5-10}$$

$$\Delta v = \sqrt{v_{HBr}^2 + v_{MA}^2 - 2v_{MA}v_{HBr}\cos\theta} \tag{5-11}$$

$$|R| = d_{min} \times \mu_{rm} \times \Delta v \tag{5-12}$$

If the sum of these angular momenta equaled an angular momentum eigenvalue within the uncertainty $\hbar/2$ for *any* rotational state of the adduct *and* the resultant rotational energy of the

product was less than 45 kJ/mol (the enthalpy of formation of MABr determined by CCSD(T)), the reaction was assumed to proceed. Otherwise, it was assumed to fail. The results of 100,000 such simulations for a series of temperatures between 10 and 120 °C and maximum distances of reaction randomly selected between 4 and 6 Å indicated a strongly temperature dependent reactivity between 60 and 100 °C due solely to conserving angular momentum (Figure 5-8). However, these simulations are likely generous in estimating the reaction rate dependence on angular momentum conservation as the setup assumed perfectly aligned rotational and orbital angular momentum vectors, which is not true in real experiments. Additional factors such as steric hindrance may also greatly affect the kinetics.

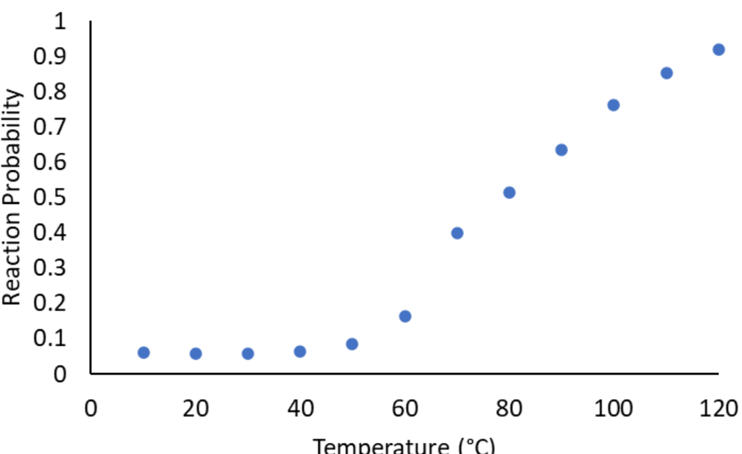

Figure 5-8: Simulations of the reactivity of MA and HBr when considering only the conservation of angular momentum. Here, a reaction is considered to occur if the sum of the reactant rotational and orbital angular momenta are equal to angular momentum eigenvalue of the product and that the resultant rotational energy is less than the enthalpy of formation of MABr (~45 kJ/mol).

While these simulations do not prove the reason for the absence of strong gas phase reactions of MA and HBr, they do suggest that if even in the most favorable conditions for conservation of angular momentum where all rotational vectors were aligned, the reaction still

failed a significant percentage of times, then one could expect even lower reaction probabilities when all possible angles and orientations are considered. A simple experiment to test this hypothesis and the one assuming the reaction orders are not first order would be to run the reactions at lower pressure with varying ratios of [HBr]:[MA]:[N_2]. If only a third body is needed, additional N_2 would facilitate the reaction, but if a different reaction order than first order were true, different ratios of the precursor concentrations would illuminate this deviation in reaction order.

5.4.2 Evidence for Surface Chemistry

Surface reactions of the L-H and R-E type were hypothesized to account for deposited films under the assumption of an absence of gas phase reactions. The strong (001) XRD peaks (Figure 4-1) are consistent with crystalline growth from the substrate, rather than growth from gas phase reactions, which would be consistent with a more polycrystalline film. However, crystallinity alone cannot confirm surface reactions predominate. Additional support for a surface reaction mechanism included the observation of an apparent incubation time in the film growth depending on the growth rate. Shown in Figure 5-9, depositions with a lower overall thickness, as determined by Br EDS intensity, showed a higher ratio for asymmetric peak intensity difference to the peak intensity average.

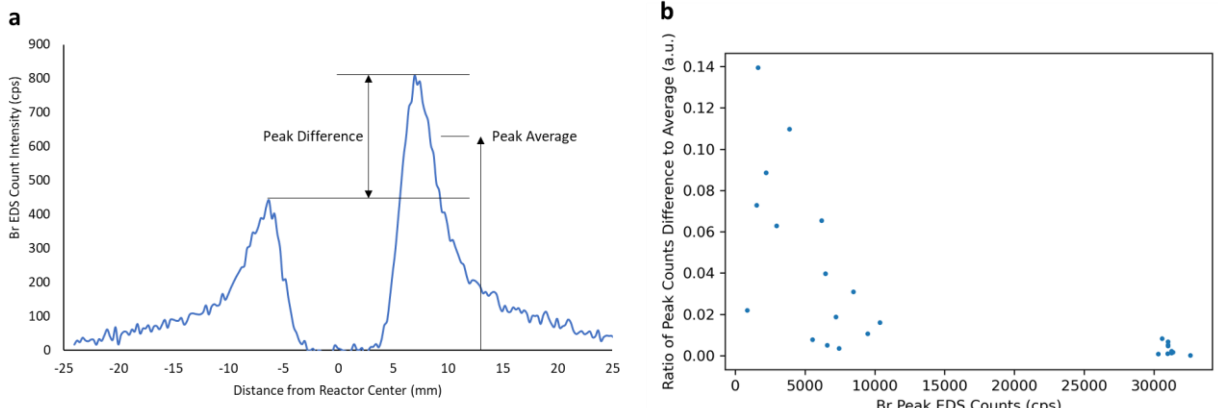

Figure 5-9: (a) An example EDS plot showing asymmetric growth around the reactor center. (b) Plot of the peak difference to peak average ratio vs. peak counts per second (cps). The trend towards a lower ratio as the peak cps increases strongly suggested that growth rate was initially stymied until a critical film thickness was achieved after which growth was consistent.

One interpretation of this result is that surface reactions dominate the growth rate, but that initiation of a consistent growth rate depends on the quality of the surface preparation and, possibly, achieving a nucleation layer. The films were deposited on Si wafers, for which HBr and MA are expected to have a much lower binding affinity than to MABr. This view was also supported by SEM images showing scattered islands of MABr material over areas with less deposition and for films with shorter deposition times or precursor flow rates (see Figure 5-10).

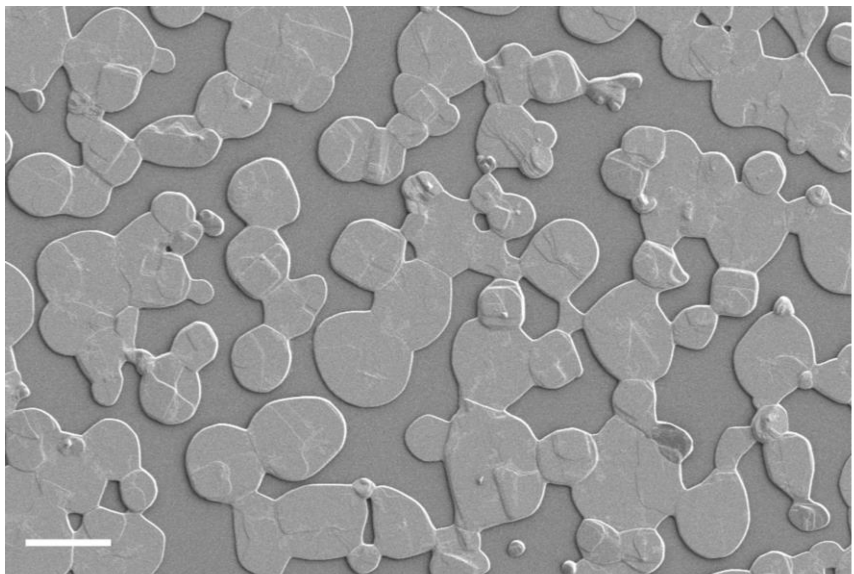

Figure 5-10: SEM image of an example MABr film on Si further away from the reactor center where the precursor concentrations were less. MABr platelets appeared to grow and converge with each other, suggesting growth initiated from discrete islands or seed crystals. The scale bar is 10 μm

To further understand the surface chemistry, two tests were performed to elucidate the growth rate dependencies. The first was a test of the growth rate for different total deposition times. Figure 5-11 shows that the growth rate was relatively insensitive to the total deposition time. Combined with the previous data on asymmetric growth rates vs total deposition, this data supports the conclusion that the growth rate is constant after an initial, unpredictable incubation time dependent on the surface preparation.

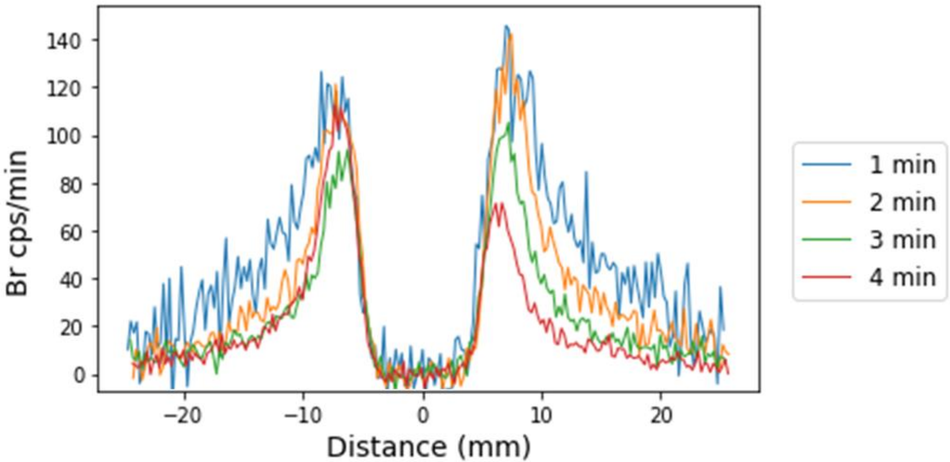

Figure 5-11: Br EDS intensity normalized by deposition time shows the deposition rate is relatively insensitive to the total deposition time. The plot at 4 mins shows strong asymmetry in peak intensity, but this could be attributed to a difference in surface preparation resulting in different times to achieve seed criticality (*vide supra*).

The second test evaluated the claim of a seed layer initiating growth. This experiment involved first depositing a thin layer of MABr at 100 °C where the growth rate was high enough that any asymmetry in growth was suppressed. This was used as a "seed" layer. The substrate was then cooled to 50 °C and a second layer was deposited. The hypothesis was that this deposition would be more symmetric and have a broader spatial EDS profile than the standard deposition without a seed layer due to the seed MABr layer providing a higher activation energy for desorption of MA and HBr, which are critical for a surface reaction. Figure 5-12 shows that the asymmetry was, indeed, greatly reduced but that the extent of the growth rate remained the same. This result suggested that the seed layer helped initiate growth but that growth was dominated by other mechanisms.

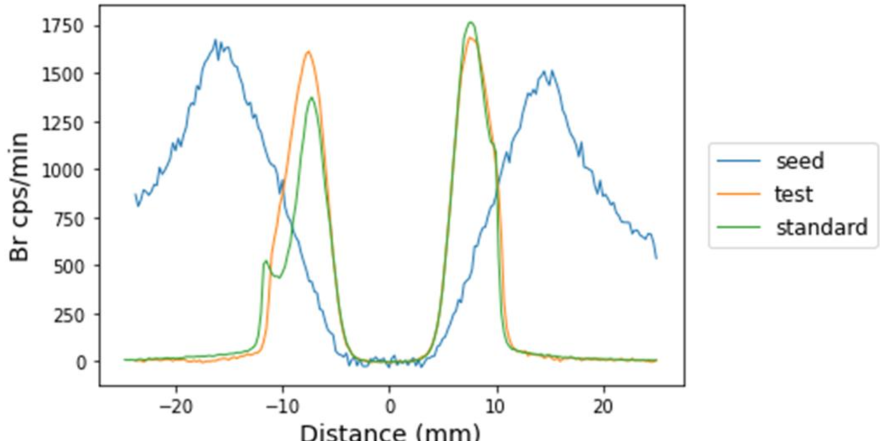

Figure 5-12: Br EDS intensity plot showing the effect of a seed layer on the deposition rate. The seed layer was grown at 100 °C for 30 sec, a sufficiently short time to deposit enough material to form a seed layer but not too long to saturate the EDS signal. The test sample was then deposited on the seed layer after cooling to 50 °C. The standard was a deposition under the same conditions but without the seed layer. The EDS profile for the test sample had the seed layer EDS profile subtracted to fairly compare with the standard.

5.4.3 Evidence for a Rideal-Eley Reaction

The conclusion that a R-E type reaction occurred was deduced as follows. Given the deposition peaks near the reactor center in Figure 5-11 and Figure 5-12 exhibited a constant growth rate after an initial incubation time and considering that film roughness increased with growth (see Figure 4-10), one concludes that the growth rate was also insensitive to surface area. Because the growth rate was approximated by EDS intensity signals, which reflect the amount of *mass* deposited by Castaing's first approximation,[23] a surface area independent growth rate would suggest the growth rate was limited by diffusion of the precursors towards the surface. However, the EDS plots of Figure 5-4 and those for temperatures of 40, 60, and 80 °C of Figure 5-4b reproduced below, strongly support that the reaction is kinetically limited at temperatures below 100 °C and not diffusion limited (within the conditions tested).

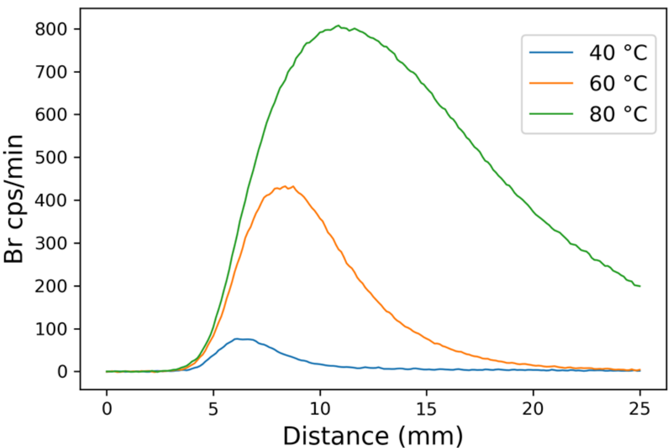

Figure 5-13: Br EDS intensity plots MABr films deposited with flow rates of 0.12 sccm HBr and 0.89 sccm MA at the stated temperatures.

If the growth rate depended on the surface reactivity and not the precursor flux, how could this be consistent with surface area independent growth? More available reactive sites in a kinetic controlled reaction with sufficient supply of precursors would strongly suggest more mass deposition – exactly what doesn't occur!

One plausible explanation for this is that the surface is near fully saturated with adsorbed precursor and, therefore, the important parameter is surface coverage as a percentage of sites, not the total number of surface sites. In this scenario, additional flux to the surface does not result in additional adsorption and the growth rate is limited by the reactivity at the surface. The coverage percentage for MA and HBr would then depend on the gas phase concentration immediately above the substrate and the binding affinity. Given that the concentration of MA was nearly 8× that of HBr near the deposition peak for the conditions in Figure 5-13 as shown in Figure 5-14 (reactions suppressed), one would assume MA had a higher rate of striking the surface.

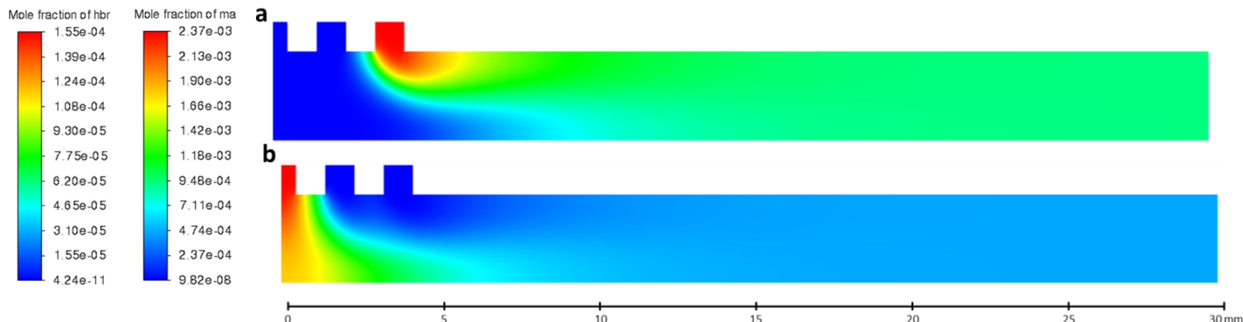

Figure 5-14: Flow fields for (a) HBr and (b) MA showing a much higher concentration of MA near the surface close to the reactor center (far left) with flow rates of 0.12 sccm HBr and 0.89 sccm MA.

Considering MA's higher surface impingement rate and that DFT predicted MA to have a higher binding energy than HBr, it was assumed that the surface was covered primarily with adsorbed MA. Using this assumption and the assumption of non-linear desorption and reactivity with MA surface concentration, it was possible to explain the depositions at 40 and 120 °C purely by a R-E type reaction, as shown in Figure 5-15, for the reaction conditions of Figure 5-4b and Figure 5-13. The assumption of growth being non-linearly dependent on the concentration of adsorbed MA and not on the presence of a seed layer is also consistent with the results of Figure 5-12.

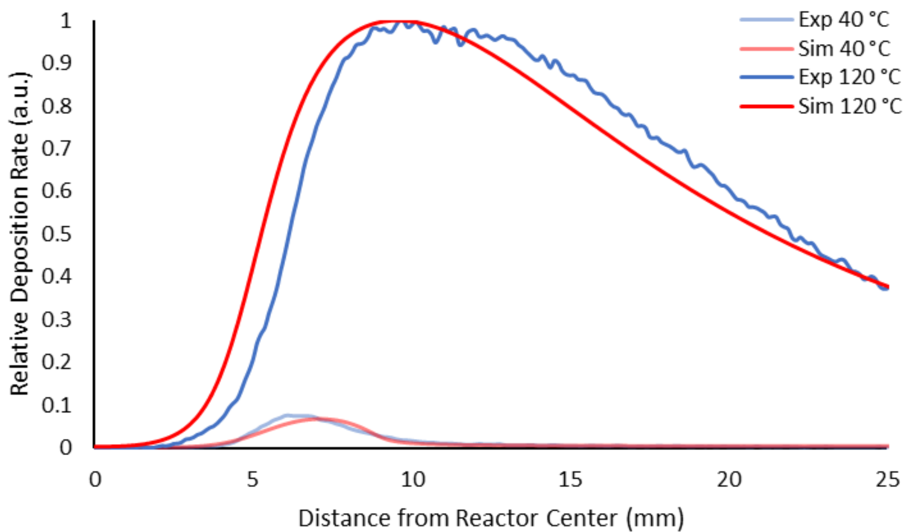

Figure 5-15: Example comparison of scaled experimental Br EDS profile measurements and scaled simulations assuming only a R-E type reaction with adsorbed MA concentration dependent reaction and desorption rates.

However, beyond identifying the peak closest to the reactor center as a R-E type reaction, there was insufficient data and mechanistic understanding to fit all the data in the temperature series with a consistent set of parameters. A full set of parameters could be obtained in future work by carefully controlling the surface state and using a fully coated substrate prior to deposition to eliminate the spatial dependence on adsorption and desorption rates.

5.4.4 Evidence for a L-H Reaction

Different than R-E type reactions, L-H type reactions occur by the surface reaction of two adsorbed precursors. The appearance of this type of reaction was, therefore, expected for depositions when the flow rates of each precursor were nearly equal. In this scenario, the coverage of surface sites would be more evenly distributed and the reaction rate (Equation (5-5)) would be maximized. However, because of the positions of the gas injector inlets (see Figure 5-14), the

substrate surface near the reactor center was mostly covered by adsorbed MA. Therefore, it was expected that a L-H type reaction would occur further away from the reactor center. Indeed, Figure 5-16 supports such a claim, showing a satellite peak away from the reactor center.

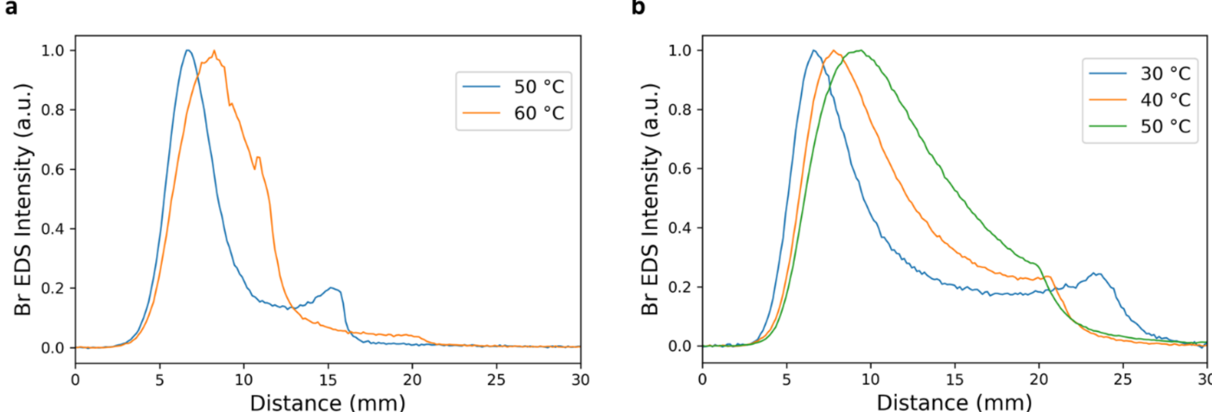

Figure 5-16: Br EDS intensity profiles for depositions with 0.06% HBr and 0.067% MA for two different sets of depositions days apart show a peak further away from the main peak, consistent with a L-H type reaction. Note the difference in shape between the two profiles at 50 °C. This difference was likely due to the MA precursor supply running out during the depositions of samples in (a). The EDS intensities were normalized by the peak intensity of the sample to magnify the small satellite peak.

Again, because the apparent non-linear dependence of surface reactivity and desorption on the coverage percentage of MA (and possibly HBr), it was not practical to fit the model without considerably more data and insights into the mechanisms of this non-linearity. However, it was possible to show that a purely L-H type reaction *could* explain the small satellite peak and is consistent with the trend of decreasing distance from the reactor center with an increase in temperature (Figure 5-17).

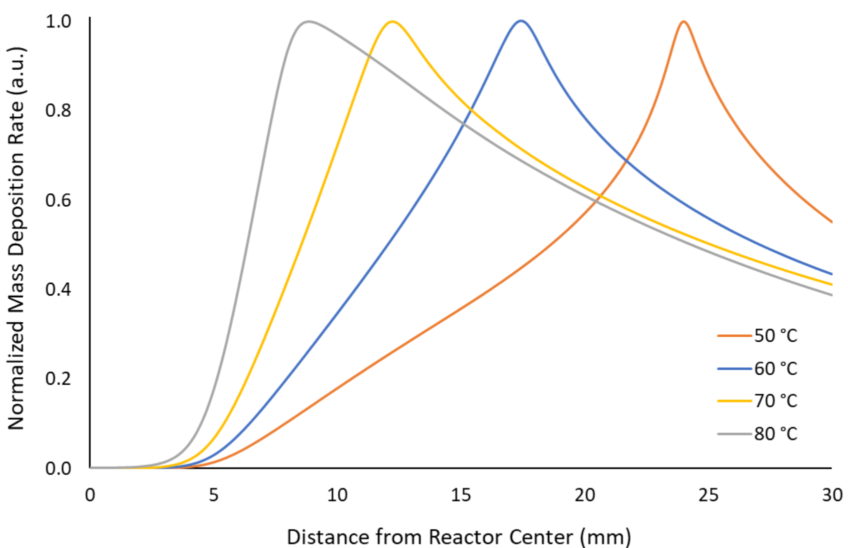

Figure 5-17: Simulations of a purely L-H type reaction at the stated temperatures. As with modeling a R-E type reaction, more data and mechanistic insights were needed to completely fit the model with the least number of parameters.

5.5 Conclusion

This chapter explored the mechanisms resulting in the film formation by attempting to model EDS intensity data using a CFD / CVD model. The initial fluid parameters for the model were constructed from classical kinetic theory of gases assuming an Arrhenius rate for the reactions. DFT / CCSD(T) calculations were used to estimate the activation energies for gas phase reaction and desorption. Unexpectedly, no gas phase reaction model was able to predict the EDS signal profile, which suggested gas phase reactions did directly contribute to the film deposition, if at all. It was hypothesized that this was due to frustration by the conservation of angular momentum, although more theoretical and gas phase spectroscopic measurements are needed to confirm. In lieu of a gas phase reaction, evidence for Rideal-Eley (R-E) and Langmuir-Hinshelwood (L-H) type reactions were provided. However, the models were not able to fully describe the EDS profiles with a single, consistent set of parameters. One of the primary difficulties in this process was the

non-linear behavior of the depositions at lower temperatures. Future work should aim to collect more data with a consistent surface by pre-depositing a uniform coating and employ data analysis schemes (e.g. machine learning) to aid in model fitting.

5.6 Appendix

1. Park, J.-W., Kim, B.-K., Kim, H. J. & Park, S. Experimentation and simulation of tin oxide deposition on glass based on the SnCl4 hydrolysis in an in-line atmospheric pressure chemical vapor deposition reactor. *Thin Solid Films* **550**, 114–120 (2014).

2. Ghoshtagore, R N. Mechanism of CVD Thin Film SnO Formation. *J. Electrochem. Soc.* **125**. 110-117 (1978)

3. Hierlemann, M., Kersch, A., Werner, C. & Schfer, H. A Gas-Phase and Surface Kinetics Model for Silicon Epitaxial Growth with SiH2CI2 in an RTCVD Reactor. *J. Electrochem. Soc.* **142.** 259-266 (1995)

4. ANSYS, Inc. *Fluent 2020 R1 User's Guide* (2020)

5. Xuan, Y. Multi-Scale Modeling of Gas-Phase Reactions in Metal-Organic Chemical Vapor Deposition Growth of WSe2. *Journal of Crystal Growth* **527**. 1-11 (2019)

6. Bird, R. B., Stewart, W. E., and Lightfoot, E. N. *Transport Phenomena. Rev. 2. ed.* (Wiley, New York 2007).

7. Lombardo, S. J. & Bell, A. T. A review of theoretical models of adsorption, diffusion, desorption, and reaction of gases on metal surfaces. *Surface Science Reports* **13**, 3–72 (1991).

8. Martin, R. Density functional theory. in *Electronic Structure: Basic Theory and Practical Methods*. (Cambridge University Press, U.K. 2004).

9. Crawford, T.D. and Schaefer, H.F. III. An Introduction to Coupled Cluster Theory for Computational Chemists. in *Reviews in Computational Chemistry* (eds K.B. Lipkowitz and D.B. Boyd) (2000)

10. Neese, Frank. The ORCA program system. *Wiley Interdisciplinary Reviews: Computational Molecular Science* **2**. 73–78 (2012)

11. Ásgeirsson V, *et al.* Nudged Elastic Band Method for Molecular Reactions Using Energy-Weighted Springs Combined with Eigenvector Following. *J Chem Theory Comput.* **17**. 4929-4945 (2021).

12. JÓNSSON, H., MILLS, G., & JACOBSEN, K. W. Nudged elastic band method for finding minimum energy paths of transitions. in *Classical and Quantum Dynamics in Condensed Phase Simulations*. (eds. Berne, B. and Ciccotti, G.) (World Scientific, 1998).

13. Mardirossian, N. & Head-Gordon, M. ωB97X-V: A 10-parameter, range-separated hybrid, generalized gradient approximation density functional with nonlocal correlation, designed by a survival-of-the-fittest strategy. *Phys. Chem. Chem. Phys.* **16**, 9904 (2014).

14. Liakos, D. G., Guo, Y. & Neese, F. Comprehensive Benchmark Results for the Domain Based Local Pair Natural Orbital Coupled Cluster Method (DLPNO-CCSD(T)) for Closed- and Open-Shell Systems. *J. Phys. Chem. A* **124**, 90–100 (2020).

15. Oura, K., Katayama, M., Zotov, A. V., Lifshits, V. G. & Saranin, A. A. Elementary Processes at Surfaces I. Adsorption and Desorption. in *Surface Science* 295–323 (Springer Berlin Heidelberg, 2003).

16. Corsini, C., Peeters, S. & Righi, M. C. Adsorption and Dissociation of Ni(acac) $_2$ on Iron by Ab Initio Calculations. *J. Phys. Chem. A* **124**, 8005–8010 (2020).

17. Boys, S. F.; Bernardi, F. The calculation of small molecular interactions by the differences of separate total energies. Some procedures with reduced errors. *Mol. Phys.* **19**. 553-566 (1970)

18. Gabe, E. J. The crystal structure of methyl ammonium bromide. *Acta Crysl*. **14**, 1296 (1961)

19. Poling, B. E., Prausnitz, J. M. & O'Connell, J. P. *The properties of gases and liquids*. (McGraw-Hill, 2001)

20. Tang, M. J., Cox, R. A. & Kalberer, M. Compilation and evaluation of gas phase diffusion coefficients of reactive trace gases in the atmosphere: volume 1. Inorganic compounds. *Atmos. Chem. Phys*. **14**, 9233–9247 (2014)

21. Svehla, R. A. Estimated Viscosities and Thermal Conductivities of Gases at High Temperatures. NASA Lewis Research Center (1962).

22. Wilke, C. R. & Lee, C. Y. Estimation of Diffusion Coefficients for Gases and Vapors. *Ind. Eng. Chem*. **47**, 1253–1257 (1955).

23. Castaing, R. Application des Sondes Electroniques a une Methode d'Analyse Ponctuelle Chimique et Crystallographique. (University of Paris, Paris, 1951)

6 Conclusion

This thesis was motivated to help address climate change by exploring the possibility of depositing perovskite thin films by APCVD for applications in solar panel manufacturing. Chapter 1 further describes this motivation and rationale for this approach. Chapter 2 discusses the approach to precursor selection and some synthetic strategies for use in lab-scale depositions. Chapter 3 explores CFD modeling to design a reactor capable of depositing the films without clogging the inlet. Chapter 4 shares the results of deposition characterization to confirm the presence of the desired compound and that the deposited material is suitable for EDS analysis and modeling. Chapter 5 presents the preliminary results of modeling attempts to describe the deposition process. The modeling demonstrated an absence of gas phase reactivity but potentially significant Rideal-Eley and minor Langmuir-Hinshelwood type reactions at low temperature (< 100 °C) under the flow conditions tested. Film growth rates above this temperature appeared to transition to a mass diffusion limited regime.

Although these results provided limited answers to quantitative mechanistic understanding of the APCVD process, they do provide a strategy for future modeling of APCVD depositions and suggest areas for improvement. Future efforts should be directed towards novel, data analysis strategies to efficiently identify mechanistic parameters. Beyond perovskites, this work is translatable to all types of atmospheric pressure, gas-phase deposition processes.